Doktorarbeit

Bacterial motility and growth in open and confined environments

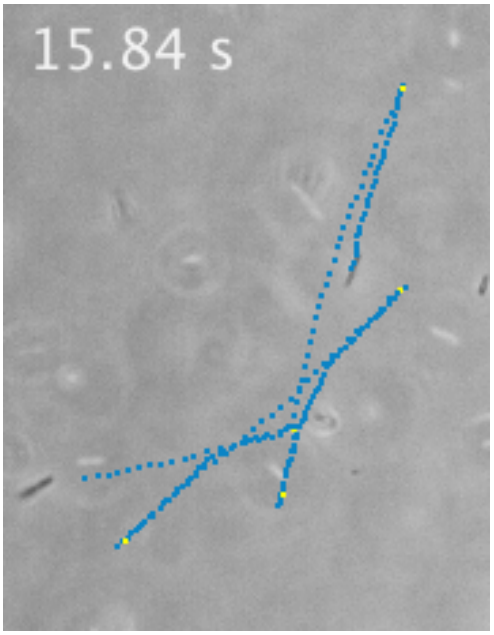

UNIVERSITÄT POTSDAM

MATTHIAS THEVES

March 28, 2014

Published online at the
Institutional Repository of the University of Potsdam:
URL http://opus.kobv.de/ubp/volltexte/2014/7031/
URN urn:nbn:de:kobv:517-opus-70313
http://nbn-resolving.de/urn:nbn:de:kobv:517-opus-70313

Contents

Chapter 1

Abstract

In the presence of a solid-liquid or liquid-air interface, bacteria can choose between a planktonic and a sessile lifestyle. Depending on environmental conditions, cells swimming in close proximity to the interface can irreversibly attach to the surface and grow into three-dimensional aggregates where the majority of cells is sessile and embedded in an extracellular polymer matrix (biofilm). We used microfluidic tools and time lapse microscopy to perform experiments with the polarly flagellated soil bacterium *Pseudomonas putida* (*P. putida*), a bacterial species that is able to form biofilms. We analyzed individual trajectories of swimming cells, both in the bulk fluid and in close proximity to a glass-liquid interface. Additionally, surface related growth during the early phase of biofilm formation was investigated. In the bulk fluid, *P. putida* shows a typical bacterial swimming pattern of alternating periods of persistent displacement along a line (runs) and fast reorientation events (turns) and cells swim with an average speed around 24 μm/s. We found that the distribution of turning angles is bimodal with a dominating peak around 180 degrees. In approximately six out of ten turning events, the cell reverses its swimming direction. In addition, our analysis revealed that upon a reversal, the cell systematically changes its swimming speed by a factor of two on average. Based on the experimentally observed values of mean runtime and rotational diffusion, we presented a model to describe the spreading of a population of cells by a run-reverse random walker with alternating speeds. We successfully recover the mean square displacement and, by an extended version of the model, also the negative dip in the directional autocorrelation function as observed in the experiments. The analytical solution of the model demonstrates that alternating speeds enhance a cells ability to explore its environment as compared to a bacterium moving at a constant intermediate speed. As compared to the bulk fluid, for cells swimming near a solid boundary we observed an increase in swimming speed at distances below $d \approx 5$ μm and an in-

crease in average angular velocity at distances below $d \approx 4$ μm. While the average speed was maximal with an increase around 15% at a distance of $d = 3 \pm 1$ μm, the angular velocity was highest in closest proximity to the boundary at $d = 1 \pm 1$ μm with an increase around 90% as compared to the bulk fluid. To investigate the swimming behavior in a confinement between two solid boundaries, we developed an experimental setup to acquire three-dimensional trajectories using a piezo driven objective mount coupled to a high speed camera. Results on speed and angular velocity were generally consistent with motility statistics in the presence of a single boundary. Additionally, an analysis of the probability density revealed that a majority of cells accumulated near the upper and lower boundaries of the microchannel. The increase in angular velocity is consistent with previous studies, where bacteria near a solid boundary were shown to swim on circular trajectories, an effect which can be attributed to a wall induced torque. The increase in speed at a distance of several times the size of the cell body, however, cannot be explained by existing theories which either consider the local drag increase on cell body and flagellum near a boundary (resistive force theory) or model the swimming microorganism by a multipole expansion to account for the flow field interaction between cell and boundary. An accumulation of swimming bacteria near solid boundaries has been observed in similar experiments. Our results confirm that collisions with the surface play an important role and hydrodynamic interactions alone cannot explain the steady-state accumulation of cells near the channel walls. Furthermore, we monitored the number growth of cells in the microchannel under medium rich conditions. We observed that, after a lag time, initially isolated cells at the surface started to grow by division into colonies of increasing size, while coexisting with a comparable smaller number of swimming cells. After $5 : 50$ hours, we observed a sudden jump in the number of swimming cells, which was accompanied by a breakup of bigger clusters on the surface. After approximately 30 minutes where planktonic cells dominated in the microchannel, individual swimming cells reattached to the surface. We interpret this process as an emigration and recolonization event. A number of complementary experiments were performed to investigate the influence of collective effects or a depletion of the growth medium on the reported transition. Similar to earlier observations on another bacterium from the same family we found that the sudden release of cells to the swimming phase is most likely the result of an individual adaption process, where syntheses of proteins for flagellar motility are upregulated after a certain number of division cycles at the surface.

Chapter 2

Introduction

Bacteria are micron-sized organisms which swim by using the periodic movement of one or several cellular appendages called flagella, slender semi-flexible filaments with an average diameter around 50 nanometers. While eukaryotic cells like spermatozoa swim with an actively beating filament driven by molecular motors [115], bacteria rotate one or several passive, helically shaped filaments, which are connected to a rotary motor in the cell wall, to propel themselves forward using the asymmetric drag force exerted by the surrounding fluid on the individual segments of the helix [86, 121]. The classical picture of bacterial swimming motility has been founded by the seminal work of Howard Berg on the intestinal bacterium *Escherichia coli* which is equipped with left-handed helical flagella [8, 146]. If the left-handed helical flagella rotate counterclockwise, hydrodynamic interactions lead the filaments to form a stable, coherent bundle. The cell swims along a straight line and is said to perform a 'run'. If one or several motors start to rotate clockwise, the bundle becomes unstable, the filaments fly apart and orient themselves towards random directions pointing away from the cell. The thrusts generated by the opposing filaments cancel each other. The cell irregularly jiggles around its center of mass without net displacement and is said to perform a 'tumble'.

Under uniform environmental conditions, the trajectory of a swimming bacterium displays alternating periods of run and tumble [8]. In a nonuniform environment, the presence of an external stimulus, e.g. a gradient in the concentration of oxygen, nutrients, in the pH-value or in the intensity of light, can lead a cell to bias its random trajectory towards one direction [45]. In case of directed migration towards or away from gradients of chemical substances, generally termed chemoattractants or chemorepellents, this process is called chemotaxis [45, 155]. Typically, this is regulated by an intracellular signaling network which monitors the ambient concentration experienced by the swimming cell (temporal sensing). If the ambient concentration of the chemoattractant

increases over time, downstream molecular reactions at the sites of the motors stabilize the state of motor units rotating in a direction which is favorable for stable bundle formation and forward propulsion. The average duration of runs pointing towards the chemical source is prolonged while the runs pointing towards negative gradients are shortened. A population of cells performs directed migration.

In the past, major work has been devoted to study and model the behavior of free-swimming cells in the bulk fluid both undergoing random and directional migration. Extensive experiments have investigated the details of power generation within the flagellar motor unit [7, 16], the shape transitions of flagella during run and tumble motion [34], and their assembling process [1], as well as the effects of viscosity and Non-Newtonian fluids [9, 132], cell geometry, and flagellation on the swimming pattern of a bacterium [161]. Theoretical models have been proposed for the chemotactic sensing pathway [134, 145] and for two and three dimensional random walks describing the spreading of a cell population [28, 98].

More recently both physicists and biologists have turned towards understanding the swimming and colonization behavior of bacteria in the presence of a surface. At a solid-liquid or liquid-air interface the majority of bacterial species are capable of forming multicellular aggregates called biofilms by secretion of adhesive substances [116, 138]. Although there remain challenging academic questions about free-swimming microorganisms, the majority of bacteria in their natural environment are actually living and replicating in confined environments, where rigid boundaries which affect their motile behavior and allow for transitions to the sessile biofilm lifestyle are ubiquitous [41]. As in almost all bacterial species the majority of cells are living in sessile aggregates with a downregulated flagella driven motility mechanism one could go as far as to consider bulk fluid swimming as a simple transition state, where a bacterium is traveling from one biofilm to the next surface related aggregate. The process of biofilm formation can be subdivided into four major phases, (1) near surface swimming, (2) reversible and irreversible attachment to the surface, (3) surface related growth and cell differentiation and (4) a detachment or recolonization phase. All motile and non-motile activities of bacteria in the presence of a surface can be categorized according to their function in one of these four subsequent steps of biofilm formation:

(1) During the early phase, free-swimming cells from the bulk fluid randomly approach the surface. Depending on the details of the swimming mechanism and the geometry of the cell, hydrodynamic wall effects can accelerate or decelerate the cell trajectory, lead to a parallel or perpendicular alignment of cell body or swimming direction and create an attractive or repulsive force [86]. Eventually, these effects can induce a torque act-

ing on flagella and body that 'entraps' the cell at a constant distance to the boundary and leads to a circular swimming path [84]. Most commonly, because we are in the low Reynolds number regime, so called resistive force theory has been used to model the swimming behavior near the surface, which assumes a locally linear relationship between translational and angular velocities of body and flagellum on the one hand and induced drag forces and moments on the other hand [21, 34, 121]. Experiments using multi particle tracking of fluorescent nanobeads have confirmed that the flow field created by a swimming bacterium can be modeled by a force dipole [42] and the presence of a surface can then be accounted for by introducing mirror images analogously to electrostatics to satisfy the no-slip boundary condition [137].

(2) Near surface swimming bacteria eventually collide with the wall and temporarily attach to it. Several experiments have investigated the influence of shear flow and how surfaces of different roughness and with different coatings affect the attachment and detachment rate [74, 89, 118]. This has been in the focus of applied research in the food science and engineering field to prevent undesired corrosion and fouling effects [136]. Experiments with mutant cell lines of *Pseudomonas aeruginosa* have also pointed to the role of type IV-pili, hair like cellular appendages, usually thinner than propulsive flagella, during the attachment and detachment process [81]. Synchronized projection, anchoring and retraction of IV pili is also responsible for so called 'twitching motility', one among several possible modes for cell movement across a surface [29, 71]. While coordinated surface motility can promote the formation of cellular aggregates as observed in *Neisseria gonorrhoeae* [15, 69], in some bacterial strains random twitching motility prevents bacteria from forming colonies of sizes sufficient to induce biofilm formation [80].

(3) The initially isolated cells, which have irreversibly attached to the surface, start to grow by division and form the cores of expanding colonies. At the beginning the colonies on the surface coexist and exchange with cells in the swimming phase from the boundary layer, developmental stages (2) and (3) overlap. Depending on a variety of conditions, after the cells have spend a certain amount of time on the surface, usually starting with bacteria embedded within the bigger colonies, the secretion of adhesive substances and the developmental program towards the mature biofilm is initiated [116, 138]. It is the subject of ongoing research how surface contact from the cell wall signals to the genetic network of the individual cell to downregulate flagellar activity, upregulate production of proteins for the biofilm matrix, and induce metabolic changes [36, 51, 131, 163]. Experiments and theoretical studies have also tried to elucidate the contribution of density dependent effects (quorum sensing), where a transition towards the biofilm state is triggered when the local concentration of a signaling sub-

stance, secreted by the cell, exceeds a certain threshold [37, 60, 109]. In general for many bacterial species it is still unclear, whether one is at all looking at a coordinated, cooperative developmental program like during the formation of fruiting bodies observed in some species or whether biofilm patterns emerge from purely local adaption of individual cells that do not interact with each other [80, 108].

(4) Specific environmental conditions e.g. a depletion of growth medium can trigger the dissolution of biofilm colonies. Cells from inside the aggregates change back to their planktonic phenotype, become motile again and break through the wall, which is formed by a subpopulation of biofilm cells [80, 138]. Loose protruding structures remain at the surface and a majority of cells is released to the bulk fluid phase.

In the present work, experiments are performed with the model organism *Pseudomonas putida* (*P. putida*), a soil bacterium which has been studied extensively in the context of biodegredation and biofilm research. We use microfluidic tools and high-speed microscopy to study (i) the swimming of aggregation competent cells at varying distance from a surface and in microchannels of varying height, (ii) the early phase of surface associated growth in colonies at the surface. We thus focus on the early stage of biofilm formation (step (1) till beginning of step (3)), till the point where we can still identify individual cells and where colony growth is restricted to two dimensions.

After an introduction from a biological perspective on bacteria in a sessile or a motile lifestyle (section 3.1), we present the basic properties of our model bacterium *P. putida*, most importantly its flagellation and its environmental function (section 3.2). The physical fluid dynamics of bacteria swimming in an environment where viscous forces exerted by the fluid dominate over inertial force is explained in section 3.3. First, we present the governing hydrodynamic equation, the Stokes equation, and general implications of its characteristic features on bacterial swimming (section 3.3.1). Second, we explain how asymmetric drag experienced by the individual segments of a rotating flagellum generates the necessary thrust force for bacterial propulsion (section 3.3.2). Additionally, the propulsion matrix formalism, a general framework to describe the relationship between forces and velocities in a free-swimming bacterium is presented. Third, we give an overview on how the trajectories of bacteria swimming in a confined environment are affected by hydrodynamic stresses near solid boundaries (section 3.3.3). The background chapter closes with a random walk model which is used to describe the motion of a bacterium swimming with a basic 'run-tumble' pattern (section 3.4). In the results chaper, this model will serve as a starting point to describe a bacterium with a more complex swimming pattern.

In chapter 4 we explain how we recorded and analyzed trajectories of swimming and sessile cells in different microfluidic devices. After presenting our cell culture techniques (section 4.1), we describe the subsequent steps involved in the fabrication of microchannels using soft lithography (section 4.3). The experimental setup for time-lapse microscopy and the image segmentation and tracking algorithm to acquire two-dimensional cell trajectories is presented in section 4.4.1 and section 4.5.1 respectively. To track the motion of swimming cells in three dimensions, we performed time lapse recordings with a synchronized piezo driven objective turret introduced in section 4.4.2 and used a reconstruction algorithm to extract the three-dimensional shape of the cell body (section 4.5.3). An additional procedure to determine the swimming height also from two-dimensional cell trajectories is described in section 4.5.2. At the end of the methods section, we introduce the different motility statistics calculated from the recorded cell trajectories (section 4.6).

The results of this work are presented in chapter 5. We first analyze two-dimensional trajectories of swimming cells in the bulk fluid (section 5.1.1). Based on the experimental results and on the observed swimming pattern, a random walk model with two different levels of complexity is developed to describe the spreading behavior of a population of cells (section 5.1.2). To evaluate how motility statistics of swimming cells are affected in a confined micro-environment we perform experiments with bacteria swimming 'sandwiched' between two solid boundaries (section 5.2.1) and in close proximity to a single open boundary (section 5.2.2). These results are complemented by three-dimensional cell tracking experiments in a two boundary confinement with particular emphasis on the orientation of a cell's swimming direction with respect to the solid boundaries (section 5.2.3). Apart from the motility statistics of swimming cells, we analyze the number growth of an initial population of sessile and motile cells in the microchannel (section 5.3.1). To discriminate between different factors affecting the growth dynamics, we perform additional experiments, one in which the growth medium is periodically renewed (section 5.3.2) and another one where we simultaneously monitor two different subpopulations of cells in a microchannel with a Y-shaped geometry (section 5.3.3). Within the results chapter, we discuss the most important findings at the end of each section.

A full résumé of this work which summarizes the main results and provides an outlook to future experiments is given in chapter 6.

Chapter 3

Background

3.1 Bacteria - Planktonic and sessile life

Bacteria and Archaebacteria constitute the oldest microorganisms on earth. Typically they have a rigid cell wall and grow to a size from one to five micrometers with a spherical or rod-like shape of the cell body. Together they form the class of prokaryotic cells and lack a membrane bound nucleus, which is present in every eukaryotic cell. Eukaryotic cells are typically much larger (10 μm to 100 μm) and maintain complex functions in interior compartments (organelles) to generate energy, replicate DNA, and synthesize proteins [2]. Starting e.g. with a single fertilized eukaryotic cell, through functional differentiation (e.g. as epithelial cells, nerve cells, brain cells etc.), eukaryotic cells can constitute multicellular organs in plants and animals.

Bacteria on the other hand mostly live as unicellular organisms and are ubiquitous in nature, representing a significant fraction of the total biomass on earth [147, 157]. For example, the total biomass of planktonic Cyanobacteria in lakes and on land soil crusts alone was estimated to be on the order of $3 \cdot 10^{11}$ kg [53] and exceeds the amount of biomass represented by humans ($\approx 1.05 \cdot 10^{11}$ kg). Because of their fast mutation and growth rate they are highly adaptive and can be found in extreme environments such as hot water springs or the arctic ice [5, 17], petroleum storage tanks [66], and solutions containing dissolved heavy metals and highly acidic or basic environments [114]. Bacterial communities have been found living in extremely dry conditions in the Atacama Desert [30, 112] (‚the closest one can get to Mars while remaining grounded on earth' [49]) and even under extreme radiation in the reactors of nuclear power plants [62]. Among bacteria, approximately 40% of the species are motile. With varying degree of precision in their mechanistic and molecular description, we can distinguish

between five different types of bacterial movement: swimming as a way of translocation in viscous fluids and gliding, twitching, spreading, and darting as slower, surface related motility modes [33, 67]. Motility allows a bacterium to explore its surrounding in quest for nutrients or otherwise more favorable environments for growth and host infection. In the following part, we will explain the two principal states of bacterial life, first the biofilm state (section 3.1.1), in which the majority of cells is sessile with reduced surface motility and second the planktonic or swimming state (section 3.1.2), where cells move through the surrounding fluid by means of flagellar propulsion. The focus of this work is to analyze the motility of a bacterium, capable of forming biofilms and swimming in very close proximity to a rigid surface during the early stage of colony formation.

3.1.1 Bacteria in sessile biofilm state

In the presence of a solid-liquid or liquid-air interface, planktonic bacteria adhere to the surface because of the hydrophobic nature of their cell wall [150]. Swimming cells from the bulk fluid collide with the surface, temporarily attach to it and join the population on the surface. Depending on environmental conditions, attachments may become irreversible. Initially, isolated cells on the surface grow by binary fission with a doubling time on the order of 30 minutes, varying from species to species and with environmental conditions, and form the cores of expanding colonies. As cell density on the surface and colony size increase, developmental signals trigger the secretion of extracellular polymeric substances (EPS), mostly polysaccharides, lipids, and nucleic acid [48, 59]. Approximately after $24 - 48$ hours of development, the majority of cells is sessile and embedded in this extracellular matrix, which can form a variety of regular and irregular three-dimensional structures with different length scales (see figure 3.2(a)). The mature biofilm has formed in which cells functionally differentiate and constitute a complex interdependent community [31, 138]. While some cells are in an inactive state with reduced metabolic activity, a small number remains in the planktonic state and swims through hollow parts of the biofilm matrix. Parts of the biofilm remain permeable to oxygen and diffusion of nutrients (see figure 3.1 for a schematic represenation of the subsequent steps of biofilm formation).

Due to the high resistivity of cell aggregates within the EPS against harsh conditions and antibiotic treatment, biofilm formation is important for understanding chronic bacterial infections and has been in the focus of medical and food science research [31, 136]. In bioengineering applications it can have desired effects, e.g. the degredation of organic compounds in bioreactors, whereas in mechanical engineering it is responsi-

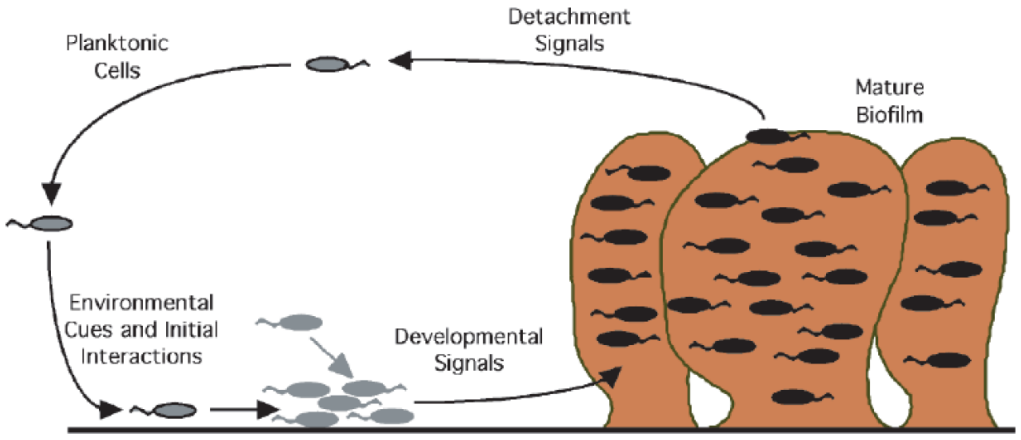

Fig. 3.1: Subsequent stages of biofilm development at solid-liquid interface: planktonic cells from the bulk fluid irreversibly attach to the surface and form growing colonies. If the density on the surface is high enough, a developmental program is triggered and the cell phenotype changes. After approximately 48 hours, the majority of cells are embedded in an extracellular polymeric matrix (EPS). The mature biofilm has formed. Picture taken from [116].

ble for undesired corrosion and fouling of surfaces (figure 3.2(b)). For physicists the interplay between various effects during the subsequent developmental stages of a biofilm (quorum sensing, chemotaxis, hydrodynamic interactions, swarming of active particles), makes biofilm formation a prime example for a complex biological system, where collective behavior plays an important role. Within this context, bacteria are often described as self-propelled particles or active Brownian particles (see [129] for a review). Theoretical studies investigated the collective dynamics in high density populations of active particles with various approaches to model the local interaction of particles, e.g. by collision based alignment depending on geometry or short and long range attraction/repulsion [58, 119, 151]. Predictions were compared with experimental results on the onset of collective motion and colony formation in *Myxococcus xanthus* or *Bacillus subtilis*, bacterial species which display gliding or swarming motility during the early stage of aggregation on the surface [119, 164]. How chemotaxis and quorum sensing contribute to the self-organization of bacteria on a surface has been addressed in a number of experimental and mathematical studies and is subject to ongoing research [25, 79, 105]. Recently, research also starts to address the symbiotic or competitive interactions in biofilms formed by multiple bacterial species [61, 68].

(a) (b)

Fig. 3.2: (a) Macroscopic cyanobacteria-biofilm with a ‚mushroom' like structure grown in a hotwater spring with low-shear environment. The size of the aggregate is on the order of several centimeters. (b) Contamination of ship hulls with biofilm increases hydrodynamic drag. Pictures taken from [59, 143].

3.1.2 Swimming bacteria

Bacteria in the bulk fluid swim by rotating a helical, corkscrew shaped filament. The motion of the filament has to be non reciprocal (invariant under time reversal) because inertial forces are negligible in the hydrodynamic regime of low Reynolds numbers governing the motion of swimming cells [122]. The speed of the swimming cell depends on the propulsion power, i.e. the work provided by the flagellar motor at a given shape of the filament (helical pitch and radius) against the viscous drag of the surrounding fluid and on the hydrodynamic drag experienced by the cell body.

Owing to the nature of their propulsion mechanism, bacteria exhibit distinct motility patterns. In the best studied bacterial model organism, the intestinal bacterium *Escherichia coli* (*E.coli*), several flagella are uniformly distributed across the cell surface (peritrichous flagellation). When all motors are rotating counterclockwise (CCW), the filaments bundle together and the thrust of the rotating left-handed helices push the cell forward. The bacterium swims in a straight line and is said to perform a ‚run' (figure 3.3(left)). When one or several motors start to rotate clockwise (CW) the bundle becomes unstable and dissociates [34]. The thrusts produced by the opposing filaments cancel each other and the bacterium jiggles around its center of mass without significant displacement in one direction. The cell is said to perform a ‚tumble' or ‚turn' (figure 3.3(right)). Additionally, because of viscous drag and the sudden change in the direction of rotation, the filaments can undergo polymorphic transitions, which alter the pitch, the radius, and

even the handedness of the helix from left- to right-handed ([34], see below for a more detailed description).

For stable bundle formation to occur, rotating nearby filaments have to be attracted by each other and rotate in a synchronous fashion. Regarding bundle formation, two different scenarios have been proposed [86]: In the first scenario, hydrodynamic drag on the swimming cell naturally forces the filaments to trail behind the cell body. As the cell body rotates in CW-direction to balance the torque of the filaments, the left-handed helical filaments anchored to it are passively wrapped around each other and form a bundle [120]. In the second scenario, which relies on the semi-flexible property of the filaments, a filament induces a flow which causes the neighboring helix to bend and twist. Whether the hydrodynamic interactions lead to a stable bundle formation depends on the handedness of the helix and the direction of rotation and is independent of the rotating cell body [76, 100]. In an impressive macro-scale experiment with flexible polymer tubes immersed in silicon oil, mimicking flagellar dynamics at a comparable Reynolds number, Kim et al. have shown that left handed helices rotating CCW are attracted by each other and form a stable bundle [76] on a time scale determined by rotation speed. While CW-rotating left handed filaments are still attracted by each other, the forming bundle is periodically distorted and unstable. Synchronization within the rotating bundle has been addressed by numerical simulations. It was shown that phase-locking through hydrodynamic interactions relies on the flexibility of the filaments and does not not occur if helices are perfectly rigid [77, 125].

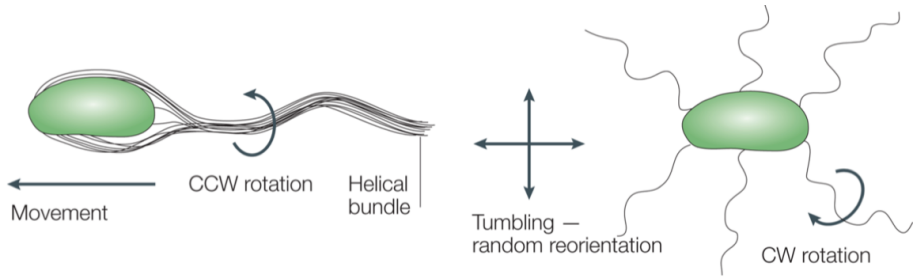

Fig. 3.3: Two swimming modes of a peritrichously flagellated bacterium, where flagella are uniformly distributed across the cell body: (left) flagellar motors rotate counterclockwise (CCW) and filaments form a stable rotating bundle. The cell swims on a straight trajectory (run). (right) Clockwise (CW) rotation of one or several motors causes the bundle to become unstable and induces a random change in direction accompanied by a period of small displacement (tumble). If motors reverse back to CCW-rotation, the cell starts a new run. Illustration taken from [18].

Bacterial flagellum

In figure 3.4 we show the bacterial flagellum which consists of three major parts: the filament, the hook and the basal body with the rotary motor unit, which is rigidly attached to the cell wall. Unlike in eukaryotic cells, where the filament and cilia are actively beating with their motion driven from inside by molecular motors (see [97] for a review), the filament of a bacterium is passive and hollow from inside with an approximate thickness around $20 - 40$ nm. It is generally assumed that each bacterial filament is individually connected to a single motor unit.

In the following description till the end of this section we will focus on the flagellum of the best studied model organism *Escherichia coli* as an example and for the most part comply with the pioneering work by Howard Berg summarized in [11, 12]. The basic structure of the flagellum with filament, hook and motor unit and the principle of the propulsion mechanism is similar for every bacterium. The molecular details of the motor unit responsible for force generation and motor reversal, however, vary from

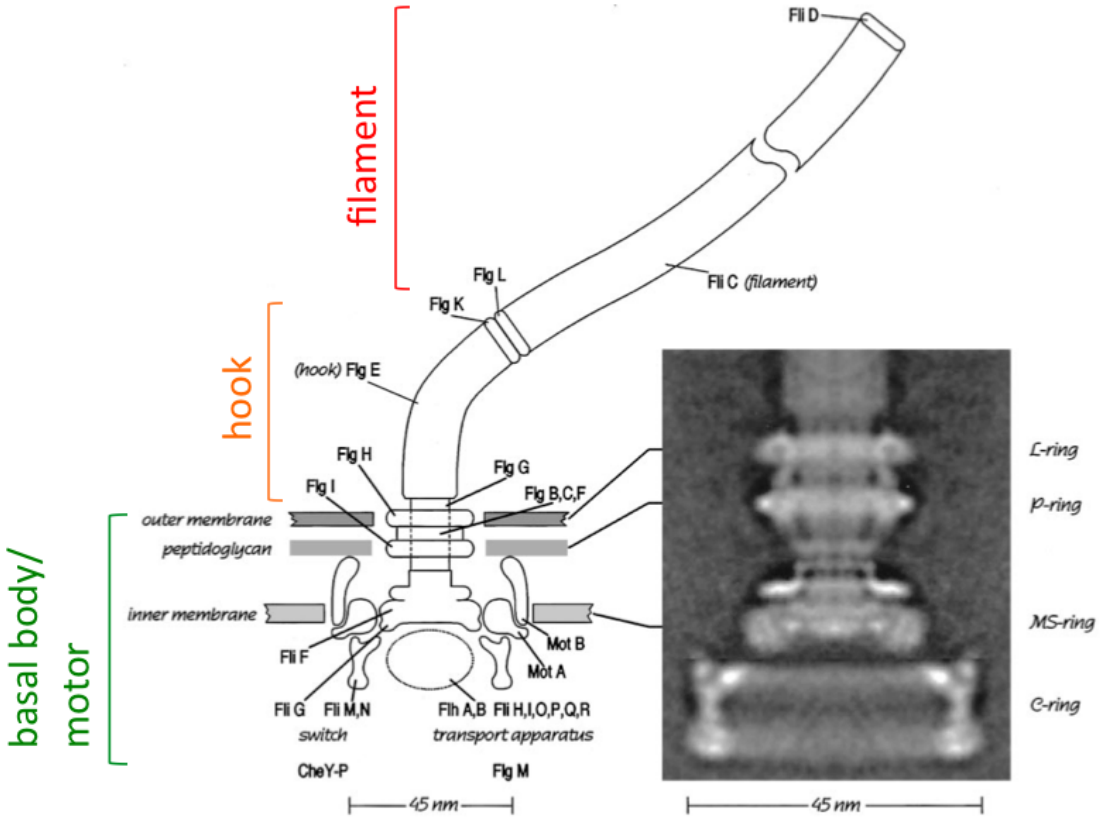

Fig. 3.4: Bacterial flagellum of *E.coli* with filament, hook, and motor assembly in the basal body anchored to the cell wall. See text for description. Picture taken from [12].

species to species.

The hook serves as the primary joint between motor and helical propeller. It is made of about 120 copies of a single protein, FlgE, and due to the nature of its function as a joint, its structure is highly flexible with an elastic bending modulus two orders of magnitude smaller than that of the filament [130]. During a run, filaments form a trailing bundle behind the cell but are anchored at different locations all over the cell body. This is only possible if the rotational motor can transduce torque to the filament even though both are not coaxial [11]. The flexibility of the hook thus allows for large angular deflections to permit synchronous rotation of flagella during a run [95].

Towards the cell body, the flexible hook is coupled to a rigid rod, which itself is attached to four rings, made of FlgB, FlgC, FlgF and FlgG proteins. The outer pair of rings, the L- and P-ring, embedded within the lipopolysacharide and peptidoglycan layer of the cell wall respectively, rotate passively. The inner pair of rings, the MS-ring (membranous-supramembranous-ring) and the C-ring (cytoplasmic ring) together with eight MotA- and MotB- protein complexes form the core unit of the motor, where the actual torque for flagellar propulsion is generated.

Within the motor unit, MotB and MotA proteins act as the stator with MotB being attached to the inner membrane while MS- and C-ring form the rotor. A proton gradient across the cell membrane drives a flux of H^+-ions through channels passing the MotA/MotB interfaces. Each time H^+-ions pass the stator complex, they bind to an acid cite on the MotB protein. Binding to MotB then causes a conformational change in the neighboring MotA protein that results in a power stroke of the protein acting on the MS-ring and moves the rotor incrementally. At the end of the power stroke, the H^+-ion is released from the MotB binding site and causes a second conformational change that drives the rotor another step forward in one direction of rotation.

Proton motive force

The work per unit charge done by a proton by crossing the cell membrane is called the protonmotive force F_P and can be calculated according to

$$F_p = \Delta U - 2.3(k_B T/e)\Delta pH$$

with $\Delta U = U_{in} - U_{out}$ for the electric potential across the membrane, $\Delta pH = pH_{in} - pH_{out}$ for the difference in pH-value across the membrane and $k_B T$ for the Boltzmann constant and temperature [11, 162]. At 24 °C, we have $2.3(k_B T/e) = 59$ mV. Following a calculation by Berg for *E. coli* [11], which maintains an intracellular pH value ranging

from 7.6 to 7.8, we get $F_p \approx -170$ mV ($\Delta U \approx -120$ mV, $-59\Delta pH \approx -50$ mV) for cells swimming in a medium with pH=7.0 and $F_p \approx \Delta\psi \approx -140$ mV for cells swimming in a medium with pH=7.7.

The potential ΔU for the proton gradient across the cell membrane is usually maintained by the metabolism of the cell (e.g. via ion pumps) for which internal energy is consumed. The electric potential can be measured whereas the number of protons passing the membrane is difficult to access. In an experiment by van der Drift et al. [149], a strain of *Streptococcus*, a bacterium that lacks an internal energy source to generate the proton motive force by itself was used to measure the flux of protons. The surrounding medium can then be shifted to a pH-value below the intracellular pH-value. By recording the increase in external pH during swimming, the uptake of protons by the cell can be calculated. Because of the difficulties involved in visualizing rotating flagella, only in later experiments the number of protons could be directly related to the rotation of the flagellar motor [99]. Approximately 1200 protons were counted for a single flagellar rotation. From this number we can calculate the power input P_{in} to the motor of *E.coli*, which is rotating with $\Omega = 10$ Hz and operating in a surrounding medium with pH=7.0 to

$$P_{in} \approx 1200\ |F_p|\ \Omega\ = 2.0 \cdot 10^3 \text{ eV s}^{-1} = 3.2 \cdot 10^5 \text{ pN nm s}^{-1}. \tag{3.1}$$

Using cells that were tethered to a glass coverslip via a single filament and exposed to an electrical field of varying strength, Berg and Turner were able to measure torque and rotation frequency of the flagellar motor [6, 7]. For a flagellum rotating at $\Omega = 10$ Hz they measured a torque of $N = 4600$ pN nm and thus calculated the power output P_{out} of the motor to

$$P_{out} = N\Omega \approx 2.9 \cdot 10^5 \text{ pN nm s}^{-1}. \tag{3.2}$$

From these numbers we get an efficiency of the motor (P_{out}/P_{in}) of approximately 90 %. With the rotor radius measuring 20 nm, one can also calculate the contribution F_u from each of the eight independent force generating MotA/MotB units per individual flagellum. If we assume that the units act on the periphery of the MS-/C-ring we get $F_u = 4600$ pN nm$/(8 \cdot 20$ nm$) \approx 29$ pN. The flagellar motor serves as a prime example for a nanomolecular machine, which operates in tiny, controlled increments (tightly coupled), so that almost all the energy provided from the transmembrane proton flux is converted into mechanical work.

Motor reversal and chemotaxis

In *E.coli* the direction in which the flagellum rotates is controlled via a switch complex (FliG, FliM and FliN) attached to the C-ring. Changes from CW- to CCW rotation and vice versa are induced randomly by thermal fluctuations and become more frequent if the temperature of the surrounding medium increases [87, 148]. At room temperature and in a uniform environment, rotation is biased towards the CCW-state: the motor spends 65% of its time rotating in the CCW-direction, when viewed from the distal end of the filament looking towards the cell body [27, 133]. When the phosphorylated key regulator CheY-P binds to FliM in the switch complex, the CW-state is stabilized. In a non-uniform environment, ligand binding of chemoattractants to receptors distributed across the cell body triggers a downstream signaling cascade that leads to the dephosphorylation, to CheY, and hence to its unbinding from FliM. The CW-state becomes less probable and the average time during which the motor is rotating CCW increases. The cell is less likely to perform a tumble and the run periods become longer. On average, the cell moves up the concentration gradient (chemotaxis).

Polymorphism of flagellar filament

The flagellar filament consists of approximately 20.000 monomers of the molecule FliC, called flagellin, which form 11 helical subunits, called protofilaments. A flagellin monomer can assume two different conformations. Bonding can only occur between two mono-mers of the same conformation and the bonding length of the two possible pairs of monomers differs by approximately 8 Å [11]. During assembly the monomers are transported through the hollow body of the filament and built up the filament by arrangement in a spiral-like staircase forming an 11-start helix. Because every protofilament is built entirely of one sort of monomers in identical conformation we have a long type of a protofilament, called L-type, and a short type of protofilament, called R-type. The final shape of the bacterial filament then depends on the number n_L of L-type protofilaments and the corresponding number $n_R = 11 - n_L$ of R-type protofilaments, which together form the 11-start helix. A filament made entirely of L-type protofilaments ($n_L = 11$) is straight with a left-handed helical structure while it has a right handed helical structure when assembled from R-type protofilaments only ($n_R = 11$). If the filament is assembled by protofilaments of different lengths, short protofilaments arrange together and cause the structure to bend. Flagellin molecules in neighboring protofilaments displace relative to each other along the axis of the filament causing the structure to twist [152]. The amount of bending and twisting then determines the characteristic

helical shape or polymorphism of the filament.

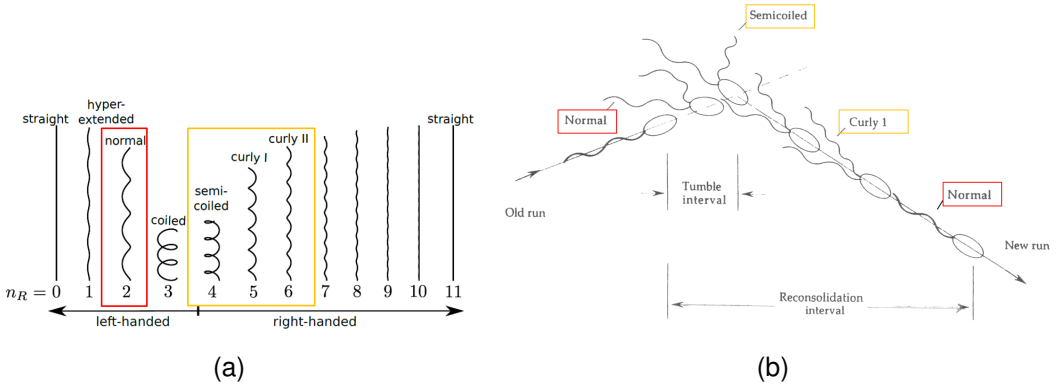

(a) (b)

Fig. 3.5: (a) Possible filament configurations (polymorphisms) predicted by [19]. Depending on the number of R-type protofilaments n_R, the filament is either straight or forms a left handed or right handed helix with varying pitch and radius. Picture taken from [152]. (b) Polymorphic transition of *E.coli* flagellar filament during tumbling. During forward swimming, the filament is in state 2 (normal state). Mechanical forces due to motor reversal from CCW to CW induce a transformation to a right-handed, semicoiled and then curly I filament (state 4 and 5). Upon reversal to CCW-rotation the tumbling ends and with the new run the filament transforms back into the normal state. Picture taken from [11].

In figure 3.5(a) we show different stable polymorphic forms of the filament as a function of the number n_R of short protofilaments according to theoretical predictions by Calldine from elastic theory [19]. Transformations between the different forms are called polymorphic transitions and can occur because of changes in pH-value or ionic strength of the surrounding medium but can also be triggered by mechanical twist due to hydrodynamic forces during propulsion [11]. The latter is particularly important for the transition between run- and tumble modes of a swimming cell.

In figure 3.5(b) we show a cell undergoing a typical tumble event [11]. During the run the helical flagella are in the left-handed normal state (state 2 in figure 3.5(a)), generate thrust by CCW-rotation, and push the cell forward. A tumbling is initiated by a reversal to CW-rotation in one or several of the motors. The corresponding filament experiences a mechanical force due to the sudden increase in drag by the surrounding fluid and its orientation changes from a left handed to a right handed helix. It undergoes a polymorphic transition from a semicoiled to a curly form (state 4 and state 5 in figure 3.5(a)). Both states still generate forward thrust when rotating CW but at a lower magnitude because helical pitch and radius have changed (see section 3.4). The bundle of flagella becomes unstable and the cell body changes direction. After the flagellar

motor switches back to CCW-rotation the filament transforms back to the normal, left-handed state 2. The bundle reconstitutes, the period of tumbling ends and a new run is initiated [34, 146].

3.2 *Pseudomonas putida*

In this work, our model organism *Pseudomonas putida* (*P. putida*) KT2440 belongs to the family of *Pseudonomads* and is a gram-negative, rod-shaped soil bacterium. In the presence of a surface, even under toxic environmental conditions, *P. putida* is capable of attachment, colony formation, and phenotype change towards biofilm development [54, 80]. In the bulk fluid or the porous soil environment, it swims by using a so called ‚lophotrichous' arrangement of flagella. Unlike in E. coli, where flagella are uniformly distributed across the cell body (peritrichous flagellation), in *P. putida*, between three and seven flagella are inserted at one polar end of the cell, where they form a tuft (see figure 3.6, [64]). In its environmental niche, *P. putida* colonizes plant roots [46] and lives from secreted aromatic acids, forming a synergetic relationship with its host by serving as an antagonist to plant diseases [47]. Unlike *Pseudomonas aeruginosa*, another common model organism for biofilm formation [81], which can cause severe lung infections, there is no evidence for a pathogenic relationship neither with plants, animals nor humans.

Because of the extreme heterogeneity of its soil environment regarding temperature, pH-value, ionic strength, availability of oxygen, and the chemistry of possible carbon or nitrogen sources, *P. putida* has developed as an extremely versatile and robust microorganism [142, 154]. It is resistant to antibiotics, detergents, and heavy metals and its strains are often found in polluted soils. The regulatory network can switch the metabolism of the cell to recycle disparate organic molecules. *P. putida* can oxidize aromatic hydrocarbons like phenol and toluol and it can grow on more than 80 different organic compounds [39]. Because of its ability to degrade organic substances and detoxify polluted environments, *P. putida* became the worlds first patented microorganism. Its genom has been fully sequenced [113, 124] and current biotechnological applications use *P. putida* to design new catabolic pathways for pollutants [142], to desulfurize fuel [52], or to design herbicides and insecticides, which are degradable with the help of *P. putida* metabolism [154]. The highly adaptive nature of *P. putida* is also reflected by the fact that it can express different chemotactic receptors corresponding to the aromatic compounds of its growth medium [65, 83]. Swimming cells are able to use these receptors to monitor the surrounding concentration of the respective substance

and direct their random walk towards local concentration gradients (chemotaxis).

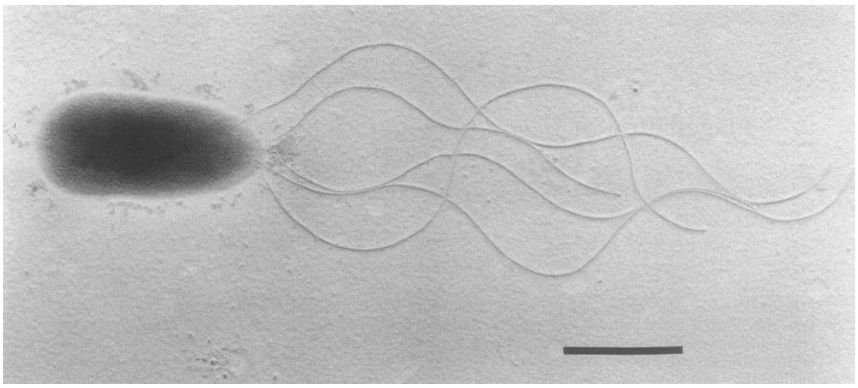

Fig. 3.6: Electron Microscopy picture of *Pseudomonas putida* PRS2000: between 3 and 7 flagella are attached in a tuft at one end of the cell body (lophotrichous arrangement), measuring $7-10$ μm in length (two to three wavelengths). Scale bar is 1 μm, taken from [64].

Apart from its importance in biotechnology because of its ‚arsenal of degradative functions' [142], in the present work *P. putida* was employed as a robust, rapidly growing, nonpathogenic and therefore easy to handle model bacterium which can swim and at the same time form biofilms at solid-liquid interfaces within our microfluidic devices.

Bacterial swimming pattern depends on flagellation

In section 3.1.2 swimming motility and flagellar propulsion mechanism of a bacterium were generally discussed based on the well studied model bacterium *E. coli*. In particular the distinct pattern of the swimming trajectory however depends critically on the number and arrangement of a bacterium's flagella. The classical swimming pattern with run-tumble motion has been observed in peritrichously flagellated bacteria like *E. coli*, where several flagella are uniformly distributed across the cell body (see figure 3.7(a)). Straight line segments and random reorientations during tumbling events alternate. In bacteria which are equipped with a single polar flagellum like the marine bacterium *Vibrio algynolyticus* (*V. alginolyticus*), a motor reversal of the left-handed flagellum from CCW to CW rotation and vice versa induces a reversal in swimming direction and the cell thus alternates between a 'forward' and 'backward' swimming mode [103]. Until the motor reverses back to CCW rotation, the cell is swimming as a 'puller' with the flagellum pointing towards the swimming direction. The corresponding trajectory of the cell shows a 'zigzag' pattern, where straight runs are interrupted by frequent reversals in swimming direction. Recently this picture has been refined by Xi et al. who found that upon resuming to CCW rotation the flagellum of *V. alginolyticus* performs a distinct

'flick' which leads to an additional randomization of the swimming direction [161]. The cell trajectory display a characteristic 'run-reverse-flick' swimming pattern (see figure 3.7(b)).

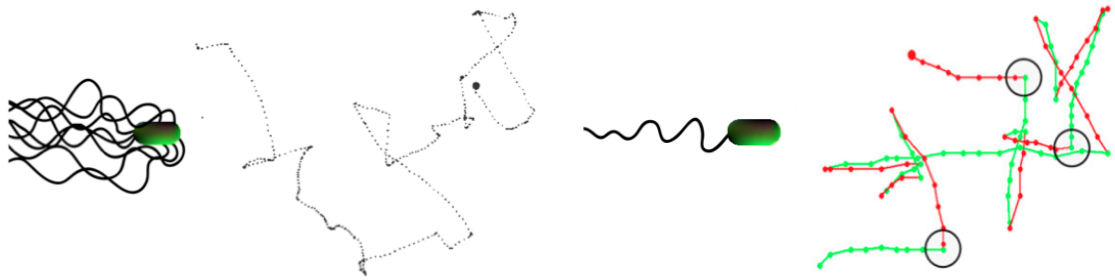

(a) (b)

Fig. 3.7: Characteristic swimming pattern of two bacteria with different flagellation. (a) Trajectory of a peritrichously flagellated bacterium (here *E. coli*): straight lines and random reorientations alternate ('run-tumble' pattern). Picture taken from [8]. (b) Trajectory of a monoflagellated bacterium (here *V. alginolyticus*): straight runs, trajectory reversals and reorientation events alternate ('run-reverse-flick' pattern). Picture taken from [161].

Compared to the well studied cases of peritrichous and monotrichous flagellation, *P. putida* can be considered as a somewhat intermediate case, a bacterium which has several flagella but polarly attached at one end of the cell body (see figure 3.6). The fact that few experimental studies are available on the swimming pattern of such a lophotrichously flagellated bacterium further motivated parts of this work. In section 5.1 and section 5.2 we will present a systematic analysis of the swimming pattern of *P. putida* in the bulk fluid and near a solid boundary.

3.3 Hydrodynamics at low Reynolds numbers

3.3.1 Navier-Stokes equation

In the absence of an external force the flow field $\boldsymbol{u}$ of an incompressible, Newtonian fluid is related to the local pressure gradient ∇p via the Navier-Stokes equation

$$\rho\left(\frac{\partial \boldsymbol{u}}{\partial t}+\boldsymbol{u}\cdot\nabla\boldsymbol{u}\right)=-\nabla p+\eta\nabla^2\boldsymbol{u} \tag{3.3}$$

with ρ and η for the fluid density and dynamic viscosity. The flow field $\boldsymbol{u}$ has to satisfy the continuity equation

$$\nabla \cdot \boldsymbol{u} = 0. \tag{3.4}$$

If we scale this equation by a characteristic length L, a characteristic velocity U and a characteristic time $T = L/U$, writing

$$\boldsymbol{u}' = \frac{\boldsymbol{u}}{U} \ , t' = \frac{t}{T}$$

we get the non-dimensional form of the Navier-Stokes equation

$$Re\left(\frac{\partial \boldsymbol{u}'}{\partial t'} + \boldsymbol{u}' \cdot \nabla \boldsymbol{u}'\right) = -\nabla p' + \eta \nabla^2 \boldsymbol{u}' \tag{3.5}$$

with

$$p' = \frac{pL}{\eta U} \quad , \quad Re = \frac{\rho U L}{\eta}.$$

The Reynolds number Re is a dimensionless quantity that allows for qualitative predictions on the nature of the flow regime [78, 144]. When looking at a steady flow with a mean velocity U around an object of size L in the absence of an external force, in its most common physical interpretation the Reynolds number is defined as the ratio of the inertial term in the Navier-Stokes equation (left-hand side) to the viscous forces per unit volume (right-hand side)

$$Re = \frac{\text{inertia forces}}{\text{viscous forces}} = \frac{|\rho \boldsymbol{u} \nabla \boldsymbol{u}|}{|\eta \nabla^2 \boldsymbol{u}|} \sim \frac{\rho U L}{\eta}. \tag{3.6}$$

One can also interpret the Reynolds number as the ratio of the forces acting on the object [86]. With the typical inertial stress given by the dynamic pressure in the Bernoulli equation of momentum conservation, $\sigma_{\text{inertial}} \sim \rho\, U^2$, we can then estimate the inertial force acting on the area of the object to $f_{\text{intertial}} \sim \sigma_{\text{intertial}} L^2 = \rho\, U^2 L^2$. The viscous stress is proportional to shear rate and dynamic viscosity, $\sigma_{\text{viscous}} \sim \eta\, U/L$, from which we get a typical viscous force of $f_{\text{viscous}} \sim \sigma_{\text{viscous}} L^2 \sim \eta\, UL$. The Reynold-number is thus $Re = f_{\text{inertial}}/f_{\text{viscous}}$, the ratio of inertial and viscous forces acting on the object.

A third interpretation was given by Purcell, who noticed that $\mathcal{F} = \eta^2/\rho$ has units of force [122]. Rearranging equation 3.6 then gives

$$Re = \mathcal{F}^{-1}\rho\, UL = \frac{f_{\text{viscous}}}{\mathcal{F}} \quad \text{and} \quad Re = \sqrt{\mathcal{F}} \cdot \sqrt{\rho\, U^2 L^2} = \left(\frac{f_{\text{inertial}}}{\mathcal{F}}\right)^{1/2}.$$

Subjected to a force $\mathcal{F}$ a body at arbitrary size will experience a Reynolds number of unity ($f_{\text{inertial}} = f_{\text{viscous}} = \mathcal{F}$). If the body experiences a force smaller than $\mathcal{F}$ we have $Re < 1$ and viscous forces dominate its motion. For a body immersed in water this characteristic force is $\mathcal{F} \approx 1$ nN.

For a bacterium with a cell body length $L \approx 1$ μm swimming in water ($\rho \approx 10^3$ kg m^{-3}, $\eta \approx 10^{-3}$Pa s) at a velocity $U \approx 10$ μm/s we get a Reynolds number on the order of $Re \approx 10^{-5}$. At this very low Reynolds number, the inertial term in the Navier-Stokes equation can be neglected and equation 3.5 for a stationary flow simplifies to

$$\nabla p = \eta \nabla^2 \boldsymbol{u}, \tag{3.7}$$

the so called Stokes equation for the flow field in an environment where viscous forces dominate over inertial forces. In the low Reynolds number regime, the governing hydrodynamic equation is thus drastically simplified. At every point in the fluid there is a balance between local pressure gradient and viscous forces [144]. Due to its linear nature, for the Stokes equation analytic solutions can be found which usually cannot be obtained for the full, nonlinear Navier-Stokes equation.

For us, two characteristic features of the Stokes equation are important [63, 144]: First, the solutions of the Stokes equation are reversible. This means that for a given solution, there exists another one with the same streamlines but with the flow field now pointing in the opposite direction where the pressure gradient has changed sign. This has important consequences for the propulsion mechanism of a swimming microorganism, which we will explain in section 3.3.2. In short, bacteria cannot use appendages moving with time-reversal symmetry to generate thrust. The second important feature is that in low Reynolds number flow, the range of spatial interactions in the fluid is large. The spherical body of a swimming cell is affected by the presence of a rigid wall with no-slip boundary condition or by the presence of another swimming cell even if the distance between the two is large compared to the characteristic size of the cell. In section 3.3.3 we will discuss implications of these hydrodynamic interactions on the speed and propulsion mechanism of a cell swimming close to a boundary.

The movement in the low Reynolds number world is very different from the physical intuition we have from swimming of animals and humans, which move at a higher Reynolds number. This can be demonstrated by considering the coasting distance, the typical

length scale l, over which a body with mass $m = \rho_s L^3$ and swimming with a velocity U comes to rest due to the drag of the surrounding fluid [86]. At $Re > 1$, with $f_{\text{drag}} = f_{\text{inertia}} \sim \rho\ U^2 L^2$ (see above) and Newtons second law, we can estimate the deceleration of the body to $a \sim \rho U^2 L^2 / \rho_s L^3$ and thus the coasting distance to

$$l \sim \frac{U^2}{a} \sim \frac{\rho_s L}{\rho}.$$

The dimensionless coasting distance is on the order of the ratio between the density of the swimmer and the density of the surrounding fluid. A human swimmer making a breaststroke will coast for a couple of meters, several times the length of its body. At $Re \ll 1$, viscous drag dominates, $f_{\text{drag}} = f_{\text{viscous}} \sim \eta U L$ (see above). Analogously we then calculate a coasting distance

$$l \sim Re \frac{\rho_s L}{\rho}.$$

For a bacterium swimming in water we obtain $l \approx 1$ nm, not even a thousandth part of the cell body length [122]. At low Reynolds number, the inertia of a moving body is dissipated virtually instantaneously and all momentum and energy is transferred to the molecular movement of the surrounding fluid. A Microorganism behaves as a macroscopic object swimming through viscous syrup. If the propulsion mechanism is switched off, the cell stops within a couple of nanoseconds.

3.3.2 Flagellar propulsion

In his seminal work, Purcell answered the question about the simplest possible propulsion mechanism necessary to generate movement for a swimmer at low Reynolds number [122]. We can imagine a body with one degree of freedom, consisting of two rods (in two dimensions) or consisting of two paddles (in three dimensions) which are connected by a joint. At high Reynolds number, this body can generate propulsion and move like a scallop in sea water by periodically opening and closing the hood. This is possible if one of the two cyclic steps (opening or closing) is executed faster than the other, the moment of inertia generated from one stroke is higher than the opposing moment generated from the thrust of the counterstroke. At low Reynolds number, however, we know that inertial forces are dissipated instantaneously. Locomotion is therefore *rate independent*, i.e. independent of the speed during which the shape deformation of the swimmer body occurs, it depends only on the geometry of the deformation itself [95]. In both power strokes the scallop generates thrust of the same magnitude but with opposing sign generating zero net propulsion. Because of the time symmetry in the Stokes equation (see section 3.3) any motion which is reciprocal, meaning that any sequence of shape changes, which is invariant under time reversal, cannot generate net propulsion (movement with one degree of freedom is always reciprocal) [122]. Appendages of a swimming microorganism must therefore have at least two degrees of freedom, deform periodically and in a non-reciprocal way to create net motion. In the next part we will derive expressions, which relate the torque and thrust force generated by a helical flagellum to the movement of a bacterium at low Reynolds numbers, following a formalism which has been introduced by Purcell [122].

Propulsion matrix formalism

A bacterium swims by rotating one or several filaments which are connected to the cell body. Following Purcell we approximate the stable flagellar bundle by a single, rotating filament and neglect any further hydrodynamic interaction between the filament and the body of the cell [122]. Because of the linearity of the Stokes equation, angular velocity ω and translational velocity v of the filament are linearly related to the thrust force and torque generated by the filament.

We can write the thrust force

$$-F_{\mathrm{fl}} = Av - B\omega \tag{3.8}$$

with A for the translational drag coefficient of the filament and the torque

$$N_{\text{fl}} = -Bv + D\omega \tag{3.9}$$

with D for the rotational drag coefficient experienced by the filament (see figure 3.8(b) and (d)). The constant B can be understood if we consider the force necessary to prevent a rotating helix from translating (contribution to the propulsion force in equation 3.8) or the moment necessary to prevent a translating helix from rotating (contribution to the generated moment in equation 3.9) [86, 95]. Note that ω and N_{fl} obey the right hand rule for a left-handed helix and that the sign in front of the coupling constant B is determined by the orientation of the helix [95, 122]. Here the helix generates positive thrust pushing on the cell body when rotating counterclockwise. We are only dealing with the magnitudes of thrust forces and torques and the arrows in figure 3.8 symbolize the corresponding directions. The two equations can be summarized as

$$\begin{pmatrix} -F_{\text{fl}} \\ N_{\text{fl}} \end{pmatrix} = \begin{pmatrix} A & -B \\ -B & D \end{pmatrix} \begin{pmatrix} v \\ \omega \end{pmatrix}. \tag{3.10}$$

This 2 x 2 matrix is known as the propulsion or resistance matrix [63, 121]. The coefficients A, B and D are positive and depend on the wavelength or pitch, the radius and the thickness of the helical filament. Depending on whether long range hydrodynamic interactions between the individual segments of the filament were taken into account or not, their value was approximated using slender body theory or resistive force theory (see below).

Analogously we determine the force and moment acting on the cell body (see figure 3.8(a) and (c))) to

$$F_{\text{bd}} = -A_0 v \tag{3.11}$$

and

$$N_{\text{bd}} = -D_0 \Omega \tag{3.12}$$

with $A_0 = 4\pi\eta b/(\ln(2b/a) - 1/2)$ for the translational drag coefficient and $D_0 = 16\pi\eta a^2 b/3$ for the rotational drag coefficient [6]. Here we treat the cell body as a prolate ellipsoid with its two major axis a and b and η for the viscosity of the surrounding fluid. Written as a matrix equation we obtain

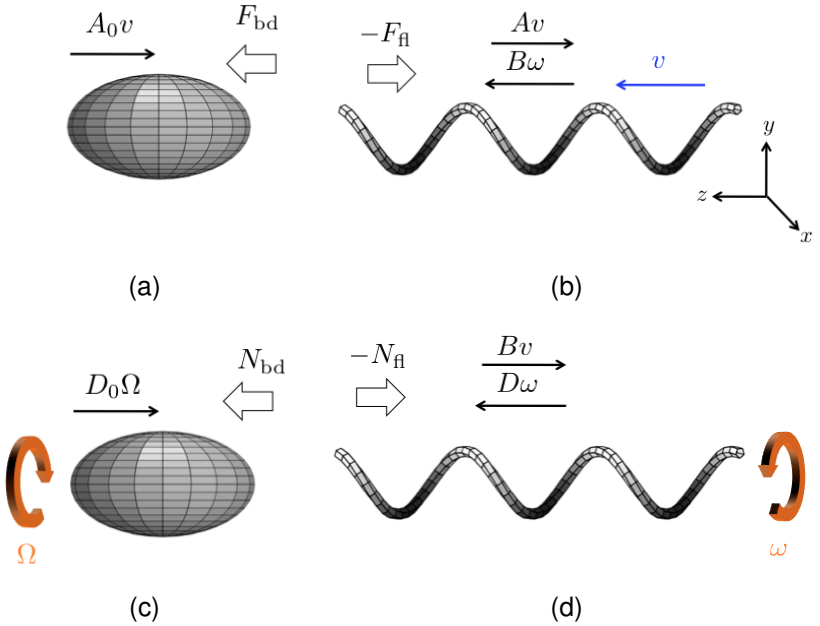

Fig. 3.8: Propulsion matrix formalism first proposed by Purcell [121] for cell body (a) and (c) and helical filament (b) and (d): The left-handed filament rotating with ω generates a thrust force $B\omega$ pushing the cell body with velocity v and experiences an opposing translational drag $-Av$ (b). The thrust force is balanced by the translational drag acting on the cell body $A_0 v$ (a). Analogously, the moment generated by the rotating filament $D\omega - Bv$ (d) is balanced by the counter-rotational drag of the cell body $D_0\Omega$ (c). See text for summarizing description. Adapted from [95].

$$\begin{pmatrix} F_{\mathrm{bd}} \\ N_{\mathrm{bd}} \end{pmatrix} = \begin{pmatrix} -A_0 & 0 \\ 0 & -D_0 \end{pmatrix} \begin{pmatrix} v \\ \Omega \end{pmatrix}, \tag{3.13}$$

the propulsion matrix of the cell body. Unlike the filament the cell body is not self-propelled, therefore the coupling constants vanish and the matrix is diagonal. Note that the cell body's rotation rate Ω is different from the rotational frequency of the flagellum ω. For most cells, the drag opposing rotation of the cell body is higher than the one acting on the filament so that in most cases $\omega > \Omega$.

For a self-propelling bacterium swimming at constant velocity v, in the absence of external forces, the thrust force must equal the viscous drag experienced by the cell body ($F_{\mathrm{bd}} = -F_{\mathrm{fl}}$) and the torque must be balanced by the drag on the rotating cell body ($N_{\mathrm{bd}} = -N_{\mathrm{fl}}$). Following this principle and using equation 3.10 and equation 3.13 we receive

$$(A + A_0)v = B\omega \tag{3.14}$$

and

$$D_0\Omega = -Bv + D\omega. \tag{3.15}$$

These expressions are commonly used to determine a cell's speed, rotation rate or the torque of its flagellar motor when only two of these quantities are directly accessible via experimental techniques [84, 104]. They typically rely on fixing a bacterium in an optical trap under various flow conditions [21]. Additionally, research tries to provide experimental data to accurately determine the drag coefficients, in particular A, B, and D resulting from the complex helical geometry of the flagella which can undergo transitions depending on the swimming conditions [22, 34, 103].

Resistive force theory

In the following we want to calculate the total drag force and moment induced by a rotating helical filament, in other words give a theoretical estimate on the coefficients A, B, and D in the propulsion matrix formalism which depend on the exact geometry of the filament. This theory has been pioneered by Gray and Hancock in 1955, who modeled the propulsion mechanism of the sea-urchin spermatozoa by a wave traveling through viscous fluid [56, 57]. The main idea is that the helical flagellum, which is characterized by its length L, wavelength λ and radius R, rotating with frequency ω (see figure 3.9(a)) is divided into individual segments of cylindrical rods with length D and radius r (see figure 3.9(b)). The individual segments do not interact with each other and there is no long range interaction with the body of the cell. As the helix rotates, each segment is dragged through the fluid with a given velocity and experiences a hydrodynamic drag force parallel and perpendicular to the axis of the rod. Being in the Stokes-regime, the relationship between the velocity of the segment and the drag force exerted on the fluid is linear, which is why this approach has been termed resistive force theory (RFT) or more accurately local resistive force theory (LRFT). The total propulsion force and moment generated by the helix is then calculated by summing over the drag per unit length of all individual segments [20].

In figure 3.9(b), a segment of the flagellum is depicted. We consider it as a straight rod, inclined at a helical pitch angle of $\varphi = \arctan(R/(\lambda/2))$ with the z-axis and moving with a velocity $\boldsymbol{u}$. The velocity decomposes into the two components $u_{\parallel}$ and $u_{\perp}$ parallel

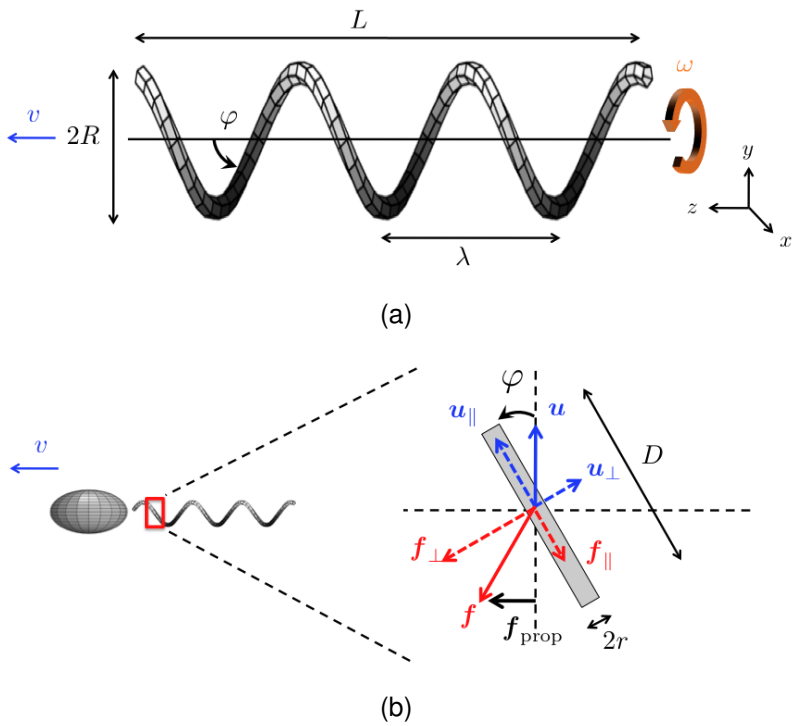

Fig. 3.9: Drag based propulsion modeled by resistive force theory: (a) the helical filament is composed of a series of rod-shaped segments and characterized by its length L, radius R and wavelength λ with φ for the pitch angle of the linear segment with respect to the swimming axis. (b) Within a helix rotating at ω, the individual segment is actuated with a velocity $\boldsymbol{u}$ perpendicular to the z-axis which can be decomposed into a parallel and a perpendicular component. The rod experiences local drag by the surrounding fluid $f_{\parallel} = -\zeta_{\parallel} u_{\parallel}$ and $f_{\perp} = -\zeta_{\perp} u_{\perp}$. Because of asymmetric drag, $\zeta_{\perp} > \zeta_{\parallel}$, a net propulsion force is generated. The total propulsion force can be calculated by summing over the local drag of all individual segments. Adapted from [86] and [95].

and perpendicular to the orientation of the rod. The drag per unit length along the two components then becomes $f_{\parallel} = -\zeta_{\parallel} u_{\parallel} = -\zeta_{\parallel} u \cos\varphi$ and $f_{\perp} = -\zeta_{\perp} u_{\perp} = -\zeta_{\perp} u \sin\varphi$, with $\zeta_{\parallel}$ and $\zeta_{\perp}$ for the drag coefficients experienced if the rod is pulled through the fluid parallel or perpendicular with respect to its principal axis. For the drag force parallel to the z-axis and perpendicular to the velocity of the rod, we get

$$\boldsymbol{f}_{\text{prop}} = (\zeta_{\parallel} - \zeta_{\perp}) u \sin\varphi \cos\varphi \boldsymbol{e}_z \tag{3.16}$$

, which is the amount of forward thrust generated by an individual rod segment of the helix [86]. If the drag on the filament was isotropic ($\zeta_{\parallel} = \zeta_{\perp}$), no forward thrust would be created. The tangential and normal drag coefficients for a rod being pulled through a

fluid have been first calculated by Gray et al. [57], while we use a more accurate form which was presented by Lighthill in 1975 (see [96] for a full derivation):

$$\zeta_{\parallel} = \frac{2\pi\eta}{\ln(2D/r) - 1/2} \tag{3.17}$$

$$\zeta_{\perp} = \frac{4\pi\eta}{\ln(2D/r) + 1/2} \tag{3.18}$$

The drag experienced by a rod moving perpendicular to its principal axis is approximately two times higher than the one for movement parallel to its principal axis ($\zeta_{\perp}/\zeta_{\parallel} \approx 2$). Additionally we can see from equation 3.16 that to generate thrust with a periodic motion, both velocity and orientation angle have to change sign periodically [86, 95]. If the velocity changes $\boldsymbol{u} \to -\boldsymbol{u}$ and orientation angle changes $\psi \to \pi - \varphi$, the sign of the propulsive force is constant while periodically changing only $\boldsymbol{u} \to -\boldsymbol{u}$ with constant φ leads to alternating sign in $\boldsymbol{f}_{\text{prop}}$ and does not generate net displacement. Bacteria use a rotating appendage with a helical geometry which fullfills the conditions for propulsion. The drag experienced by the rod segments of the helix is asymmetric ($\zeta_{\parallel} \neq \zeta_{\perp}$) and because of the rotation around the z-axis, both velocity and orientation angle of the segments change sign. The motion of the filament is periodic but non-reciprocal.

With the local drag coefficients given, one can obtain the coefficients for the propulsion matrix by integrating over the length of the flagellum under the conditions that the length of the individual segment is bigger than the radius of the filament but smaller than its wavelength ($r \ll D \ll \lambda$):

$$A = \zeta_{\perp} L(1-\beta^2)\left(1 + \gamma\frac{\beta^2}{1-\beta^2}\right) \tag{3.19}$$

$$B = \zeta_{\perp}\left(\frac{\lambda}{2\pi}\right)\left(1-\beta^2\right)(1-\gamma) \tag{3.20}$$

$$D = \zeta_{\perp} L\left(\frac{\lambda}{2\pi}\right)^2\left(1-\beta^2\right)\left(1 + \gamma\frac{\beta^2-1}{\beta^2}\right) \tag{3.21}$$

The calculation can be found in full detail in [96] and in the thesis by Chattopadhyay [20]. Here, $\beta = \cos^2\varphi$, with φ being the pitch angle of the helix relative to the z-axis (see figure 3.9(a)) and $\gamma = \zeta_{\parallel}/\zeta_{\perp}$ ($\gamma < 1$) for the ratio between the parallel and the perpendicular local drag coefficient. As explained above, if the helical segments experiences symmetric drag ($\gamma \to 1$) we will have $B \to 0$ and $v \to 0$ (see equation 3.14). The helix loses its ability to generate forward propulsion [21].

With all coefficients in the propulsion matrix for both the helical filament and the cell body modeled as a prolate spheroid at hand (equation 3.14 and equation 3.15), Chattopaday et al. [22] calculated a total thrust force of ≈ 0.57 pN for the flagellar bundle of *E. coli*. This is consistent with experimental values determined from swimming cells suggesting an average thrust force between $0.25 - 0.85$ pN [34]. With these values also the propulsion power can be calculated and compared with equation 3.2 at the beginning of this chapter. It was found that in general the efficiency of propulsion (P_{prop}/P_{out}) by a rotating propeller is very small. Less than 3% of the power generated by the motor unit is converted into energy for the locomotion of a swimming bacterium [21].

3.3.3 Swimming near solid boundaries

The previous section has focused on the propulsion mechanism of bacteria which can be understood best when considering free-swimming cells in the bulk fluid and in the absence of external forces. In a confined environment near solid boundaries, because of the no-slip boundary condition, hydrodynamic stresses acting on the cell change as compared to the bulk fluid case and can have a significant impact on its swimming motility [86]. Wall effects on cell locomotion are important for understanding the swimming behavior of bacteria that naturally live in confined environments, in particular our model organism *P. putida* growing in porous soils. They play a role in surface-related bacterial infections and are important for understanding the early attachment and transition to the sessile lifestyle during biofilm formation (see section 3.1.1). In the following we want to first describe the three most important aspects of locomotion near a solid boundary, which were summarized in the excellent review by Lauga et al. [86], namely the effect on (1) a cell's swimming speed, (2) the curvature of its trajectory, and (3) the orientation of its principal axis with respect to the wall.

Effect on speed, curvature, and cell orientation

The flow field induced by a cell swimming in the bulk or near a surface can be approximated in first order by a force dipole [86]. If the cell is swimming as a 'pusher', which means that it is propagating with its cell body ahead and with the flagellar bundle generating thrust from behind, the force dipole is positive. Flagella and body create a flow field pointing away from the cell along its swimming direction and pointing towards the cell at its sides (see figure 3.10(a)). As it has been observed primarly in monoflagellated bacteria, flagella can switch direction of rotation, and the cell can also swim as

a 'puller'. This means that the cells is swimming with its flagella pointing towards its direction of motion and the cell body now being dragged behind. In this case, the force dipol is negative. Along the swimming direction the flow field is pointing towards the cell and away from the cell at its sides (see figure 3.10(b)).

In the presence of a wall, the viscous drag (A_0 in equation 3.13) experienced by the body of the cell increases with decreasing distance d to the wall because of the no-slip boundary condition at the interface. Usually one would therefore expect that the swimming speed v decreases (see equation 3.14). However, as the cell approaches the boundary, the drag based propulsion mechanism of the rotating filament generating forward thrust, $B\omega$, is also affected. The value of the coefficient B is determined by the ratio of the drag per unit length, $\zeta_\perp$ and $\zeta_\parallel$, for moving a segment of the rotating helix tangential or normal to its principal axis (see equation 3.20). With decreasing d, $\zeta_\parallel$ increases but the increase in $\zeta_\perp$ may be even stronger leading to a higher value for B in the vicinity of the wall [75]. The generated thrust $B\omega$ is then higher near the boundary, provided that the flagellar motor has a sufficient reserve in torque to allow for a power increase and continues to rotate the flagellum at a constant velocity ω. The increase in propulsion counterbalances the increased resistance experienced by the cell body. The cell is swimming faster near the boundary than in the bulk fluid. Assuming that motor power is constant, ω will decrease and a cell will swim slower near a boundary as soon as it enters the regime where viscous drag on the cell body increases.

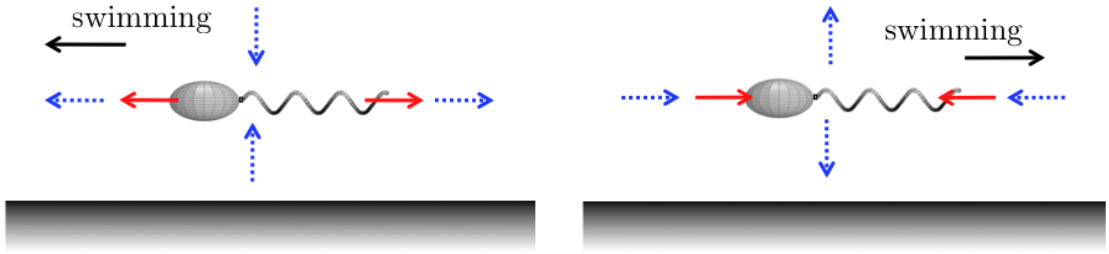

Fig. 3.10: Flow field induced by a swimming cell in the 'push' and 'pull' mode: (a) for a cell moving as a pusher with its cell body pointing ahead, the flow field can be described by a positive force dipol (red arrows). Along the swimming axis, fluid is pushed away from the cell (blue arrows). In lateral direction, the flow field is pointing towards the cell body. (b) For a cell swimming as a puller, the flagellar bundle is pointing towards the direction of propagation. The flow field can be modeled as a negative force dipol. Along the cell axis, fluid is attracted towards the cell while it is pushed away from the cell in the lateral direction. Adapted from [86].

The second hydrodynamic surface effect acts on the shape of the cell trajectories. In the bulk fluid far away from the surface, the rotation of the flagellar bundle in CCW-direction is balanced by a counterrotation of the cell body in CW-direction. The swimming bacterium is torque free. As the bacterium approaches a single boundary from one side, the axial symmetry of the rotational drag experienced by cell body and flagellum is broken. Resistance against rotation for the lower half ellipsoid and helix closer to the boundary is higher as indicated by the different length of the gray arrows for $\boldsymbol{F}_{\text{top}}$ and $\boldsymbol{F}_{\text{bottom}}$ in figure 3.11(b). When looking from behind at a cell swimming parallel to the surface, the clockwise rotating cell body will then experience a net force $\boldsymbol{F}_b$ by the fluid pointing to the right in negative x-direction while the helix rotating counterclockwise will experience a net force $\boldsymbol{F}_l$ pointing to the left (here in positive x-direction) (see figure 3.11(b)). The forces $\boldsymbol{F}_b$ and $\boldsymbol{F}_l$ act in opposing directions and induce a torque on the cell. In superposition with the velocity vector $\boldsymbol{v}$, this leads the cell to perform a right-turn and describe a clockwise-circular path when looking at the surface from above (figure 3.11(a)).

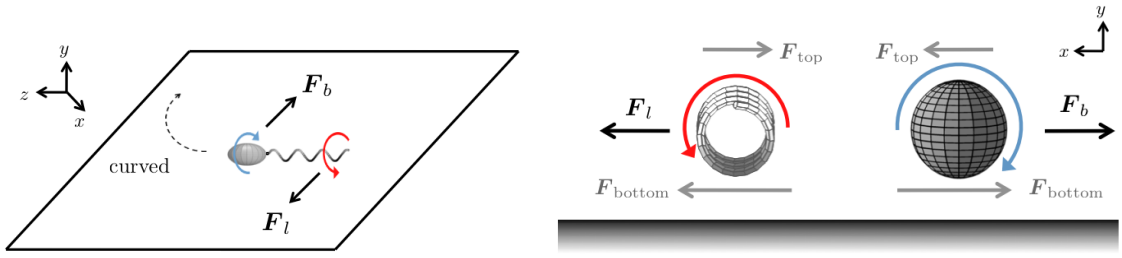

(a) (b)

Fig. 3.11: Hydrodynamic wall effect on the trajectory of a cell swimming in the pusher mode parallel to a solid boundary with body and flagellar bundle rotating in opposing directions. (b) View from behind: near the boundary, fluid is pushed against the wall by the rotating objects. The cell body rotating in CW direction experiences a counterforce $\boldsymbol{F}_b$ pointing to the right, the flagellar bundle rotating in CCW direction experience a counterforce $\boldsymbol{F}_l$ to the left. (a) The opposing forces $\boldsymbol{F}_b$ and $\boldsymbol{F}_l$ generate a torque. When superposed with the velocity, the cell describes a right-turn, a clockwise circular trajectory when viewed from the top. Adapted from [102].

The third effect depends on the orientation of the cell body with respect to the solid plane, the so called pitch angle θ (see figure 3.12). A cell swimming as a pusher with its head pointing towards the boundary ($\theta < 0$, figure 3.12(a) left) pushes the fluid against the boundary and will experience a counterforce. This counterforce will induce a head up or pitch up rotation pointing away from the surface ($d\theta/dt > 0$). If a pusher

is swimming with its head pointing away from the boundary ($\theta > 0$, figure 3.12(a) right) the same effect will induce an upward rotation acting on the flagellar bundle and a pitch down maneuver of the cell body ($d\theta/dt < 0$). In both cases, the rotation rate tends to align the swimming direction of the cell parallel to the boundary towards a stable orientation angle $\theta = 0°$. This effect can be also explained by considering the interaction with the flow field induced by a mirror image of the cell swimming on the other side of the plane (see [40, 86]). For a cell swimming as a puller, the laterally induced flow pointing away from the cell (see figure 3.10(b)) leads to rotations in the opposite directions ($\theta < 0 \rightarrow d\theta/dt < 0$ and $\theta > 0 \rightarrow d\theta/dt > 0$, see figure 3.12(b)). The cell tends to align itself perpendicular to the surface with its head pointing directly towards or away from the surface $\theta = \pm 90°$. In conclusion, cells swimming as a pusher align their swimming direction parallel to the wall, which is why e.g. swimming *E.coli* [13] and *Caulobacterium crescentus* [91] have both been observed to accumulate near boundaries. Cells swimming as a puller on the other hand tend to align their direction of propagation perpendicular to the surface, they frequently collide with the boundary and do not accumulate at the interface.

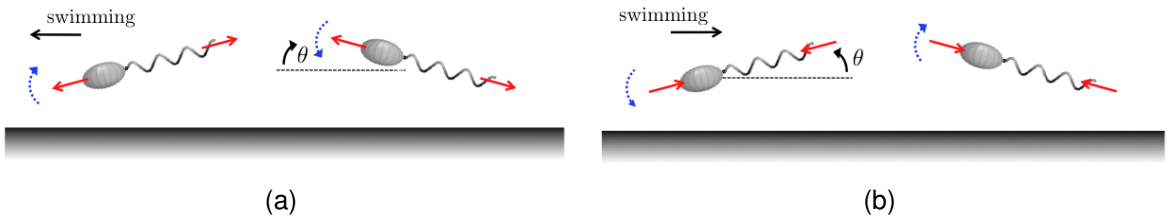

Fig. 3.12: Hydrodynamic surface effect on the orientation of swimming cells with respect to a solid boundary. (a) A cell swimming in the pusher configuration with its head (left) or flagella pointing downward (right) pushes fluid against the boundary. The counterforce induces an upward rotation (left) or downward pitch moment leading the cell to align its swimming direction parallel to the surface. (b) A cell swimming in the puller configuration laterally induces a repulsive flow acting on the boundary (also compare figure 3.10(b)). Swimming near the boundary is unstable because the counterforces acting tend to align the cell perpendicular to the surface. Adapted from [86].

It shall be noted that this third effect on the orientation of the swimming direction is closely linked to the first effect on the swimming speed of the cell. Considering a cell temporarily swimming at an inclined angle with respect to the surface, cell body and flagella have different distances d to the boundary. In the pusher configuration depicted in figure 3.12(a) on the right and in the puller configuration shown in figure 3.12(b) on the right, the flagellar bundle is closer to the boundary. The increase in drag based propulsion power is higher than the increase in the hydrodynamic resistance experi-

enced by the cell body. The cell is expected to move faster than a cell swimming at comparable distance d but parallel to the surface. A cell pushing or pulling with its head closer to the boundary 3.12(a) and (b) left, on the other hand, will experience a comparable higher translational drag which offsets the gain in propulsive power. The cell is expected to move slower.

3.4 Modeling bacterial migration

For the most part the trajectory of a swimming *E. coli* bacterium consists of relatively straight segments, which correspond to periods where the cell is performing a run and propelled by a stable bundle of one or several rotating flagella. The straight segments are interrupted by short events, where the bundle temporarily becomes unstable and the swimming direction changes, periods where the cell is said to perform a tumble (see figure 3.13(a)). In the following we want to present a simple random walk model that captures the basic properties of the swimming motion, its directional autocorrelation function and its effective diffusion constant (mean square displacement). This derivation has first been presented by Lovely and Dahlquist in 1975 [98] and a part of this work is to extend this model to more complex swimming patterns (see section 5.1.2).

We assume that the random walk of the bacterium can be modeled as a sequence of

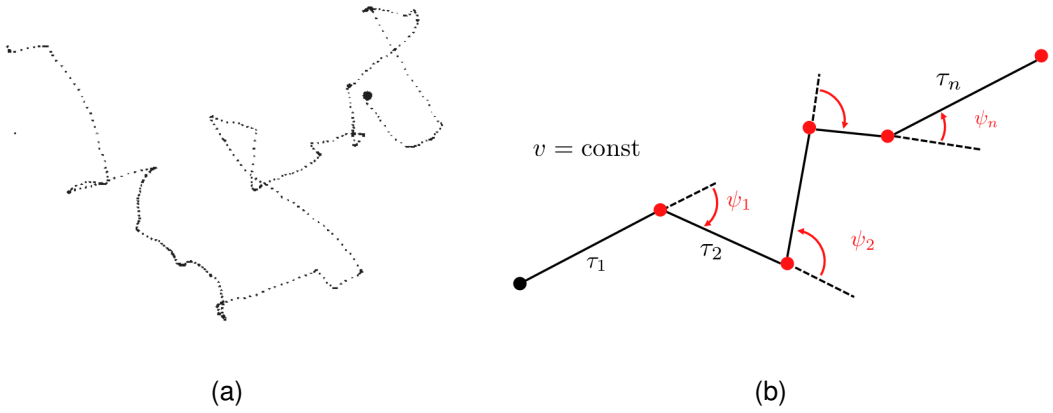

Fig. 3.13: (a) Experimental cell trajectory of swimming *E. coli* recorded in [8] displaying persistent runs (straight segments) and tumbling events where the cell changes direction. (b) Idealized theoretical model of a random walk proposed in [98]. The cell moves at constant speed v performing straight runs with durations τ_n. Runs are interrupted by instantaneous turn events, where the direction changes by the angle ψ_n.

straight segments (runs) with constant speed v interrupted by instantaneous reorientation events where the cell changes its swimming direction by the angle ψ (see figure 3.13(b)). The duration of the reorientation events can be neglected with respect to the duration of the run events and is set to zero. The turning angle ψ, the angle between two subsequent run segments, is random and can be chosen from a given distribution of turning angles for which we introduce the persistence parameter $\alpha = \langle \cos \psi \rangle$. A persistence parameter $\alpha = 1$ would correspond to a cell performing zero degree turns only and the trajectory would form a line made of straight segments with varying lengths. A persistence parameter $\alpha = -1$ would correspond to a cell showing 180° turn events only. The trajectory then consists of a sequence of segments each orientation being anticorrelated with the orientation of the previous segment, corresponding to a cell performing a run-reverse random walk. Most important, we assume that the duration of a run (or the probability for a turning event) is independent of the duration of the previous run. Thus the length of the trajectory segments follow Poisson statistics with an exponential runtime distribution.

The instantaneous velocity of the cell is described by $\boldsymbol{v}(t)$. Following the calculation according to [98, 139] for the velocity autocorrelation function we can then write

$$\langle \boldsymbol{v}(0) \cdot \boldsymbol{v}(t) \rangle = p_0 v^2 + p_1 v^2 \alpha + p_2 v^2 \alpha^2 + ... + p_n v^2 \alpha^n + ..., \tag{3.22}$$

where p_0 is the probability that zero turn events occur in time t and p_n the probability that n turn events occur in time t. We can write this series with α, the mean cosine of the turning angle, because we assume that subsequent turning angles are uncorrelated. From Poisson statistics we know that the probability to have n turn events within time t is

$$p_n = \frac{(\lambda t)^n}{n!} e^{-\lambda t} \tag{3.23}$$

with λ for the turning rate, the inverse of the average run duration $\tau = \lambda^{-1}$. This allows us to calculate the sum in equation 3.22:

$$\langle \boldsymbol{v}(0) \cdot \boldsymbol{v}(t) \rangle = v^2 e^{-\lambda t} \sum_{n=0}^{\infty} \frac{(\lambda t)^n}{n!} \alpha^n = v^2 e^{-\lambda t(1-\alpha)} \tag{3.24}$$

$$= v^2 e^{-t/\tau_c}. \tag{3.25}$$

Here we have defined the correlation time

$$\tau_c = \frac{\tau}{1-\alpha}. \tag{3.26}$$

In reality the run segments of the bacterial trajectory are not completely straight. Because of rotational diffusion, random 'kicks' from the surrounding fluid change the orientation of the cell body's principal axis. Consequently, the cell will randomize its direction of propagation after a given time even if the run is not interrupted by a turn event. To include rotational diffusion in the velocity autocorrelation function we can add a second Poisson process to equation 3.22 with a smaller mean cosine turn rate α_R at a more rapid rate $1/\tau_R$ [98]. This is then reflected by an additional factor e^{-t/τ_R} in equation 3.25, see [139] for further details. The time scale of rotational diffusion is related to the rotational diffusion coefficient via $\tau_R = 1/(2D_R)$ and hence the velocity autocorrelation function now including rotational diffusion becomes

$$\langle \boldsymbol{v}(0) \cdot \boldsymbol{v}(t) \rangle = v^2 e^{-(\lambda(1-\alpha)+2D_R)t}. \tag{3.27}$$

We can calculate the mean square displacement $\langle \boldsymbol{d}(t)^2 \rangle = \langle (\boldsymbol{r}(t) - \boldsymbol{r}(0))^2 \rangle$ by integrating twice over the velocity autocorrelation

$$\langle \boldsymbol{d}(t)^2 \rangle = \int_0^t dt' \int_0^t dt'' \langle \boldsymbol{v}(0) \cdot \boldsymbol{v}(t) \rangle, \tag{3.28}$$

which finally gives the diffusion coefficient for large times in three dimensions

$$D = \lim_{t\to\infty} \frac{\langle \boldsymbol{d}(t)^2 \rangle}{6t} = \frac{v^2}{3(2D_R + \lambda(1-\alpha))}. \tag{3.29}$$

The rotational diffusion coefficient depends on the size and shape of the cell body via the 'Stokes-Einstein relation' on thermal noise

$$D_R = k_B T/\gamma_R \quad \text{with} \quad \gamma_R = (16/3)\pi\eta a b^2 \tag{3.30}$$

with $k_B T$ for the thermal energy and γ_R for the frictional drag coefficient of an ellipsoid rotating about its principal axis, where a and b denote the major and minor axes [6].

The persistence parameter α can be determined for each cell species by experimentally measuring the distribution of turning angles ψ from a sufficient number of trajectories. From equation 3.29, which has evolved from a rather simple model, we can already gain much insight into the spreading dynamics of various cell types:

- The bigger the rotational diffusion the smaller the mean square displacement and thus the slower the spreading over time of a cell population in a fluid environment. A population of smaller cells has a higher D_R than bigger cells and will spread slower. Comparing two cell types of the same size (surface area of the cell body), a cell with a spherical head is less sensitive to angular changes than a prolate ellipsoid with an aspect ratio $a/b > 1$. Cells with a more elongated body will have a higher D_R and thus a smaller D and spread slower. It is important to note, that cells might be more prone to angular changes, with a higher D_R calculated from experimental data as compared to equation 3.4, also because of their intrinsic propulsion mechanism. An asymmetric distribution of flagella over the cell body or a helical filament whose axis is not aligned with the principal axis of the cell body might lead to a constant 'wobbling' of the cell body and an increase in the observed rotational diffusion coefficient.

- Depending on the swimming pattern of the bacterium, the mean square displacement will change significantly. If all turning angles ψ are completely random, $\alpha = 0$, we have $D = v^2/(6D_R + 3\lambda)$. In the case of a bacterium that is constantly reversing its swimming direction by $\psi = 180°$, we get $D = v^2/(6D_R + 6\lambda)$. The translational diffusion reduces by a factor of 50% as compared to a cell performing random turn between 0° and 180°. Furthermore, e.g. in the presence of a chemotactic stimulus, bacteria can change their turning frequency λ by reducing the switching rate of the motor leading to larger τ. This can be used by cell populations to shorten the time needed to explore the environment or bias their motion towards a food source.

For *E. coli* swimming in a uniform environment, Berg [6] has calculated a rotational diffusion constant $D_R \approx 0.062$ rad^2 s^{-1} and measured a tumbling frequency $\lambda \approx 1$ s^{-1}, an average turning angle around $70°$, and a persistence parameter $\alpha \approx 0.33$ [8]. With an average swimming speed of $v \approx 22$ μm/s [21] we can estimate the diffusion coefficient according to equation 3.29 to

$$D_{E.coli} \approx 203 \ \mu\text{m}^2/\text{s}.$$

Analyzing cell trajectories of *E. coli* AW405 (wild type strain) under varying environmental conditions, experimental studies have reported values for $D_{E.coli}$ ranging from 160 to 380 μm^2/s [10, 90, 153] and are thus in good agreement with this random walk theory for the mean square displacement of a run-tumble bacterium.

Chapter 4

Materials and Methods

4.1 Cell culture

Pseudomonas putida KT 2240 cells from frozen stock were grown to stationary density in an overnight shaking culture of Lysogeny broth medium (Applichem (Darmstadt, Germany), LB-Medium Lennox, 10 g/L Tryptone, 5 g/L NaCl, Yeast Extract 5 g/L, adjusted to pH=7.0). Approximately 50 μL of the dense cell suspension were dispersed on a solid agar dish (LB-Medium, 1.5% Agar-Agar) and the dish was incubated for 24 hours at $30°$C (see figure 4.1). With a sterile inoculating loop, a single colony from the confluent cell layer was picked and streaked onto a new LB-Dish, which was then again incubated for another 24 hours to achieve a pure culture. Colonized LB-Dishes were stored at $4°$C and used as cell source for three weeks after which they were constantly renewed. Within this period of three weeks, growth curves of shaking cultures inoculated from the dishes showed no significant variations (section 4.2).

Before an experiment, a 50 mL flask with N-Medium (5 g/L Peptone, 3 g/L Meat extract, adjusted to pH=7.0) was inoculated by a single loop pick from the stationary LB-dish and the suspension was grown overnight on a shaker at $30°$ C rotating with 300 rpm. Depending on the height of the microfluidic chamber used in the experiment, cells from the stationary shaking culture were diluted in N-Medium to an optical density of 0.05, 0.01, or 0.005 and filled into the microchannels with a height of 10, 50 or 300 μm. This corresponded to an average cell number densities around $\approx 10^7$ cells/mL (see section 4.4 for the individual experimental procedures).

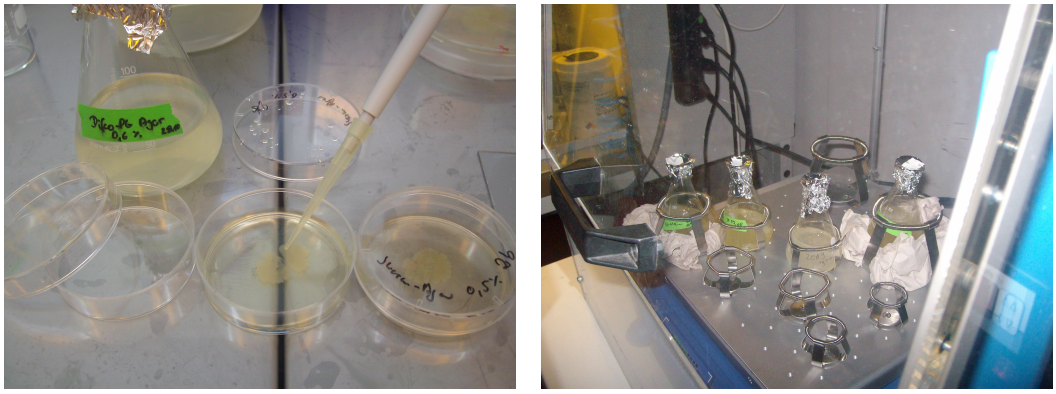

(a) (b)

Fig. 4.1: Cell Culture: (a) Inocculation of source dishes with stationary cell suspension from an overnight shaking culture grown from frozen stock. (b) Bacterial cell suspension growing on shaker inside $30°$C incubation chamber.

4.2 Cell growth in shaking culture

To perform experiments at comparable conditions we determined the growth curve of *P. putida KT 2240* from source dishes of different age in the shaking culture of N-medium. This was done following standard procedures for measuring bacterial growth [158]. First, we measured the optical density, i.e. the adsorption of light of wavelength 600 nm (OD600) with a Photometer (Eppendorf BioPhotometer (Hamburg, Germany)), in cell suspension samples taken at consecutive times from the shaking culture. As the cell density in the sample increases, the optical density of the suspension and thus the adsorption increases. Second, to relate the change in optical density to the cell density in the sample, a calibration curve was recorded and the range of measurement values where the optical density is linearly proportional to the cell density was determined.

The results are shown in figure 4.2 for growth in cultures which were inocculated from LB-dishes with storage times ranging from one day till 30 days. In general, the cell density as a function of time shows the typical pattern of bacterial growth [106]. After a lag phase with slow growth, which is usually attributed to cells adapting to the specific environment [106, 128], bacteria reach the exponential phase where cells divide at a constant rate and the growth rate is maximum. After four to six hours, growth limiting factors take effect. The medium gets depleted and the division rate decreases. We observe the beginning of the stationary phase. Generally our results indicate that with increasing age of the inocculation sample, the lag time till the onset of exponential growth increases from approximately two hours (one day old dish) up to four hours (30 days of

storage time). The growth curve recorded after 19 days of storage time (purple-violet markers in figure 4.2) with a lag time comparable to cells from fresh dishes, however, deviates from this trend. We suggest that the duration of the lag phase also depends on the initial inocculation number of cells and that this number can vary from experiment to experiment due to the amount of cells picked by the inocculation loop. Growth during the exponential phase however is only slightly affected by cell age. We determined the fastest growth rate, retrieved from an exponential fit, to $\lambda = 0.915$ h^{-1} for fresh cells (one day old dish) and the slowest to $\lambda = 0.643$ h^{-1} (after 30 days of storage time).

Dishes were constantly renewed every three weeks (21 days). From the available four datasets of 1, 2, 9 and 16 day old cells we calculated an average growth rate of $\bar{\lambda} = (0.816 \pm 0.196)$ h^{-1} corresponding to an average doubling time of $\bar{T}_\lambda \approx 51$ minutes, and an average duration of the lag phase of $T \approx 2.75$ hours.

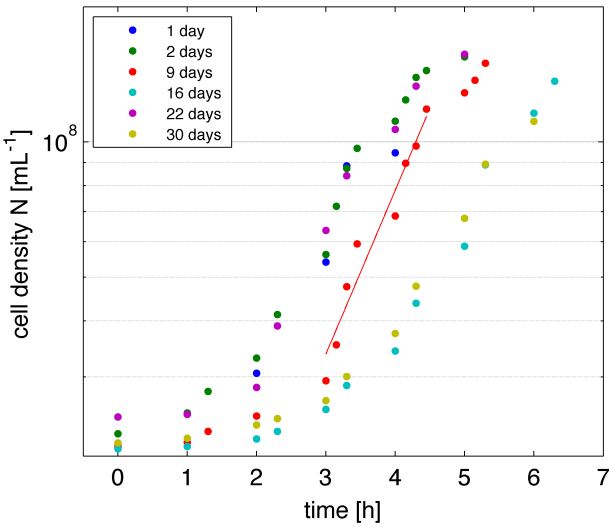

Fig. 4.2: Cell density as a function of time for cells growing in a shaking culture with N-Medium. The cells were loop-pick inocculated from agar dishes of different age, ranging from 1 day to 30 days. With increasing age the lag time, before cell growth enters the exponential phase, increases from 2 hours (one day old) till 4 hours (30 days old). The red line shows an exponential fit with $\lambda = 0.849$ h^{-1}, corresponding to a doubling time of $T_\lambda \approx 50$ minutes.

4.3 Microfluidics

To perform time lapse recordings of swimming and surface attached bacteria at a liquid-solid interface in confined geometries we decided to use microfluidic channels made

from polydimethylsiloxane (PDMS) using soft lithography [43, 160].

The resulting channels with varying geometries are filled with the cell suspension and consist of an optically transparent polymer block, which is sealed from below by a glass coverslip. Via tubings, attached to syringes and infusion pumps, we can connect to the channel inlets and expose cells to a defined shear by running a constant flow, add chemicals or renew growth medium. Furthermore, the PDMS channel is permeable to oxygen and thus suited for experiments with aerobic microorganisms, while at the same time it prevents uncontrolled fluid flow advection or evaporation of fluids that would occur in comparable experiments on a dish or a glass coverslip. Microfluidic channels thus served as hydrodynamically stable platform to investigate bacterial movement near and surface related growth at a glass-liquid or PDMS-liquid interface.

4.3.1 Fabrication

The Manufacturing of all microfluidic devices followed customized protocolls for rapid prototyping and soft lithography [43, 160]. First, the channel layout was designed on a personal computer using Novarm DipTrace, a CAD freeware, that could export GERBER-files, a format still used to control plotters of most mask manufacturers. Depending on the necessary resolution, an emulsion film mask with the smallest feature in our channel structure going down to ten microns or a solid sodalime glass-chrome mask that could contain features down to one micron in size, was ordered from JD Photo-Tools (Oldham, United Kingdom) or from MLC corporation (Jena, Germany).

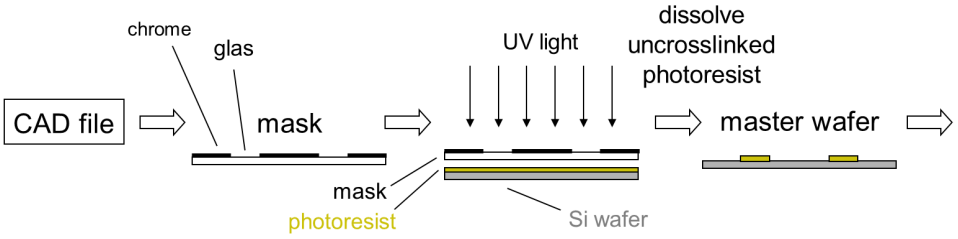

Fig. 4.3: Steps of microfabrication I: the channel layout from the CAD-file is etched or printed on a sodalimeglass-chrome or emulsion film mask and then transferred to a negative master on a silicon wafer using contact photolithography. See text for closer description.

We then used 1:1 contact photolithography with SU-8 2000 series photoresists (Microresist (Berlin, Germany)) to generate a negative master of our mask layout on a Silicon-Wafer (figure 4.3). First, the Si-Wafer was rinsed with aceton, isopropanol and destilled water, dried with N_2 and clean baked on a hot plate (Electronic Micro Systems

Model 1000-1 (Salisbury, United Kingdom)) at $200°$C. If done thoroughly, no further surface treatment (e.g. with a contact promoting agent) was necessary. The clean wafer, measuring 105 mm in diameter, was cooled down to room temperature and $3-6$ mL of photoresist were dispensed in the middle of the wafer forming a single, viscous droplet. Depending on the desired height of the structures on the negative master, photoresists with different viscosities were used (table 4.1).

height [μm]	Photoresist	Spincoating Step 1	Spincoating Step2
100	SU8-2150	15 s at 500 rpm	40 s at 3500 rpm
30	SU8-2050	15 s at 500 rpm	45 s at 3600 rpm
10	SU8-2010	20 s at 500 rpm	45 s at 3500 rpm

Table 4.1: Microfabrication I: Spin coating program and type of photoresist used for negative master wafers of varying height. Acceleration in spin coating rotation was 110 rpm/s in step 1 and 330 rpm/s in step 2.

To disperse the photoresist, the wafer then was put on a spin coater (Laurell Technologies WS-400BX-GNPP/LITE (North Wales, USA)), programmed to undergo two subsequent rotation stages with defined acceleration and terminal rotation velocities to create a uniform layer of photoresist with the desired height (see table 4.1 for settings).

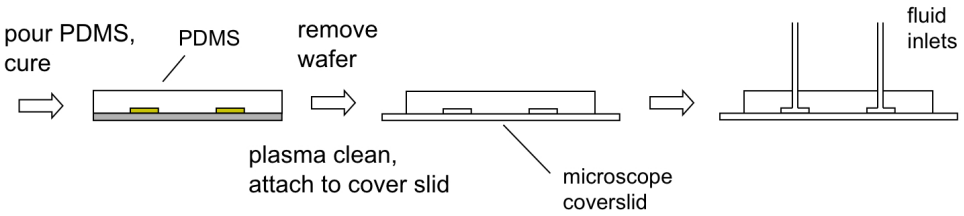

Fig. 4.4: Steps of microfabrication II: Softlithography- a positive replica of the negative master wafer is produced by pouring PDMS on the wafer and adding a curing agent. The channel is then cut out from the wafer. After plasma cleaning the microchannel forms a stable bond with a glass coverslip. Before the experiment, holes for fluid and cell inlets are punched by a needle. See text for closer description.

After the resist was applied to the substrate, the wafer was given 10 minutes to relax and then put back on the hotplate to evaporate parts of the solvent and smoothen the photoresist layer, a process called Softbake. This was done in two temparature steps, the thinner the resist, the shorter the necessary Softbake time (see table 4.2). To transfer the pattern, the mask was brought in direct contact with the wafer and illuminated with UV-light (Tamarack Scientific PRX 2000-20 (Corona, USA)) for a defined exposure

time (see table 4.2). The exposed parts on the wafer become crosslinked and insoluble to developer solution (negative photoresist). During the following postbake on the hot plate, crosslinking is finalized and the uncrosslinked parts of the photoresist are removed by putting the wafer two times for approximately 30 till 60 seconds in a bath of developer (Microresist MR-Dev 600 (Berlin, Germany)). The master wafer is created.

The various microchannels themselves were produced by molding liquid PDMS together with 10% of curing agent (Sylgard 184, Dow Corning Corp. (Midland,USA)) against the master wafer (figure 4.4). After 60 min in a vacuum desiccator, air bubbles from the molding process are removed and the mixture is heated up to $75°$C for 45 min during which the crosslinkers from the curing agent connect the free polymer chains inside of the solution and the mixture solidifies. Approximately one hour before each experiment, the devices are cut out using a scalpell and holes for fluid inlets are punched with sharpened 20 gauge shringe tips (VWR (Darmstadt, Germany)). Together with a 40 mm x 24 mm glass coverslip the PDMS block was put for 3.5 min into a plasma cleaner (Harrick Plasma PDC-002 (Ithaca, USA)). During the plama cleaning, the valve was slightly opened every 30 seconds adjusting the vacuum pressure inside to ensure that the purple plasma visible through the bull eye of the apparatus was kept stable.

height [μm]	Softbake	Exp [mJ/cm^2]	Postbake
100	$65°/95°$C for $10/20$ min	285	$65°/95°/65°$ for $10/20/10$ min
30	$65°/95°$C for $10/10$ min	250	$65°/95°/65°$ for $10/10/10$ min
10	$65°/95°$C for $10/\ 5$ min	120	$65°/95°/65°$ for $10/10/10$ min

Table 4.2: Microfabrication II: Softbake, exposure dose by UV-lamp (Exp) and postbake conditions for manufacturing waferstrucures of varying height.

The air plasma oxidizes the surface of the PDMS block and the glass coverslip, etching hydrocarbons and leaving Si-OH groups on the surface [23,70,107]. After the cleaning, when placed in contact with each other, Si-OH-Si bonds form at the interface and the channel is sealed tightly. The plasma cleaning produces an important side effect. Due to the clean surface, covered with SiOH-groups, the channel becomes hydophilic and can be wetted by polar liquids much easier [14]. Since the device becomes hydrophobic again after approximately half an hour, the channel is filled immediately with the desired chemicals or diluted cell suspensions. Our microfluidic device is ready for use.

Fig. 4.5: Preparation of a microfluidic experiment: a channel made from PDMS has been cut out using a scalpel. This corresponds to the transition from step one to step two in figure 4.4. The PDMS block is a negative replica of the structure printed on the wafer. After punching holes for the fluid inlets, plasma cleaning and sealing with a coverslip, the microchannel is ready for use.

4.3.2 Devices used in experiment

In the following we present an overview on the different microfluidic devices used in this work which are depicted in figure 4.6. Two-dimensional trajectories of cells swimming in the bulk fluid were recorded in an IBIDI μ-Slide VI$^{0.4}$ (Ibidi GmbH (Martinsried, Germany)), a linear channel with a glass bottom measuring 17 mm in length, 1 mm in width and 0.4 mm in height (see figure 4.6(a)). The results from these experiments are presented in section 5.1.1. Tracking of cells in two- and three-dimensions at various distances to a single boundary and in a confinement between two boundaries was performed in a linear microchannel (see figure 4.6(b)) manufactured according to the protocol described in the previous section. The channels had a length of 30 mm, a width of 0.5 mm and, depending on the experiment, a height of 10, 20 or 100 μm. The results from these experiments are presented in section 5.2. Apart from the linear microchannel, in the surface related growth experiments for which we present the results in section 5.3, an additional microchannel with a Y-shaped geometry (see figure 4.6(b)) was designed, again produced according the procedures of microfabrication in section 4.3.1. The three branches of the channel measure 0.5 mm in width and 20 μm in height.

In all experiments with linear microchannels, cell were recorded in the center, a minimum of 10 mm away from the channel inlets (red box in figure 4.6(a) and (b)). In the Y-shaped channel, the particular aim was to image two subpopulation of cells subjected to two different flow media. Cell growth was therefore recorded at the crossection of the

two channel branches (red box in figure 4.6(c)).

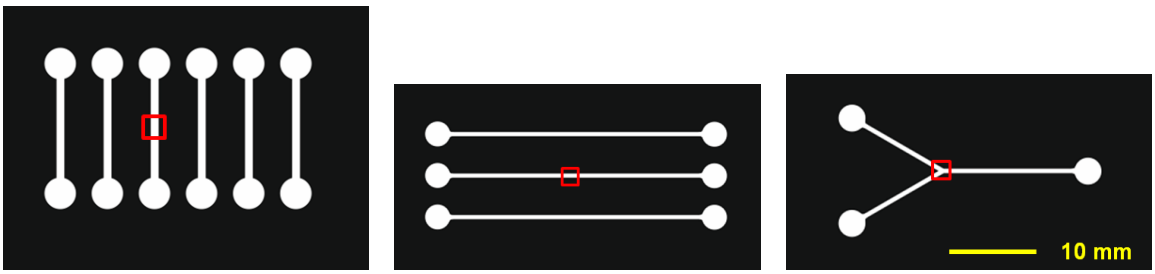

(a) (b) (c)

Fig. 4.6: Overview on different microfluidic channels used in this work: (a) IBIDI μ-Slide VI$^{0.4}$ flow chamber. (b) linear microchannel of varying height produced by Soft-Lithography (c) microchannel with Y-shaped geometry. The red box marks the region of interest where cell motility and surface-related growth was recorded. See text for closer description.

4.4 Experimental setup

4.4.1 Colony growth and swimming in linear microchannels

The linear microchannel filled with the cell suspension was mounted on the stage of an inverted microscope (Olympus IX-71 (Tokyo, Japan)), equipped with a Mikrotron EoSens MC 1362/63 highspeed B/W camera (Munich, Germany) (see figure 4.7). During the first 30 minutes after cell filling, in our region of interests (ROI) in the middle of the microchannel, approximately 15 mm away from each cell inlet, an initial population ranging from 10 to 30 single, isolated cells settled at the surface of the glass coverslip. At the beginning of the experiment, no more than three to five swimming cells could be observed. To provide stable no flow conditions, each channel inlet was sealed by tubings (PTFE 0.5 x 1.07 mm, Novodirect GmbH (Kehl, Germany)) filled with N-Medium.

To monitor surface related colony growth as well as the dynamics of the cells swimming in the bulk fluid and in the vicinity of the surface with sufficient contrast, we recorded phase contrast images with an Olympus 20X UPLFLN-PH objective. Unless stated otherwise, a one minute snapshot-sequence with 50 frames per second (fps) was recorded every 30 minutes for the first 8 hours of the experiment, starting with the cell filling. To track the motion of swimming cells, data was taken from the snapshot sequences recorded $5:30$ hours after the beginning of the experiment when the channels were populated by a sufficient number of swimmers. At this point we

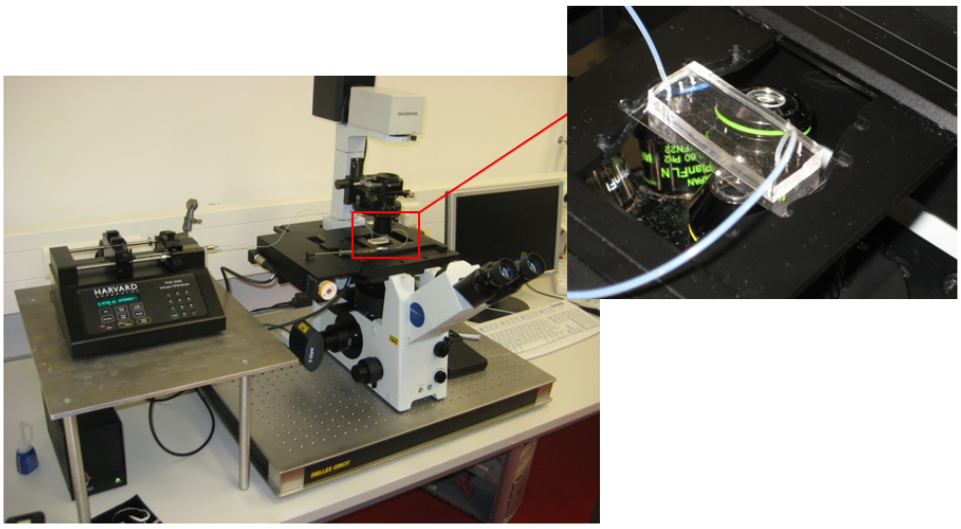

Fig. 4.7: Experimetal setup for linear channel time lapse microscopy: The microchannel is mounted on the stage of an inverted microscope. To prevent evaporization and maintain stable pressure conditions, two tubings filled with N-Medium are connected to the channel inlets. High speed sequences at 50 fps are recorded every 30 minutes to monitor both attachment and growth and fast cell swimming within the channel.

counted approximately 100 cells per mm^2. The distance between neighboring cells was about 100 μm, which was two orders of magnitude larger than the average cell size (4.65 ± 0.23 μm by 1.93 ± 0.04 μm, major and minor axes from an ellipsoid fit). Therefore we could assume that hydrodynamic interactions *between the cells* did not affect the swimming trajectories. The 1280 x 1024 px 8 bit images were stored on a solid state disk and transferred to a Windows 7 personal computer with Intel Core i7- 3.80 GHz and 32 RAM fur further processing. Experiments in the linear channel were performed with three different channel heights (10, 20, 100) and in the IBIDI μ-Slide VI$^{0.4}$ with a height of 300 μm.

4.4.2 Three-dimensional swimming in linear microchannels

Apart from the two-dimensional projection, we wanted to aquire the full three dimensional picture of swimming activity in the bulk fluid and at distinct distances from the surface. Recent attemps used Digital Online Holography (DIH) [156] or the evaluation of defocused particle images in dark field microscopy [159] to aquire 3D-cell trajectories. While the former method is difficult to combine with the use of microfluidics, where impurities in the PDMS lead to irregular obstructions hindering the digital reconstruc-

tion of holographic images, the latter requires delicate calibration and both methods are problematic at high cell densities in the ROI. With a powerfull high speed camera at hand, we instead decided to use fast Z-Scans and 3D-reconstrunction (see figure 4.8).

For this purpose, an objective in the microscope turret was attached to a piezoelectric motor (Hochdynamisches PIFOC® Piezo Nanofokussystem P-726.1CD, Physik Intrumente GmbH (Karlsruhe, Germany)). After $5:30$ hours of development led to a sufficient number of swimming cells in the microchannel, the camera was synchronously started at 480 fps together with the piezo motor that drove the objective, oscillating the focal plane at 12 Hz with a total displacement of 10 μm. This corresponded to a step size or distance between the focal planes of two subsequently recorded images of 0.5 μm. To acquire accurate positions in z-dimension we used high magnifiaction objectives with a low focal depth, either a 60X UPLFLN-OIPH or 100X UPLFLNO2PH Olympus.

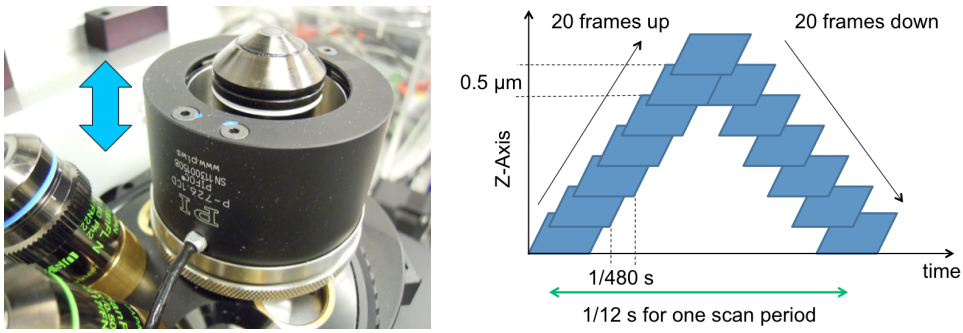

(a) (b)

Fig. 4.8: Z-Scanning to acquire three-dimensional cell trajectories: (a) a piezo motor drives the microscope objective, oscillating at 12 Hz. (b) Synchronized with the motor, a frame is taken every 2.1 ms at a different focal position. The motion of bacteria can be followed in three dimensions with a time resolution of $\Delta t = 0.08$ s and a sample depth of 10 microns.

4.5 Image Processing and cell tracking

4.5.1 Tracking sessile and swimming cells in two dimensions

To binarize the images and extract information about a cells position, perimeter and orientation in the microchannel a customized algorithm using MATLAB 8.0 R2012b (MathWorks (Natick, USA)) together with the Image Processing Toolbox was written. After

successfull segmentation, the cell positions determined for each frame were linked together by a tracking algorithm to form trajectories in time.

First, a bandpass filter was applied to the original images to correct for high frequency noise at the CMOS-sensor of the camera and for spatial modulations (e.g. uneven illumination) at frequencies lower than the average cell size. To perform the bandpass filtering we used an open source MATLAB function, described in detail in [32]. Filtering is achieved by calculating the difference between two filtered versions of the original image. The first filtered image, a low frequency noise reduced version, is retrieved by 'smoothing' the original image with a boxcar average over a region λ_l larger than the average cell radius . The second filtered image is a high frequency noise reduced version retrieved by convolving the original image with a two-dimensional Gaussian function with half-width λ_s. The parameters $\lambda_l = 6$ pixel and $\lambda_s = 0.5$ pixel yielded best results. In figure 4.9(a) and (b) we provide a sample image and the corresponding intensity profile along a horizontal line (black curve) crossing a swimming cell and a cell colony on the surface. After bandpass filtering (figure 4.9(c) and (d)) the intensity profile is adjusted for short range fluctuations (blue line). Cells can be identified as dark gray values on a smooth gray background. The filtered images were then converted into binary images using isodata thresholding [127]. From the binary image sequence, a background image was constructed by calculating the average intensity over time for each image pixel. The resulting background image was subtracted from the sequence to exclude non moving cells. After a second isodata thresholding and a 3x3 binary median filter was applied, the binarized images accurately captured the contour of all swimming cells in the system.

We illustrate the results of the segmentation algorithm in figure 4.10. The original image is depicted in figure 4.10(a). After background subtraction and the segmentation process described above, we successfully identified the contours of the swimming cells, highlighted in red, and the shape of the sessile colonies on the surface, highlighted in green, see figure 4.10(b). The position of the swimming cells and colonies are indicated by a red and green dot respectively as shown in figure 4.10(c).

The position of each cell in each given image was determined by calculating the centroid (center of mass) of the corresponding pixel ensemble in the binary image. We then used a MATLAB version of the cell tracking algorithm written by Crocker and Grier [32] to link these positions together to form trajectories in time and space. Essentially, the algorithm had to find the most probable set of N links between N cell positions found in two consecutive images. Proper linking was then achieved by minimizing the cost function

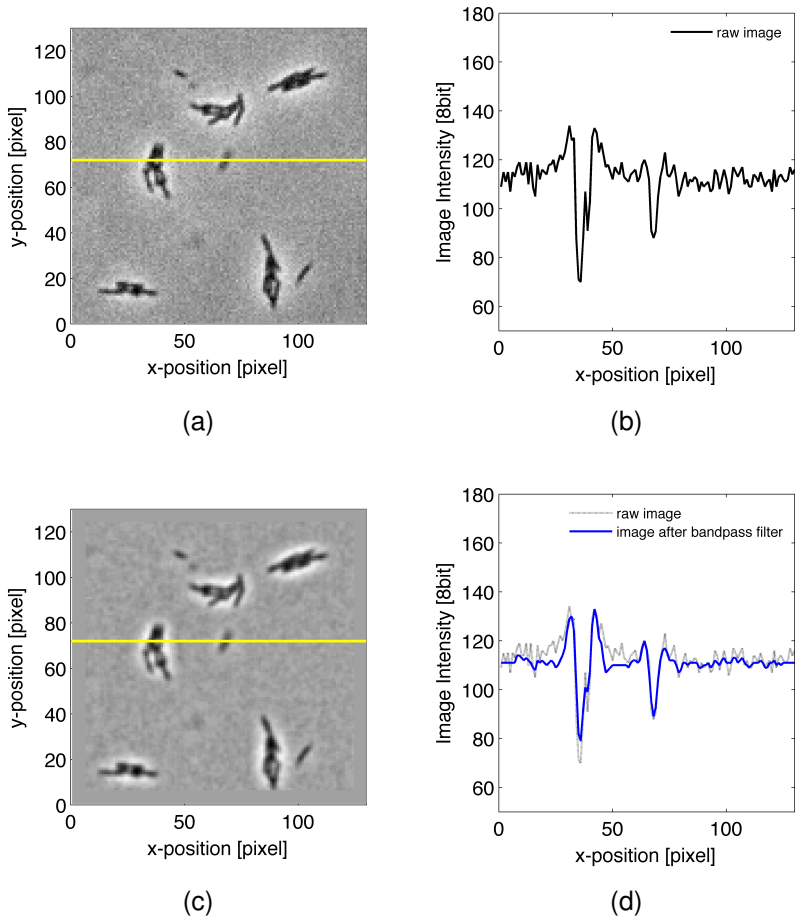

Fig. 4.9: Overview Bandpass Filtering: (a) Raw image and horizontal line in yellow crossing an individual swimming cell and a colony of cells on the surface. (b) Intensity profile (black curve) along the horizontal line in (a). (c) Raw image after bandpass filtering to correct for low and high frequency noise (see description in the text). (d) The line profile is cleared from short range fluctuations. Cells can be identified as dark gray values on a smooth background.

$$\Upsilon = \sum_{i=1}^{N} \delta_i^2, \tag{4.1}$$

the sum over the square displacement δ_i^2 of all 'bonds' between all pairs of cell positions in two consecutive frames for a given assignment (a given set of bonds). The tracking algorithm calculates Υ for all possible combinations of bonds ($N!$ in total) and chooses the assignment that minimizes this cost function. To reduce the computational effort which goes like $\sim N!$, with the number of cells during our experiments sometimes exceeding $N > 1000$, a cutoff length L_c was introduced to reduce complexity of the linking

process. Consequently, the process of minimizing the cost function for the hole network of $N!$ possible assignments is broken down to solving Υ for a number of subnetworks formed by groups of cell positions no further than a distance L_c away from each other. With L_c small enough, the linking process becomes trivial because most subnetworks contain only a single bond [32].

In general the algorithm produced good results if the average displacement δ of the cells between two subsequent frames was sufficiently smaller than the typical distance between them. With the cells on average swimming at a velocity $v \approx 40\ \mu$m$/s$ and a time between two subsequent frames $\Delta t = 0.02$ s, we decided for a cutoff parameter $L = 2\ \mu$m. Consequently, trajectory linking leading to velocities bigger than $100\ \mu$m$/s$ were thus considered unrealistic and excluded from the tracking process.

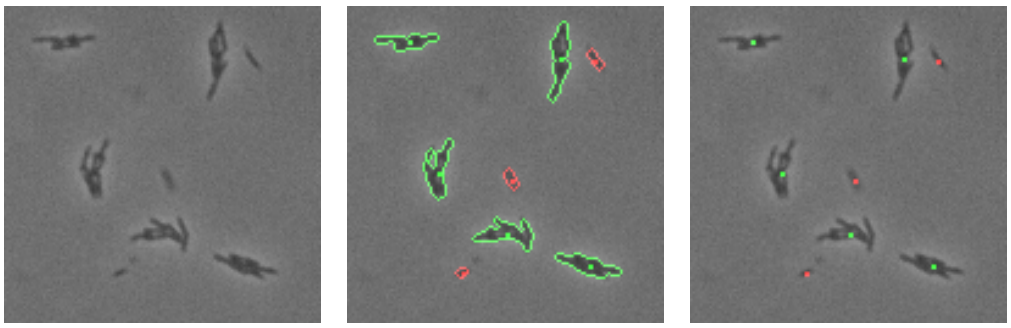

(a) (b) (c)

Fig. 4.10: Illustration of the segmentation result: (a) original image showing individual swimming cells and sessile colonies on the surface. (b) and (c) Cell contour lines and centroid positions (dot) for swimming cells (red) and colonies (green) after image segmentation. The algorithm successfully captures position and shape of cells and cell colonies.

4.5.2 Determining swimming height from two-dimensional trajectories

For cells swimming in a confined environment or near a wall, apart from the three-dimensional trajectories, we also wanted to acquire a rough information from the two-dimensional trajectories on the third dimension, the distance from the cell to the solid boundary. In every two-dimensional image sequence (section 4.4.1), recorded at a distance d from the boundary, over time cells swam in and out of the objective's focal plane. The higher the objective's depth of sharpness f, the longer we could track a single cell swimming perpendicular to the focal plane or track the motion of a swarm

of cells swimming parallel to the surface but at various distances from it. While our algorithm still detected the shape of a cell swimming slightly above or below the focal plane, the sharpness of the cell object was reduced (see figure 4.11, left column). We measured this by using standard Sobel edge detection [55]

$$I_E = \sqrt{(I \star M_1)^2 + (I \star M_2)^2}. \tag{4.2}$$

Here I is the original cell image, while $\star$ denotes a convolution with the masks

$$M_1 = \begin{bmatrix} -1 & 0 & 1 \\ -2 & 0 & 2 \\ -1 & 0 & 1 \end{bmatrix} \text{ and } M_2 = \begin{bmatrix} -1 & -2 & -1 \\ 0 & 0 & 0 \\ 1 & 2 & 1 \end{bmatrix}. \tag{4.3}$$

For each cell we then calculated a value $\overline{I}_{E,cell}$, which was the mean over all pixel intensities from I_E falling within the boundary of the corresponding cell that was determined by the segmentation algorithm. A high value $\overline{I}_{E,cell}$ means that the cell is swimming in the center of the focal plane, whereas low values from blurry cell contours correspond to cells moving above or below the focal plane.

In each experiment, we recorded a sessile reference cell in focus at the glass bottom of the microchannel and with the focal plane at various distances from the bottom. The distance was given by the scale on the finetuning knob of the mircoscope. The average edge intensity $\overline{I}_{E,cell}$ is then calculated for each distance from the focal plane. With the resulting calibration curve we could convert the edge intensity information into height information on swimming cells in the corresponding experiment (figure 4.12). Measuring the sharpness of a cell's contrast with the objective focused at the glass bottom of the microchannel allowed us to determine a cells z-position within a distance $d = 0 - 8$ μm ($f = 8$ μm) in the vicinity of the focal plane with an accuracy of ± 1 μm.

4.5.3 Tracking swimming cells in three dimensions

To extract three dimensional information on the position of the cells from the captured Z-Scanning images, a series of customized MATLAB programs was written. Here we made extensive use of the variety of functions implemented in the MATLAB Image Processing Toolbox. For every second of time-lapse microscopy, 12 image stacks corresponding to different times and each of them consisting of 20 images corresponding to different focal planes were available. First, an average intensity image over time

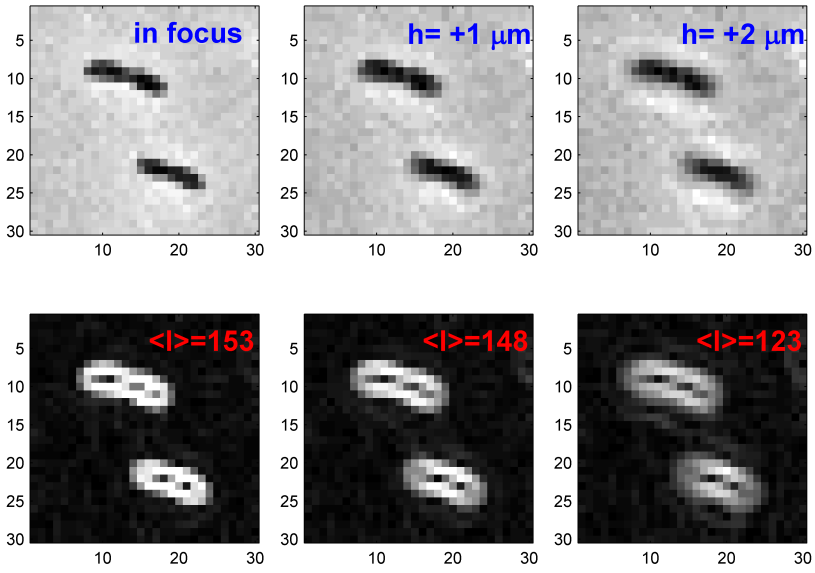

Fig. 4.11: Upper row: raw images of a cell at rest taken at different distances d to the focal plane where it is in focus. With increasing distance cell images become blurred. Lower row: processed images after Sobel-edge detection. The average value $\overline{I}_{E,cell}$ measuring the cell body sharpness decreases for the blurred images of cells. Edge intensity can be converted into information about the z-position of the cell.

was calculated for each focal plane yielding 20 'background' images. We then subtracted from every original image its corresponding 'background' image to eliminate non-moving objects and restrict our analysis to swimming cells. Subsequently, a max-entropy thresholding procedure [73] was separately applied to binarize each image. Remaining high frequency noise from fluctuating illumination was reduced using a 3 x 3 median filter. The segmented images of swimmers in all focal planes corresponding to the same time step were then combined together to form 1280 x 1024 x 20 matrices allowing for three-dimensional reconstruction of each cell body. By calculating the center of mass from each connected object in the matrices, the three dimensional position of each cell could be determined. Positions were then linked together to form three-dimensional trajectories in time with the same next-neighbor tracking algorithm used on the two-dimensional data ([32], see section 4.5.1), this time minimizing the three-dimensional instead of the two-dimensional displacement over all possible position links (see equation 4.5.1).

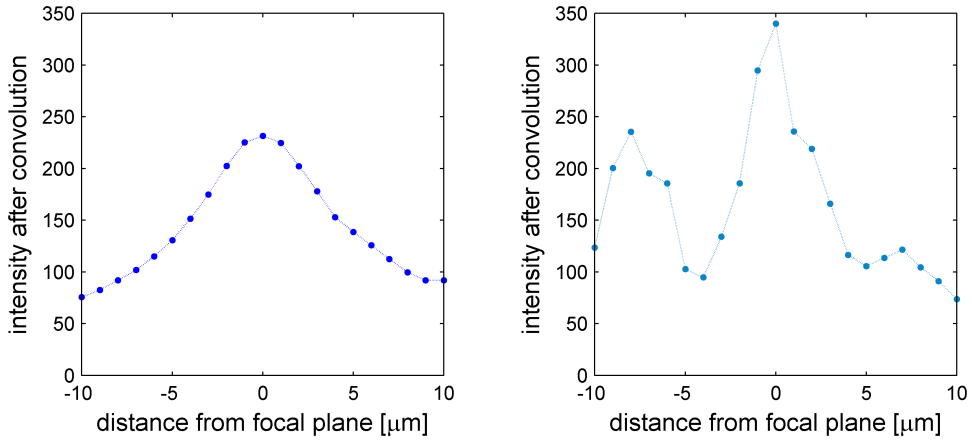

(a) (b)

Fig. 4.12: Average sharpness of a cells image, $\overline{I}_{E,cell}$, as a function of the distance from the focal plane for two different objectives in phase contrast mode. (a) 20xUPLFLN Olympus: cells are tracked at a maximum distance of ± 8 μm from the focal plane. Within this region, differences in swimming height can be evaluated. (b) 40xLUCPLFLN Olympus: cells are tracked at a maximum distance of ± 3 μm from the focal plane. The second peak peak in sharpness, 8 μm below the focal plane, is due to the halo effect, an artifact which occurs in phase contrast images. Because of this, for intensity values below 200 we can no longer distinguish between cells at ± 2 vs $\pm 8 \mu$m. Differences in swimming height are only evaluated at distances up to ± 2 μm from the focal plane.

4.6 Analysis of cell trajectories

4.6.1 Statistics from two-dimensional trajectories

In two-dimensional tracking experiments, a cell trajectory is represented by the two-dimensional position vector $\mathbf{r}(t)$ of the cell center projected onto the xy-plane at each frame t. Depending on the experimental conditions (cell density in the microchannel, quality of recorded images) the length of the trajectories vary from ten till more then four hundred frames. With our time resolution of one frame taken every $\Delta t = 0.02$ s (50 fps), this means that the length of cell trajectories ranges from 0.2 to 16 s. Unless stated otherwise, only trajectories longer than two seconds were used in the data analysis.

Speed and directionality of cell movement are evaluated based on the instantaneous velocity of the cell (figure 4.13(b)), which is calculated as

$$\boldsymbol{v}(t) = \frac{d\mathbf{r}}{dt} = \frac{\mathbf{r}(t) - \mathbf{r}(t - \Delta\tau)}{\Delta\tau}. \tag{4.4}$$

The acceleration or deceleration of the cell is determined by the instantaneous change in the velocity between two time steps:

$$\mathbf{a}(t) = \frac{d\boldsymbol{v}}{dt} = \frac{\boldsymbol{v}(t) - \boldsymbol{v}(t - \Delta\tau)}{\Delta\tau} \tag{4.5}$$

As calculated here, the instantaneous velocity represents the average displacement of a cell within a chosen time interval $\Delta\tau$= $n\Delta t$, which can be a multiple of the time between two recorded frames Δt in our experiment. For a bigger $\Delta\tau$ more information is lost about the erratic cell trajectory and the stochastic component of bacterial motility (figure 4.13(b) and figure 4.13(c)). For smaller $\Delta\tau$ on the other hand, measurement noise from image processing can lead to sudden jumps in the cell centroid position and the calculated averages become unreliable.

By evaluating parameter changes in the segmentation algorithm and the fluctuations in the centroid position of an immobile cell across subsequent frames we estimated an error ξ of 0.1 μm on the position of the cell which leads to a measured swimming speed of

$$|\boldsymbol{v}'(t)| = \frac{|\mathbf{r}(t) - \mathbf{r}(t - \Delta\tau)|}{\Delta\tau} \pm \frac{2\xi}{\Delta\tau}.$$

The timelag $\Delta\tau$ was then chosen such that the contribution from the displacement of the cell center due to measurement error is much smaller than the expected average swimming speed of the cell:

$$\left(\frac{2\xi}{\Delta\tau}\right) \ll \left\langle \frac{|\mathbf{r}(t) - \mathbf{r}(t - \Delta\tau)|}{\Delta\tau} \right\rangle \approx 30 \ \mu\text{m}/s$$

Unless stated otherwise, motility data was always calculated from a time interval $\Delta\tau = 0.08$ s ($n = 4$). Additionally, to remove non-moving or dead cells from motility statistics, all trajectories of cells swimming with an average speed below 10 μm/s were excluded.

Displacement and Propagation Angle

The displacement is calculated with respect to the starting point of each individual cell trajectory (figure 4.13(d)).

$$\boldsymbol{d}(t) = \boldsymbol{r}(t) - \boldsymbol{r}(0). \tag{4.6}$$

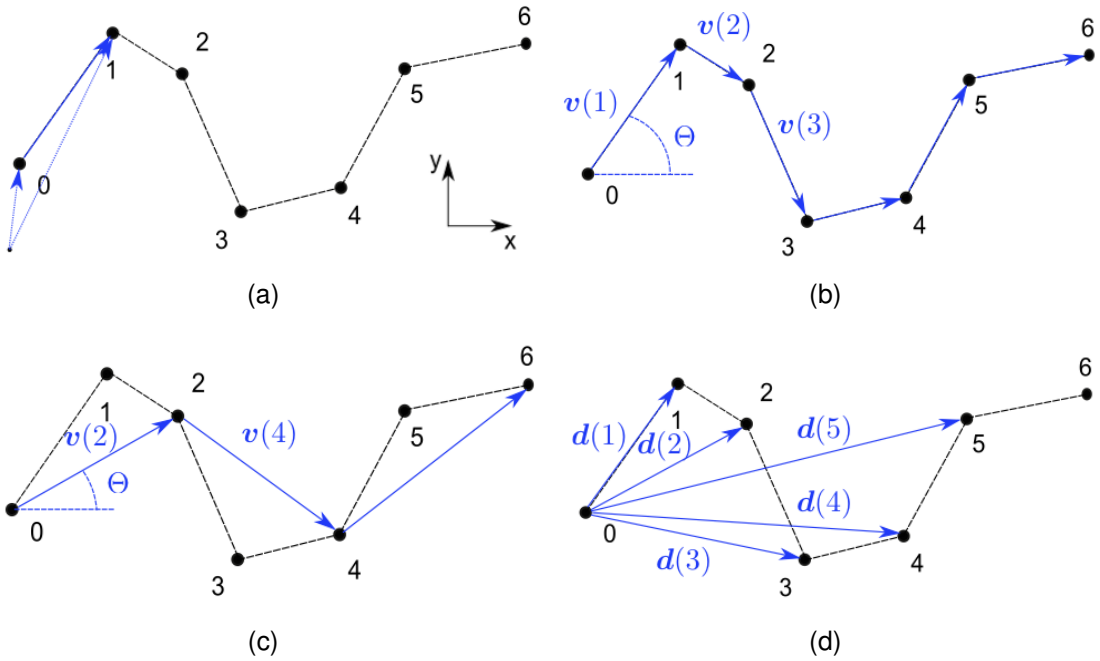

Fig. 4.13: Schematic presentation of calculating cell velocity and cell displacement: (a) Sample trajectory with cell centroid position for six time intervals taken from time-lapse microscopy, blue arrows indicates the position vector $\boldsymbol{r}$ at $t = 0.00$ s and $t = 0.02$ s. (b) and (c) Instantaneous velocity calculated for two different time lags: $\Delta\tau = 0.02$ s and $\Delta\tau = 0.04$ s (d) Displacement vector for the dispersion of the cell with respect to the starting point of the trajectory at $t = 0$ s.

Furthermore, we calculated the propagation angle $\Theta \in [0°, 360°]$ of each timestep with respect to the x-axis using the four quadrant arctangent function (atan2):

$$\Theta(t) = \text{atan2}\left(\frac{v_y}{v_x}\right). \tag{4.7}$$

Propagation angles of $\Theta = 0°$ and $\Theta = 180°$ correspond to cells which are moving parallel to the x-axis (figure 4.14(a)).

Angular Velocity

The instantaneous angular or turn velocity was calculated as the change in the direction of propagation between two subsequent time intervals

$$\omega(t) = \frac{\Theta(t) - \Theta(t - \Delta\tau)}{\Delta\tau}, \tag{4.8}$$

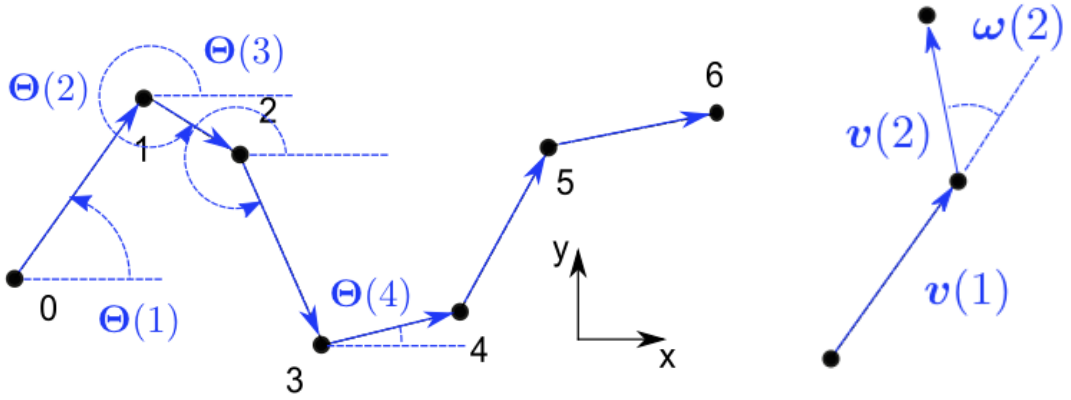

(a) (b)

Fig. 4.14: (a) Propagation angle with respect to the positive x-axis. (b) Schematic presentation of the angular velocity ω calculated from a change in the direction of propagation between two subsequent time steps.

with $\omega \in$ [-180°$/\Delta\tau$, 180°$/\Delta\tau$]. A negative value indicates that the cell is making a turn to the right, a positive value that it is turning to the left (figure 4.14(b)).

Mean Square Displacement

The mean square displacement (MSD) is calculated by taking the ensemble average over the squared displacements of all N cells in the system:

$$\langle \boldsymbol{d}(t)^2 \rangle = \frac{1}{N} \sum_{i=1}^{N} \boldsymbol{d}_i(t)^2 = \frac{1}{N} \sum_{i=1}^{N} (\boldsymbol{r}_i(t) - \boldsymbol{r}_i(0))^2 \tag{4.9}$$

Datapoints for longer times t, where the average was taken over an ensemble of less than $N_t = 5$ trajectories, were discarded.

Mean Square Angular Displacement

To determine the rotational diffusion coefficient we calculated the mean square angular displacement (MSAD) analogously to the MSD from the randomization of the direction of propagation:

$$\langle \Delta\Theta(t)^2 \rangle = \frac{1}{N} \sum_{i=1}^{N} (\Theta_i(t) - \Theta_i(0))^2 \tag{4.10}$$

Datapoints for longer times t, where the average was taken over an ensemble of less than $N_t = 5$ trajectories, were discarded.

Angular Autocorrelation Function

To investigate the directional persistence of motion we evaluated the angular autocorrelation $\Gamma(t)$ of the unit vector $\boldsymbol{e}(t)$ with

$$\boldsymbol{e}(t) = \frac{\boldsymbol{v}(t)}{|\boldsymbol{v}(t)|} \tag{4.11}$$

pointing at a given time t in the direction of motion of a cell. For the discrete time steps of our data, given the two components of the unit vector for each cell track of length L as the sequences $\{e_{x,i}\}_{i=0\ldots L-1}$ and $\{e_{y,i}\}_{i=0\ldots L-1}$, the so called directional autocorrelation function (DACF) was first calculated for each individual cell:

$$\chi(m) = \frac{\sum_{i=0}^{L-m-1} e_{x,i} \cdot e_{x,i+m}}{L-m} + \frac{\sum_{i=0}^{L-m-1} e_{y,i} \cdot e_{y,i+m}}{L-m} \tag{4.12}$$

Values for $\chi(m)$ were normalized to one for $m = 0$. We then calculated the DACF for the ensemble of cells by averaging over all individual trajectories:

$$\Gamma(m) = \frac{1}{N} \sum_{j=1}^{N} \chi_j(m) \tag{4.13}$$

4.6.2 Additional statistics from three-dimensional trajectories

In three dimensional tracking experiments, the velocity $\boldsymbol{v}(t)$, acceleration $\boldsymbol{a}(t)$ and displacement $\boldsymbol{d}(t)$ of a cell is calculated from three dimensional position vectors $\boldsymbol{r}(t)$ analogously to equations 4.4, 4.5 and 4.6. Additionally, we calculate two different propagation angles, the orientation of the swimming direction with respect to the xy-plane, the so called pitch angle θ, and the orientation of the swimming direction projected onto the xy-plane with respect to x-axis, the yaw angle Ψ (see figure 4.15).

The pitch angle is calculated according to

$$\theta(t) = \arcsin\left(\frac{\boldsymbol{v}(t)\cdot\boldsymbol{e}_z}{|\boldsymbol{v}(t)||\boldsymbol{e}_z|}\right) \tag{4.14}$$

with $\theta \in [-90°, 90°]$. Negative values ($\theta < 0$), or positive values ($\theta > 0$) correspond to cells swimming 'downward' or 'upward' with a negative or positive velocity component in z-direction respectively.

Projection onto the xy-plane and using the four quadrant arctangent function analogously to equation 4.7 yields the yaw angle

$$\Psi(t) = \text{atan2}\left(\frac{v_y}{v_x}\right) \tag{4.15}$$

with $\Psi \in [0°, 360°]$, where v_y and v_x are now components of the three dimensional velocity vector $\boldsymbol{v}(t)$.

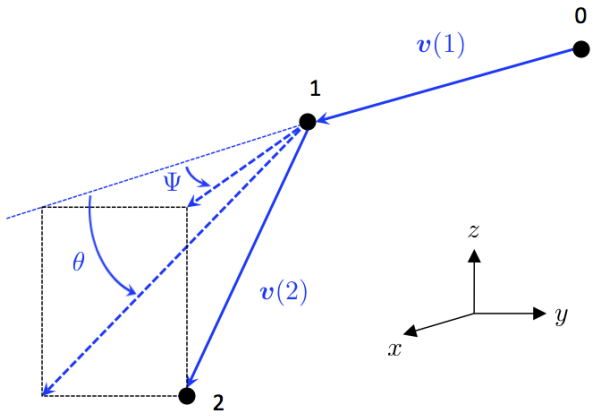

Fig. 4.15: Schematic presentation of the pitch angle θ and yaw angle Ψ, two different propagation angles describing the orientation of the three dimensional swimming direction. See text for description.

Angular velocity, Pitch angular velocity and Yaw angular velocity

In three dimensions the angular velocity is now defined as the angular change in the plane of the two three-dimensional velocity vectors and can be calculated using the dot product:

$$\omega(t) = \arccos\left(\frac{\boldsymbol{v}(t)\cdot\boldsymbol{v}(t-\Delta\tau)}{|\boldsymbol{v}(t)||\boldsymbol{v}(t-\Delta\tau)|}\right)/\Delta\tau \tag{4.16}$$

The pitch angular velocity is defined as the change in pitch angle between two subsequent time intervals

$$\omega_\theta(t) = \frac{\theta(t)-\theta(t-\Delta\tau)}{\Delta\tau} \tag{4.17}$$

and analogously the yaw angular velocity is calculated according to

$$\omega_\Psi(t) = \frac{\Psi(t)-\Psi(t-\Delta\tau)}{\Delta\tau}. \tag{4.18}$$

4.6.3 Identifying distinct trajectory patterns

Run- and Turn Event

Cell trajectories show periods of straight, persistent displacement (runs) and periods with fundamental changes in the direction of motion (turns). To determine whether a cell at a given time step n is in a run or turn state we used the sequence of its angular velocity magnitudes $\{|\omega_i|\}_{i=0\ldots L-1}$ and the magnitudes of its velocity $\{v_i\}_{i=0\ldots L-1}$.

The first step $i=0$ of a trajectory was scored as the beginning of a run-event if

$$|\omega_i|,|\omega_{i+1}|,|\omega_{i+2}| < \Omega_t \;\text{ or }\; |\omega_i|,|\omega_{i+1}| < \Omega_t \;\wedge\; \overline{(v_i, v_{i+1})} > 20\ \mu\text{m/s} \tag{4.19}$$

while it was counted as the beginning of a turn-event if

$$|\omega_i|,|\omega_{i+1}| > \Omega_t \;\text{ or }\; |\omega_i| > \Omega_t \;\wedge\; \overline{(|\omega_i|,|\omega_{i+1}|)} > \Omega_t. \tag{4.20}$$

A run ended with the beginning of a turn-event if conditon (4.20) was true, while a switch from a turn to the beginning of a run-event was scored if (4.19) was true. After careful testing, a cutoff angular velocity of $\Omega_t = 400°/s$ provided the best agreement with a

visual inspection to identify runs and fundamental changes of direction of a bacterial trajectory (figure 4.16(a)).

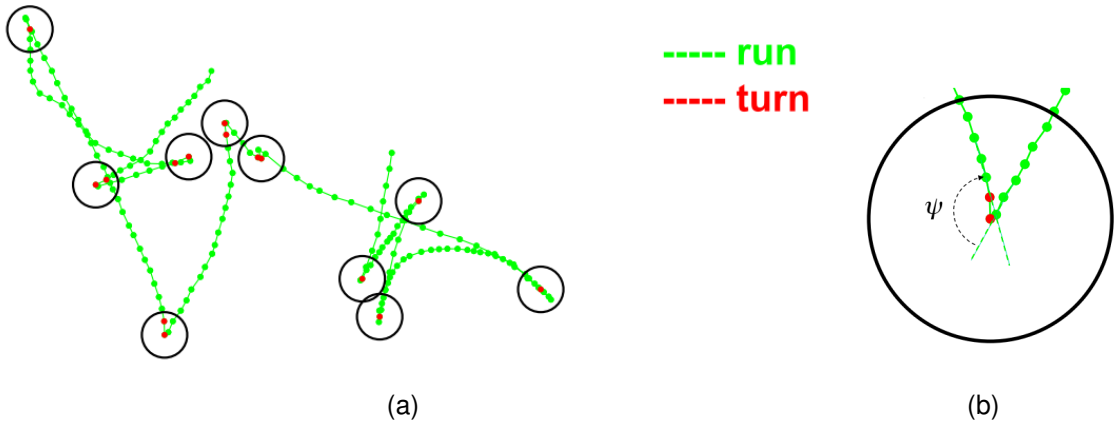

Fig. 4.16: (a) Cell trajectory with turning events identified by the algorithm (black circles) (b) definition of turning angle ψ.

Turning Angle

The Turning Angle ψ was calculated as the angle between two subsequent runs separated from each other by a turn event. Practically we first did a linear regression to fit the last three steps of a run and the first three steps of the subsequent run with a vector. The turning angle was then the angle between these two vectors (figure 4.16(b)). The three-dimensional turning angle Φ was calculated analogously by a linear fit to the three-dimensional run trajectories and lies in the plane spanned by the two subsequent runs.

Run Curvature

With the run segments and turn segments of the cell trajectory determined according to the procedure explained above, we also calculated the average curvature of a run $\kappa_n = \omega_n / v_n$ as the ratio between the average angular velocity ω_n and the average speed v_n of the corresponding run-segment.

Chapter 5

Results

5.1 Swimming cells in bulk fluid

As a starting point, we analyzed the free swimming behavior of our model organism *P. putida* in the bulk fluid without hydrodynamic surface effects. Cell trajectories have been recorded and motility statistics calculated according to the experimental procedures described in section 4.4.1 and section 4.6. In this section, we first present our main observations on the bacterial swimming pattern, in particular on the turn behavior and the bimodal distribution of run velocities. We then use these results in section 5.1.2 to develop a model for a two-dimensional run-reverse random walker, which qualitatively reproduces the experimental results on a dominating subpopulation of cells. Insights from the model on the biological processes behind this type of bacterial movement and its limits will be discussed at the end of the section.

5.1.1 Statistics of free-swimming cells

At first sight, trajectories of *P. putida* reflected the typical bacterial swimming pattern. Periods of straight, persistent displacements (runs) were interrupted by events, where the cell instantly stops and reorients or steers to change its direction of propagation (turn). This change in the swimming direction between two subsequent runs, which we measured by the turning angle ψ, is not random, as can be seen in the nonuniform distribution for ψ in figure 5.1(a). In approximately three out of five cases, the bacterium changes its swimming direction by $\psi_1 \approx 180°$, the cell reverses its direction of propagation. These reversal events are rapid and take 0.18 ± 0.02 s on average (figure 5.1(b)) with a median value of 0.08 s. A typical trajectory with a cell undergoing run-reverse

motion can be seen in figure 5.2(a). In the left picture, the trajectory is displayed with runs plotted in green and turns plotted in red. In the right picture, we show the corresponding swimming speed and absolute angular velocity of the cell as a function of time. This data confirms that during a run, the trajectory is straight and the speed is almost constant, while a turn is accompanied by a sudden jump in the speed and a peak in the angular velocity.

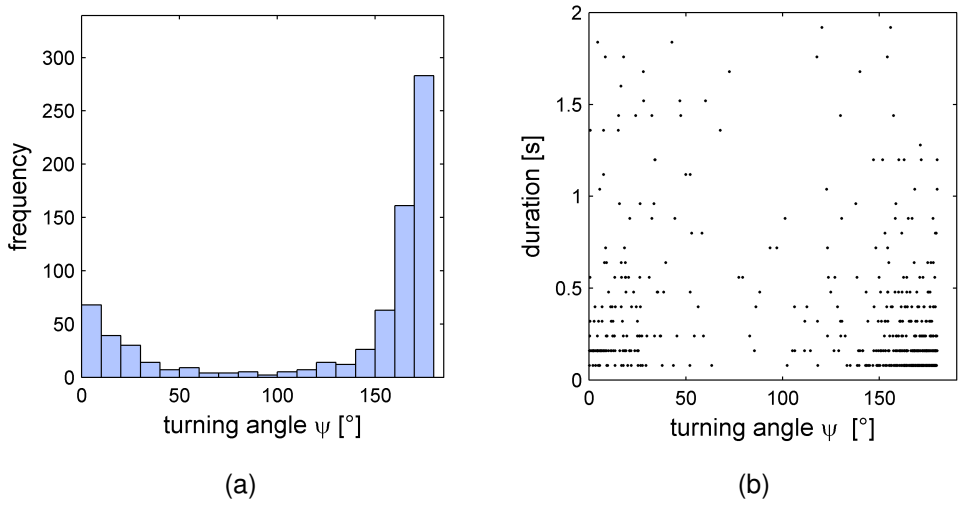

Fig. 5.1: (a) Frequency distribution of turning angles. (b) Duration of turning event and corresponding turning angle. In three out of five cases, the bacterium performs a fast reversal with a full 180° turn. The direction of propagation of two subsequent runs is anticorrelated.

The turning angle histogram showed a second peak, indicating that with a lower frequency as compared to the reversal events, the cell also performs a turn with an angle around $\psi_2 \approx 0^\circ$. The swimming directions before and after an event are similar. These turns on average take 0.40 ± 0.05 s (median value 0.16 s), which is longer than the reversal events and after a closer analysis we could classify them into two categories, pausing events and rapid speed changes:

In figure 5.2(b), the cell temporarily interrupts its run and enters a period of unstable jiggling motion. The speed decreases close to zero because the cell's center of mass remains on spot while the angular velocity is characterized by sharp peaks, reflecting the irregular motion of the cell body. After approximately 1.5 s, the cell resumes swimming and continues towards its previous direction of propagation. An example of a rapid speed change can be seen in figure 5.2(c). The angular velocity remains low but around $t \approx 0.96$ s the cell suddenly increases its speed. After the turn event, the speed has increased by a factor of two as compared to the previous run. Approximately $66\,\%$ of the

572 cell trajectories analyzed displayed reversal events with ψ_1 only, while the remaining trajectories contained pausing, speed change, and eventually reversal events.

In figure 5.3 we show the overall motility statistics calculated from all three types of trajectories. The mean square displacement (MSD) grew linearly with time t and could be fitted by $4Dt$, from which we retrieved $D = 227$ μm^2/s as the effective, translational diffusion coefficient. To describe only the diffusive regime, datapoints below the average run time corresponding to the ballistic regime of displacement were excluded from the fit. The mean square angular displacement (MSAD, figure 5.3(b)) was calculated as an ensemble and time average (see section 4.6.1) over all parts of the trajectory that were identified as runs. The strong increase at $t = 0.08$ s can be partly attributed to measurement noise in the determination of the propagation angle from which the MSAD is calculated. It also originates from the fact that during a run some cells displayed a constant 'wobbling' around their principal axis with a frequency near the time resolution of our time lapse recordings. This caused small changes in a cell's center of mass and thus in the evolution of the MSAD at the shortest time scale. From a fit with $2D_Rt$, we could estimate the rotational diffusion coefficient to $D_R = 0.073$ rad^2/s. This is close to the theoretical estimate

$$D_R = \frac{k_BT}{\gamma} \approx 0.062 \text{ rad}^2/s$$

for the rotational diffusion of *E. coli*, with $\gamma = 8\pi\eta r^3$ for the rotational frictional drag coefficient of a sphere with radius r =1 μm and η for the dynamic viscosity of water [6]. The runtime distribution for all cells has an exponential shape with a mean runtime of 1.12 s. The directional autocorrelation function shows a negative dip. To estimate the decay of directional correlations, we performed a fit with the generic function $A_0 \exp(-\tau/z)$ from which we retrieved $z = 0.78 \pm 0.07$ s. For a cell it takes 0.78 s on average until it has lost its directional correlation.

Apart from the sharp reversals with $\psi_1 = 180°$, the trajectory in figure 5.2(a), which is typical for approximately two third of the cell population, shows another remarkable feature: Upon a reversal, the average speed of the following run systematically changes by a factor of two. The cell alternates between fast runs and slow runs, in this example with an average speed around 42 μm/s and 24 μm/s. For a systematic analysis of this feature we plotted the difference in swimming speed before v_n and after a reversal v_{n+1} divided by the sum of both speeds $Q = (v_{n+1} - v_n)/(v_{n+1} + v_n)$ (from the available dataset), in figure 5.4 for the whole population of cells and in figure 5.5 for all trajectories containing reversals only. While the Q-distribution for all trajectories is centered around zero (figure 5.4(right)), the same distribution for reversal trajectories only (figure

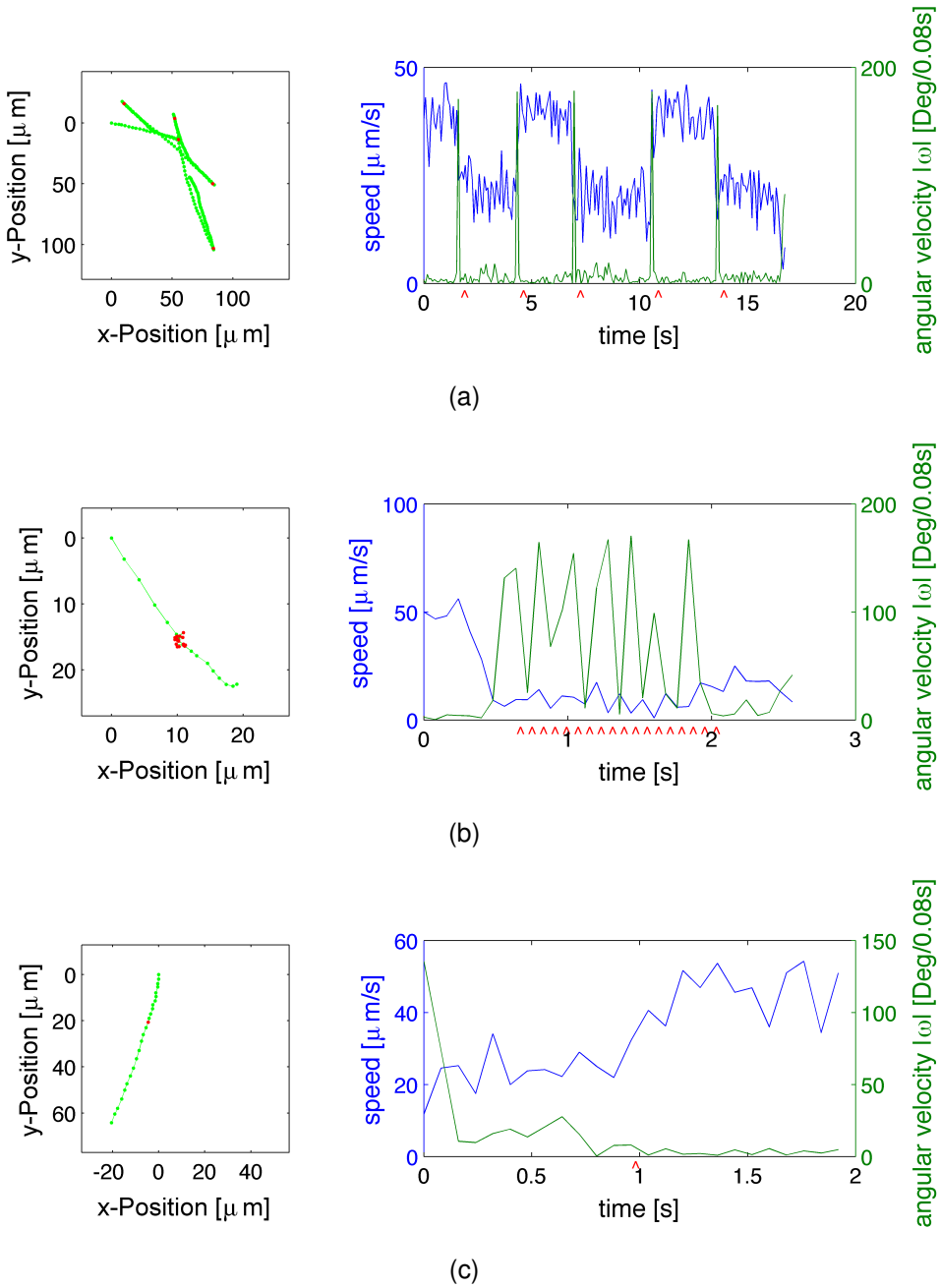

Fig. 5.2: Sample trajectories from motility statistics in the bulk fluid and corresponding speed and angular velocity over time: (a) Type I: Run-reverse pattern with alternating speeds, (b) Type II: Pausing-event, (c) Type III: Rapid speed change; Type I trajectories constitute 66 %, Type II and III 33 % of all trajectories. Red hats denote a turning event. See text for detailed description.

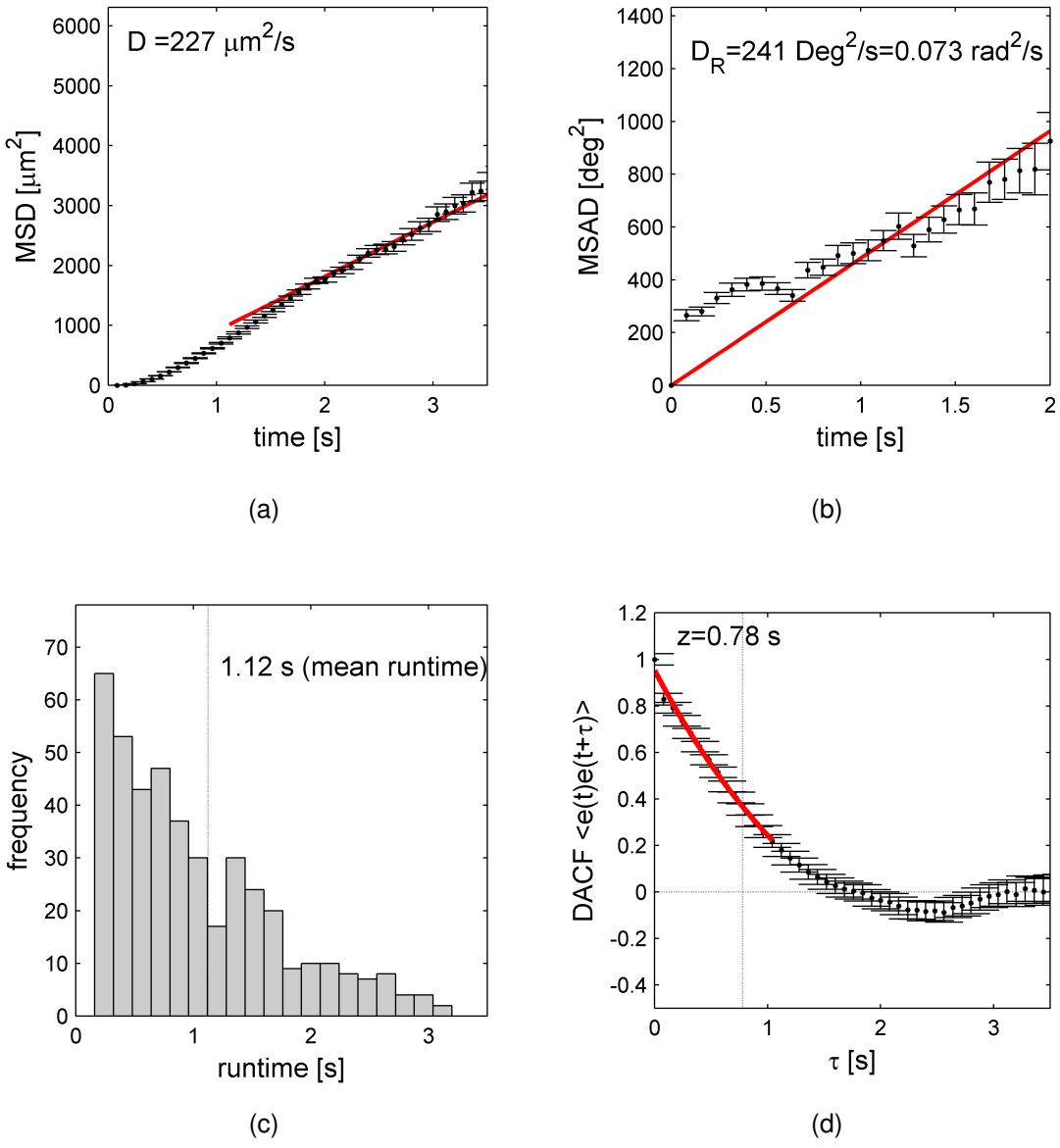

Fig. 5.3: Statistics from cell trajectories in the bulk fluid (IBIDI chamber). (a) Mean square displacement (MSD) together with linear least square fit $\langle \boldsymbol{d}(t)^2 \rangle = 4Dt$. The ballistic regime below the average runtime (1.12 s) was excluded from the fit. (b) Mean square angular displacement (MSAD, rotational diffusion) with linear least square fit $\langle \Delta\Theta(t)^2 \rangle = 2D_R t$. The strong offset at $t = 0.08$ s can be attributed to measurement noise. See text for description. (c) Distribution of runtimes. (d) Directional autocorrelation function (DACF) together with exponential fit $y = A_0 \exp(-\tau/z)$.

5.5(right)) shows two maxima at $Q = \pm 1/3$, clearly indicating that upon a reversal the swimming speeds v_{n+1} and v_n indeed change by a factor of two.

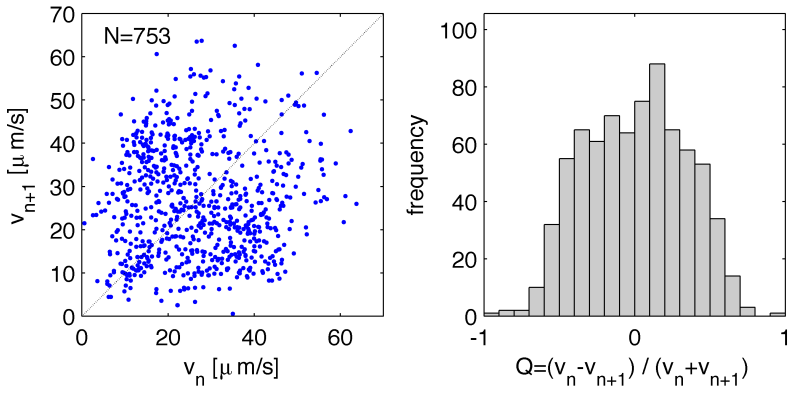

Fig. 5.4: (left) Scatter plot of average speeds of two subsequent runs v_{n+1} and v_n calculated from all trajectories. (right) Distribution retrieved from the same dataset. Calculated is the difference in average speed between each pair of runs divided by the sum of their average speeds.

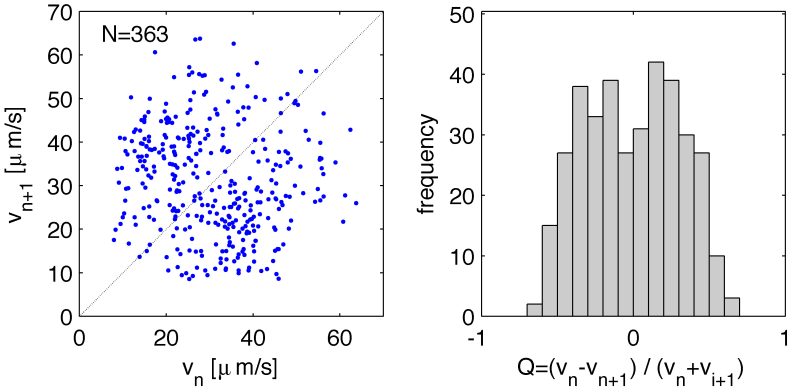

Fig. 5.5: (left) Scatter plot of average speeds of two subsequent runs v_{n+1} and v_n calculated from type I trajectories (reversal events) only. Points cluster left and right from the bisecting line, i.e. slow and fast runs alternate. (right) Distribution retrieved from the same dataset. Calculated is the difference in average speed between each pair of runs divided by the sum of their average speeds. Two peaks around $\pm$1/3 can be observed.

5.1.2 Modeling bacterial movement in the bulk [1]

Based on the experimental observations, we constructed a model that describes the spreading of a cell population in the bulk fluid. We restricted our analysis to trajectories of type I (see figure 5.2) showing reversals with $\psi_1 \approx 180°$ only, because they constitute the majority of the cell trajectories and are responsible for the dominating peak in the turning angle distribution (figure 5.1). Extending earlier work presented in section 3.4 our model included the following features:

- (i) The turn behavior between subsequent runs is reflected by a persistence parameter $\alpha = \langle \cos \psi \rangle$, defined as the mean cosine of the turning angle $\psi \in [0°, 180°]$. If cells randomly choose for a new direction, we find $\alpha = 0$. If cells perform perfect reversals with $\psi = 180°$ only, we have $\alpha = -1$. From our turning angle distribution we obtained $\alpha = -0.98$, which reflects the width of the dominating peak in figure 5.1.

- (ii) To account for rotational diffusion which perturbs the otherwise straight run segments, the unit vector $\boldsymbol{e}(t)$ reflecting the swimming direction of the cell obeys $\langle \boldsymbol{e}(0) \cdot \boldsymbol{e}(t) \rangle = \exp(-2D_R t)$ [6]. The rotational diffusion constant was determined from a linear fit to the mean square angular displacement determined from the experimental data, using the run segments of the trajectories only. We retrieved $D_R = 0.045$ rad^2 /s. This means that in the absence of turns, a cell performing a run would loose its directional correlation after a time of $1/(2D_R) = 22.2$ s.

- (iii) The run times are assumed to follow an exponential distribution (Poisson-statistics) with the mean runtime $\tau = 1.41$ s determined from the reversal trajectories only (see figure 5.6(b)). This means that at any given time during a run the turning rate $\lambda = \tau^{-1}$, is constant and independent of the duration of the previous run. Sine the duration of the reversal events is short compared to τ (median value 0.08 s, see figure 5.1(b)), the duration of the turn events can be neglected in the model.

- (iv) Upon each turn event, the swimming speed $v(t)$ of the cell systematically alternates between two constant values v_1 and v_2, corresponding to the average speed of the slow and the fast runs. The two speeds were determined from a double Gaussian fit to the distribution of run speeds (see figure 5.6(a)) and are estimated to $v_1 = 20.5$ μm/s and $v_2 = 38.0$ μm/s.

[1] The mathematical derivation of this model was done by Johannes Taktikos, Vasily Zaburdaev and Holger Stark, in close collaboration with the author.

This simple model can be seen as an extension of the approach by Lovely and Dahlquist [98] presented in section 3.4. While features (i)-(iii) are identical, the cell now alternates between a fast and a slow run instead of swimming with a single constant velocity v (iv). Following a derivation similar to the one in section 3.4, which is presented in the appendix A.3, we determined the velocity autocorrelation

$$\langle \boldsymbol{v}(0) \cdot \boldsymbol{v}(t) \rangle = e^{-(\lambda+2D_R)t} \left(\frac{v_1^2 + v_2^2}{2} \cosh(\lambda\alpha t) + v_1 v_2 \sinh(\lambda\alpha t) \right). \tag{5.1}$$

The diffusion coefficient in two dimensions $D = \lim_{t\to\infty} \langle \boldsymbol{d}(t)^2 \rangle / (4t)$ characterizing the mean square displacement was calculated by integrating the autocorrelation twice according to equation 3.28 yielding

$$D = \frac{2D_R(v_1^2 + v_2^2) + \lambda(v_1^2 + v_2^2 + 2\alpha v_1 v_2)}{6[2D_R + \lambda(1-\alpha)][2D_R + \lambda(1+\alpha)]}. \tag{5.2}$$

For equal swimming speeds $v_1 = v_2 = v$, we recovered the results from equation 3.29. With the given parameters from experimental data, we obtain an effective diffusion coefficient of

$$D_{v_1,v_2} = 436 \ \mu\text{m}^2/\text{s}$$

and for a cell swimming with a single average velocity of $\bar{v} = (v_1 + v_2)/2$ using equation 3.29 we get

$$D_{\bar{v}} = 191 \ \mu\text{m}^2/\text{s}.$$

Comparing the two ($D_{v_1,v_2}/D_{\bar{v}} \approx 2.28 > 1$) we see that movement with alternating speeds increases the diffusion coefficient. A population of cells performing a run-reverse random walk and swimming with alternating run speeds spreads faster than cells moving with an intermediate, constant swimming speed. The results of this simple analytic model are presented in figure 5.7 (blue dashed line) together with the experimental data. While the mean square displacement is described well, the model clearly does not reproduce the negative dip at $t \approx 2$ s in the experimental data of the DACF.

To improve our modeling approach we implemented the following modifications:

- (iii) Instead of an exponential distribution to describe the run times in figure 5.6(b) (red line), which ignores the local maximum around $t \approx 0.75$ s, we decided to use a Gamma distribution

$$p(t) = \frac{t}{(\tau/2)^2} \exp\left(-\frac{t}{\tau/2}\right)$$

with $\tau = 1.41$ s for the average length of a run. For smaller times the distribution increases linearly to the experimentally observed maximum while it also catches the exponential tail of the data for larger run times (red dotted line in figure 5.6(b)).

- (iv) To account for the speed variations, we no longer assume that the cell strictly alternates between the two constant values v_1 and v_2. Instead, for each run, the speed is now taken from a Gaussian distribution with a mean value v_1 or v_2 and standard deviation σ_1 and σ_2.

We treat turn behavior and rotational diffusion with parameter α and the constant D_R like in the previous modeling steps (i) and (ii). Because of the implemented changes, in particular the now non-exponential runtime distribution, the model can no longer be solved analytically. We simulated trajectories with the same length like in the experimental data. Additionally the information whether the cell starts with a fast or a slow run was taken into account according to the experimental data. The simulation results are shown in figure 5.7 (red dotted line).The model now accurately describes the mean square displacement and also recovers the negative dip in the directional autocorrelation function.

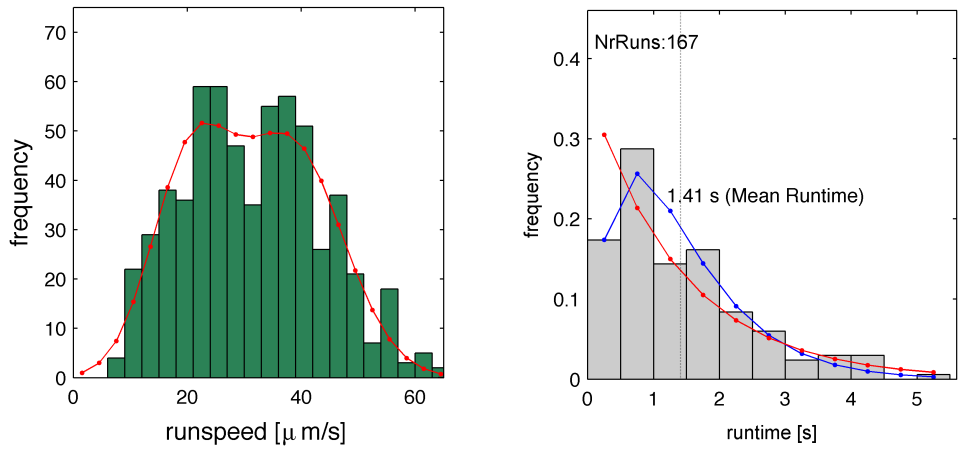

(a) (b)

Fig. 5.6: (a) Bimodal distribution of run speeds taken from trajectories showing reversal events only (type I). The sum of two Gaussians can be fitted with mean values $v_1 = 20.5$ μm/s, $v_2 = 38.0$ μm/s and standard deviations $\sigma_1 = 6.9$ μm/s and $\sigma_2 = 9.2$ μm/s. (b) Distribution of run times together with the fit of an exponential (blue) and a gamma distribution (red, see text) with mean run time $\tau = 1.41$ s. Only run times between two reversal events with $\psi_1 \approx 180°$ are considered.

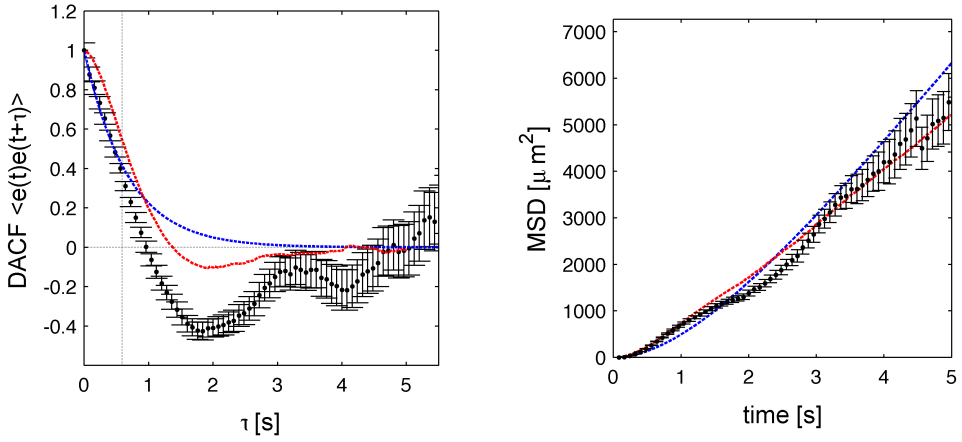

(a) (b)

Fig. 5.7: Experimental results for the directional autocorrelation function (a) and the mean square displacement (b) for cell trajectories displaying reversals only (black datapoints). The results from the analytic model model (blue dotted line) and the improved model with non-exponential runtime distribution (red dotted line) are shown.

5.1.3 Discussion

Our analysis has shown that free-swimming *P. putida* displays the typical bacterial swimming pattern with straight runs interrupted by fast reorientation events. When compared to the trajectories of the reference model organism *E. coli*, the reorientation events of *P. putida* qualitatively resemble sharp turns and are on average faster (< 0.08 s) than the duration of a tumbling event in *E.coli* (~ 0.10 s) [8, 34]. The observed distribution of turning angles is bimodal with a small peak at $\psi_2 \approx 0^\circ$ and a dominating peak at $\psi_1 \approx 180^\circ$. In the first case after a turn the cell will continue to swim in the direction of the previous run. In the second most likely case, the cell will reverse its direction of propagation upon a turn. Previous studies have already reported on the bimodality of the turning angle distribution but found that the dominant peak lies around 20° with a second one around 160° [38, 44]. This is somewhat contrary to our results. We note however, that the exact position of the peak as well as the overall shape of the distribution varies with the cell density and depends on the developmental stage of the cells, in other words on the time cells have spent in the growth medium, as Davis et al. have demonstrated [38]. Additionally, in our experiment cells originate from surface associated growth of colonies and swim in the hydrodynamically stable environment of a sealed microchannel under no flow conditions. In [38] cells were grown in a shaking culture and swimmers were recorded each time within the droplet of a cell suspension

on a glass coverslip where advection and fast evaporation might hinder the precision of the experiment. Because of this we conclude, that our experimental findings are in qualitative agreement with earlier measurements.

At first sight the purpose of the zero degree events among the otherwise dominant reversals, which were not included in the description of the model, remains unclear. The bacterium *Rhodobacter sphaeroides* is equipped with a single flagellum that can only rotate in one direction [3]. Its trajectories consist of straight runs lasting several seconds, interrupted by pausing events with a duration from 0.1 s up to a second [117]. In such a case, apart from rotational diffusion during runs, Brownian motion acting on the cell body during such intermittent stops is the only way a cell with a single unidirectional motor can reorient and randomize its direction of movement [3]. We suggest that for our run-reverse swimmer, pausing events might serve a similar purpose and enhance spatial randomization. Additionally, as the semiflexible flagella relax when the motor stops rotating, polymorphic transitions of the filament might lead to a change in the frictional resistance and further increase the reorientation of the cell body [3]. Recently, analysis of body rotation rates with one flagellum of the cell tethered to a glass slide confirmed that the motors of *P. putida* indeed display a stationary 'pausing' phase [24].

A run-reverse swimming pattern with a preferred turning angle at 180° is typical for marine bacteria like *Vibrio alginolyticus* [4, 102] and has been reported for numerous other bacteria among them *Pseudomonas citronellolis* and *Pseudomonas aeruginosa* [140]. All these bacteria use a single, polar flagellum for propulsion. If the flagellar motor rotates counterclockwise, in case of a left-handed helix, the bacterium is pushed forward, if the motor switches to clockwise rotation, the bacterium reverses its swimming direction the cell body now trailing behind and pulled by the single flagellum. In case of *P. putida*, which has several polar flagella, the situation is more subtle. Four different changes in its swimming mode triggering a reversal are possible which are depicted in figure 5.8. It has been proposed that a synchronized reversal of all flagellar motors causes the cell to reverse its direction and temporarily switch from a push- to a puller-swimming mode [64] (see figure 5.8(b)). It is generally assumed however, that a bundle of CW-rotating left-handed filaments is highly unstable and prone to jamming [100]. In order to enter and leave a reversal as a pusher with CCW-rotating flagella (figure 5.8(a)), the cell would need to rotate its body by 180°. Even if we increased the time resolution of our experiment fourfold up to 100 fps and performed comparable experiments, we never observed such turning of the cell body initiating a reverse event. For such an event to remain unnoticed in our image sequence, forces excerted by the rotating flagella would need to turn the body a full 180° within less than 0.02 s. Our calculation shows that this would require a force one order of magnitude higher than conventional estimates on the

propulsion power of flagella (see Appendix A.1).

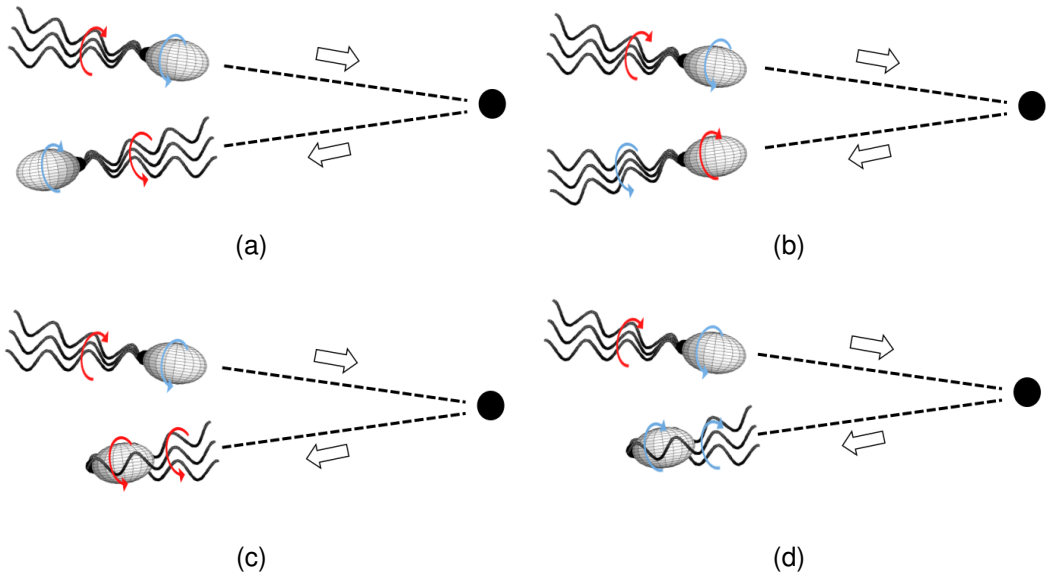

Fig. 5.8: Possible changes in swimming mode after a reversal: (a) the cell enters a reversal head forward, rotates its cell body by 180 degree and leaves the reversal head forward (push-reverse-push). (b) The cell enters a reversal head forward and emerges from it head backward. The propelling bundle of flagella first points away and after the reversal towards the direction of propagation (push-reverse-pull). (c) Upon a reversal flagellar at one polar end 'flip' over to the other side of the cell body. The cell leaves a reversal head forward with both cell body and flagellar bundle rotating in CCW-direction (push-reverse/flip-push). (d) During a reversal, flagellar motors change from CCW to CW-rotation. Hydrodynamic forces induce polymorphic transitions. The helical filaments change from left-handed to right-handed configuration and 'flip' over to the other side of the cell body. The cell leaves a reversal head forward with cell body and flagellar bundle rotating in CW-direction (push-reverse/flip push accompanied by polymorphic transitions). Red arc and blue arc arrows denote CCW- and CW-rotation respectively.

A possible assumption is thus that during a reversal, the flagella indeed switch from a pushing to a puller mode (figure 5.8(b)). Alternatively, one can imagine that the cell temporarily enters a hybrid mode in which some flagella reverse their direction and pull the cell while others are passively dragged behind. It is also possible, that due to the high flexibility of the hook, anchoring the filaments to the cell body, during a reversal the rotating bundle flips over from one pole to the other side of the cell body like an opening 'umbrella', as proposed for the reversals of *Bacillus subtilis* at an obstacle [26]. In such a case, the bacterium swimming as a pusher would perform a full reversal with or without changing the direction of its flagellar motors (figure 5.8(c) and (d)).

The different efficiency of the swimming as pusher or puller, or as a pusher where flag-

ella form a bundle at the non-flagellated side of the cell body might also explain the most striking observation in our experiments, the systematic change in swimming speed by a factor of two upon reversals. Such alternating swimming speeds have been reported for the monoflagellated *V. alginolyticus* in the presence of a solid boundary [102]. While forward and backward swimming speeds are equal in the bulk fluid, velocity and curvature of the run segments which can be attributed to the backward swimming mode, where the cell is pulling, are increased when cells are swimming close to the boundary [110]. As explained in section 3.3.3, the hydrodynamic surface effects act differently on a cell in the pusher or puller mode and also depend on the direction in which the flagellum or flagellar bundle is rotating. In section 5.2.2 we therefore investigate how the run-reverse pattern and in particular speed and curvature of subsequent runs behave near a single, open boundary.

We have presented a model for a run-reverse random walker with two levels of refinement. The simpler model could be solved analytically while the extended version relied on numerical simulation of cell trajectories. To the knowledge of the author it is the first time that the spreading of a population of cells which alternate between two distinct swimming speeds has been described analytically. For large times, the analytic expression with the assumption of exponentially distributed run times yields good agreement with the experimentally measured MSD. However, because the run times are distributed exponentially and since the directional autocorrelation is calculated as an average over a sufficient ensemble of cells, negative correlations expected from the run-reverse behavior average out and the description fails to reproduce the negative dip observed in the experimental data for the directional autocorrelation function. This is only reproduced in the extended version of the model, where the run times are approximated by a gamma distribution with a local maximum. The analytical model nevertheless underlines the fact that alternating speeds increase the diffusion constant and thus reduce the time needed to explore a given environment as compared to a bacterium that would swim at a constant, intermediate speed with the same run-reverse behavior.

5.2 Swimming cells in confined environment

5.2.1 Statistics in the presence of two solid boundaries

Apart from the movement of our model organism *P. putida* in the bulk fluid we wanted to investigate how cell trajectories and motility statistics are affected by the presence of solid boundaries. Analogously to Section 5.1.1 and according to the experimental procedures described in 4.4.1, cells from an overnight shaking culture were diluted but this time filled into a PDMS-microchannel, measuring 30 mm in length, 500 μm in width, and 10 μm in height. After approximately five hours, a total of 589 cells with an average speed above 10 μm/s were successfully tracked for at least two seconds or longer. Since bacteria are now swimming in close proximity to two surfaces, the presence of coexisting colonies on the surface can affect their movement and reorientation behavior. By manual inspection we therefore excluded all trajectories (187 in total) passing or reorienting near a colony at a distance smaller than the average cell length (~ 3 μm). Motility statistics were calculated based on a remaining population of 404 trajectories of healthy cells, which were not affected by the presence of the colonies.

Like in the bulk fluid case, cell trajectories showed periods of persistent displacement and rapid reorientation (figure 5.9(a)). The distribution of speeds is displayed in figure 5.9(b). It can be fitted by a single Gaussian with an average speed $v = 37.8$ μm/s (blue line). The overall shape however points to a bimodal behavior of the cells with a double gaussian fit yielding $v_1 = 31.5$ μm/s and $v = 55.9$ μm/s (red line). The distribution of angles between two subsequent runs (turning angle) showed a strong peak at 180 degree and a minor one around zero degree (figure 5.9(c)). In approximately nine out of ten cases after a reorientation event, cells swim into a direction directly opposing their previous direction of propagation (Run-Reverse behavior). Approximately 79 $\%$ of these fast reversals take less than 0.08 s (figure 5.9(d)).

Overall statistics for mean square displacement (MSD), mean square angular displacement (MSAD), runtimes and directional autocorrelation function (DACF) are displayed in figure 5.10. Compared to the free swimming case, rotational diffusion is enhanced more than one order of magnitude and, consistently, directional persistence, measured by the decay time of the directional correlation function, is reduced. We do not observe a strong offset in the MSAD like in the bulk fluid case (see figure 5.3(b)) which was caused by temporary wobbles of the cell body. Cells displayed smooth runs with a stable orientation of the cell body.

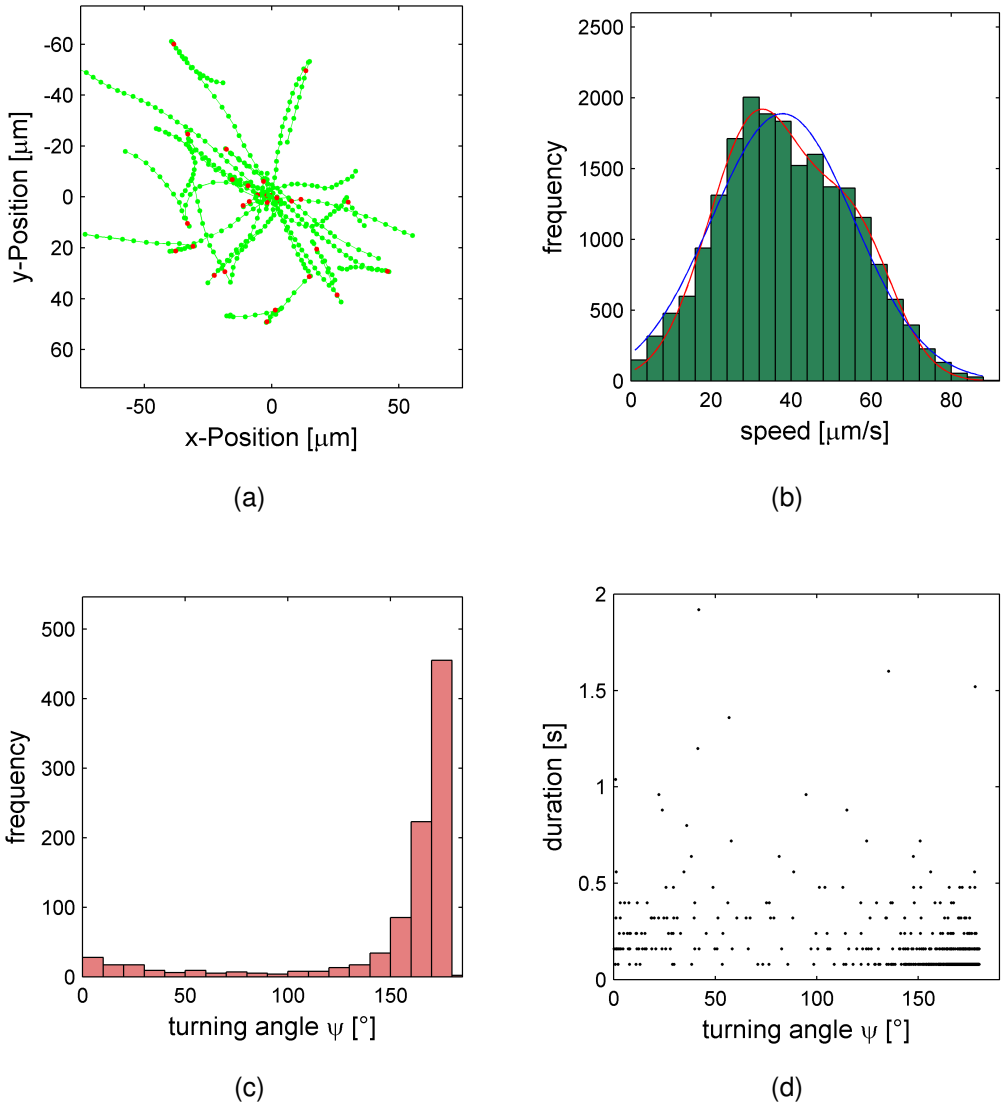

Fig. 5.9: Trajectories of cells swimming in a microchannel of 10 μm in height. (a) Sample trajectories with runs colored in green and turning events colored in red. (b) Distribution of cell speeds. Cells swim with an average speed of $v = 37.8$ μm/s, determined from the mean value of a Gaussian fit (blue line), which is approximately 50% faster than in the bulk fluid ($v = 26.9$ μm/s). The shape of the distribution can be also approximated by a superposition of two Gaussians, yielding $v_1 = 31.5$ μm/s and $v = 55.9$ μm/s (red line), which indicates a bimodal behavior of the cell speed. (c) Frequency distribution of turning angles. (d) Duration of turning events and corresponding turning angles. In approximately eight out ten cases, the bacterium performs a fast reversal with a full 180 degree turn and the direction of propagation of two subsequent runs is anticorrelated.

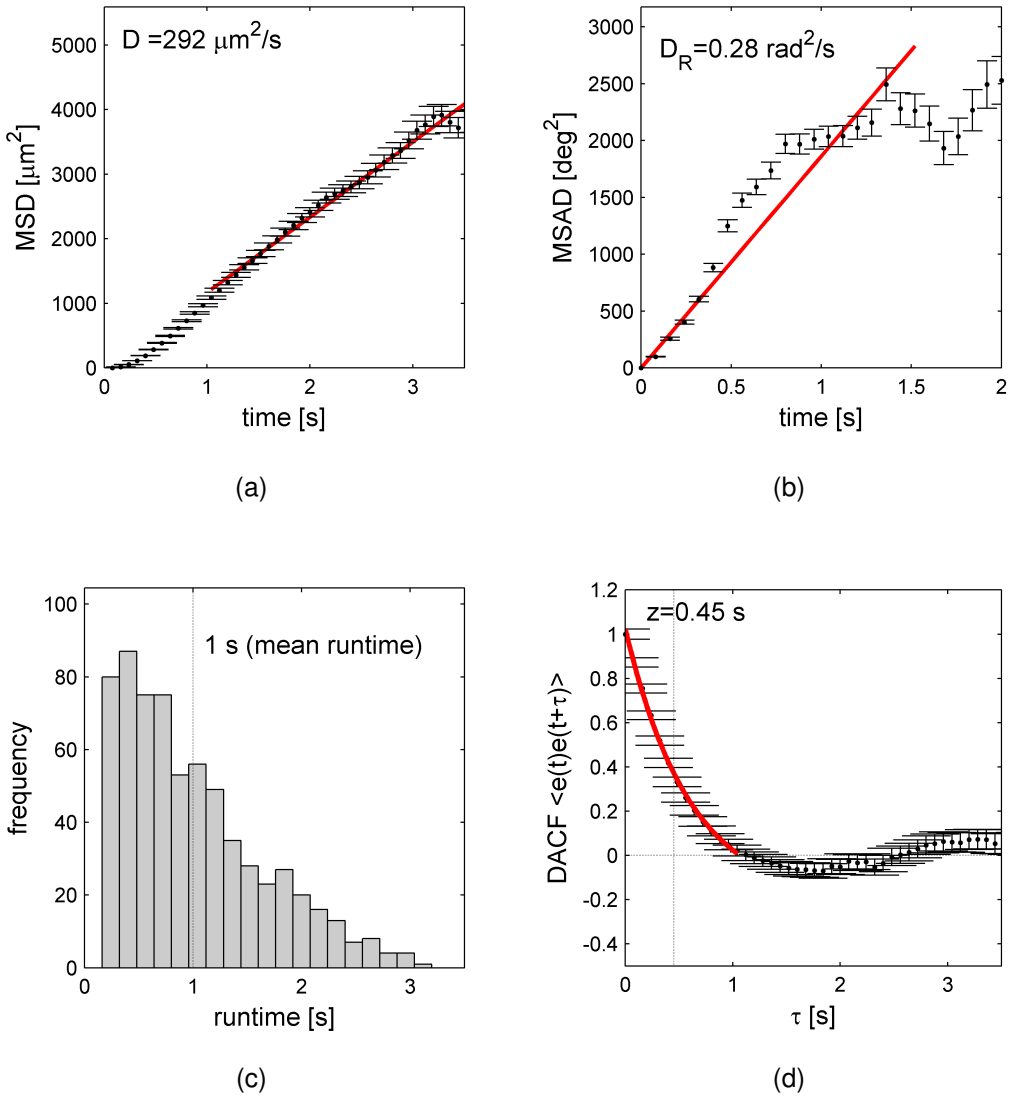

Fig. 5.10: Statistics of cell trajectories in 10 μm microchannel. (a) Mean square displacement (MSD) together with linear least square fit $\langle \boldsymbol{d}(t)^2 \rangle = 4Dt$. The ballistic regime below the average runtime (1 s) was excluded from the fit. (b) Mean square angular displacement (MSAD) with linear least square fit $\langle \Delta\Theta(t)^2 \rangle = 2D_R t$, (c) Distribution of runtimes, (d) Directional autocorrelation function (DACF) together with exponential fit $y = A_0 \exp(-\tau/z)$.

Like in section 5.1.1 we analyzed the speed change between two subsequent runs interrupted by a turning event, now for cells swimming 'sandwiched' between two boundaries. In figure 5.11(a) the average speeds of each run before and after a turn are shown in a scatterplot. The points cluster axially symmetric left and right from the bisecting line indicating that slow and fast runs alternate. The distribution in figure 5.11(b)

shows for each pair of runs the ratio between the speed difference and the sum of the two speeds. Two peaks at ± 0.25 can be identified, indicating that the speed before and after a reversal differs by a constant factor around ≈ 1.7. This is similar to the systematic speed change of free-swimming cells in the bulk performing reversals only. When compared to figure 5.5(b) the peaks in figure 5.11(b) are somewhat more pronounced.

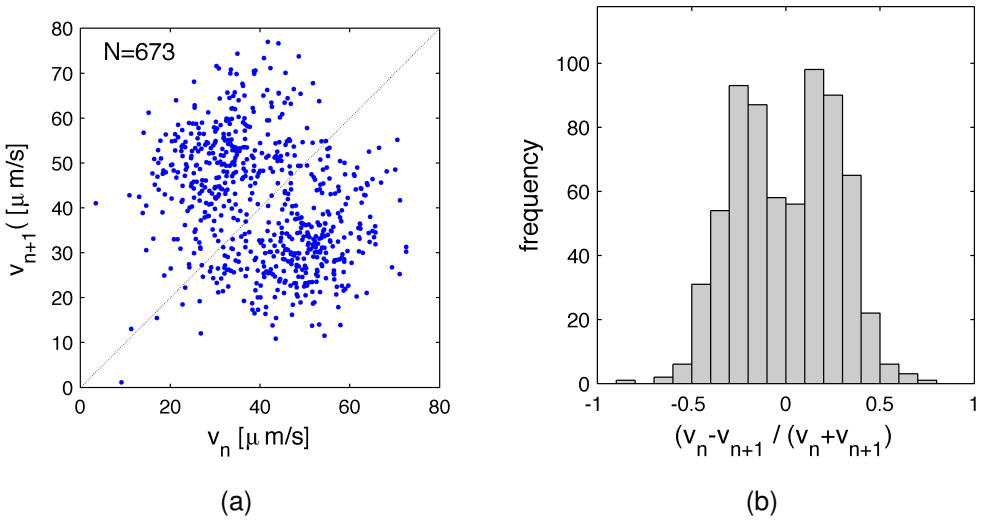

Fig. 5.11: (a) Average speed of two subsequent runs v_n and v_{n+1} from cell trajectories in 10 μm microchannel. Points cluster left and right from the bisecting line. Fast and slow runs alternate. (b) Distribution retrieved from same dataset like in (a). Calculated is the difference in average speed between each pair of runs divided by the sum of their average speed. Two peaks around ± 0.25 can be observed.

A sample trajectory of a cell swimming in the confined microchannel is shown in figure 5.12. As the cell is moving back and forth along a straight line (reversals indicated in red), run speeds alternate between $55 - 60$ μm/s and $25 - 30$ μm/s.

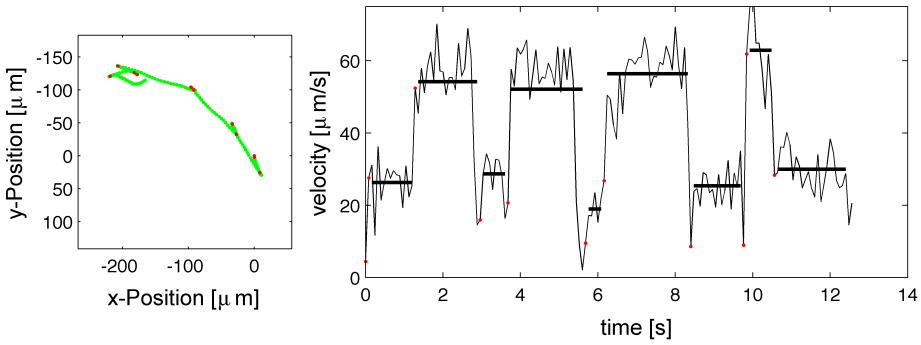

Fig. 5.12: Sample trajectory of a cell swimming inside a microchannel with a height of 10 μm. (left) Runs in green are interrupted by 180 degree turns (reversals) in red. The cell moves stepwise along a line. (right) Swimming speed of the same cell as a function of time: between its reversal events in red, the cell alternates between slow and fast runs (average speed of the corresponding run is designated by thick black line). The speed of fast and slow runs approximately differs by a factor of two.

5.2.2 Speed and angular velocity near a single boundary

We have learned in section 3.3.3 that the presence of a solid interface can have a significant effect on the speed of a swimming bacterium and the curvature of its trajectory. In this section, we will show how the ensemble and time average of speed and angular velocity (change in direction of propagation between two subsequent steps) of a given cell population changes as a function of the distance from the boundary. For this purpose, first, sets of two dimensional cell trajectories were acquired like in the bulk fluid case, following the protocol described in section 4.4.1. This time, we recorded images in a microchannel measuring 100 μm in height, at different focal planes, 10 μm apart from each other, starting with a sequence, where the microscope is focused on the glass bottom of the microchannel. Second, we acquired an additional information on the swimming height of a given cell from the first sequence recorded at the glass coverslip. We do this by detecting small differences in the sharpness of a cell's image as it moves closer or further away from the center of the focal plane while still being tracked by the algorithm. This procedure yielded an information on the z-position of swimming cells in the microchannel with a resolution of ± 1 μm (see section 4.5.2 for the full description).

In figure 5.13(a) and figure 5.14(a), we plot the speeds and angular velocities for all cells at all time points and the corresponding sharpness of the cell body as measured by the edge intensity calculated according to section 4.5.2) with the objective in focus

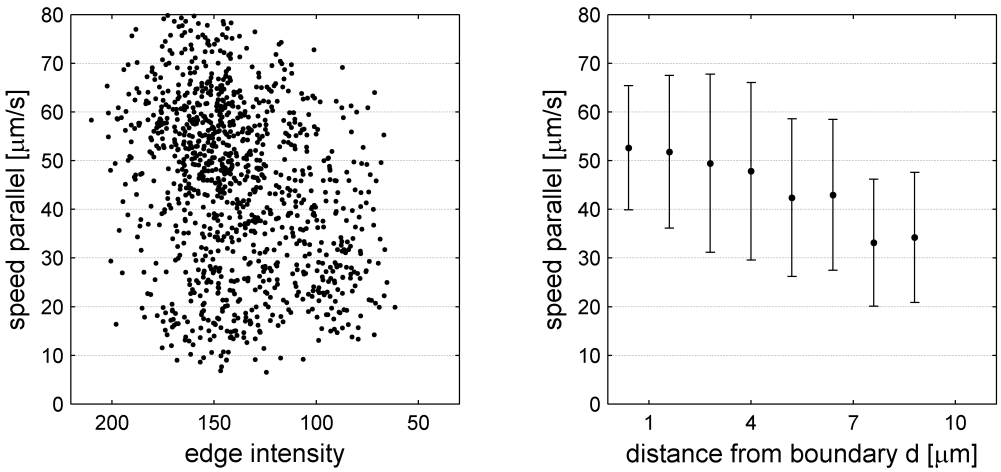

Fig. 5.13: (a) Cell velocity and corresponding sharpness of cell body (measured by edge intensity) for cells swimming parallel to the boundary, recorded with the microscope objective focused at the lower channel boundary (glass-coverslip). High values correspond to cells swimming close, low values to cells swimming further away from the focal plane. (b) Average velocities for data from (a), binned according to edge intensity. The corresponding distance to the wall has been retrieved from the calibration curve in figure 4.12. Cell speed increases in the proximity of the boundary. Datapoints from 'Series1-20x' are shown (see figure 5.15).

at the coverslip surface. Here, high values in edge intensity correspond to cells with a sharp contrast, which are swimming close to the lower channel boundary, while low values correspond to cells swimming further away from the surface. As figures 5.13(b) and 5.14(b) show, at an edge intensity around 100 (corresponding to a $d = 7 \pm 1$ μm from the boundary, see calibration curve in section 4.5.2), the average swimming speed has decreased from 50 μm/s to 35 μm/s, while the average angular velocities decreased from 12.5 deg/0.08 s to approximately 4 deg/0.08 s. Because hydrodynamic wall effects on speed and angular velocity can depend on the orientation of the cell's swimming direction with respect to the wall (see section 3.3.3), we restricted our analysis to datapoints where the swimming height changes less than 1 μm within a time $\Delta\tau = 0.08$ s, thus considering only cells moving parallel to the boundary.

To determine average speed and angular velocity as a function of the distance from the boundary, four datasets recorded with a 20x objective and one dataset recorded with at 40x magnification were available. For both objectives, a calibration curve was recorded so that we could convert the measured edge intensity into swimming height information (section 4.5.2). Three out of five of these datasets (Series1-20x till Series3-20x) were

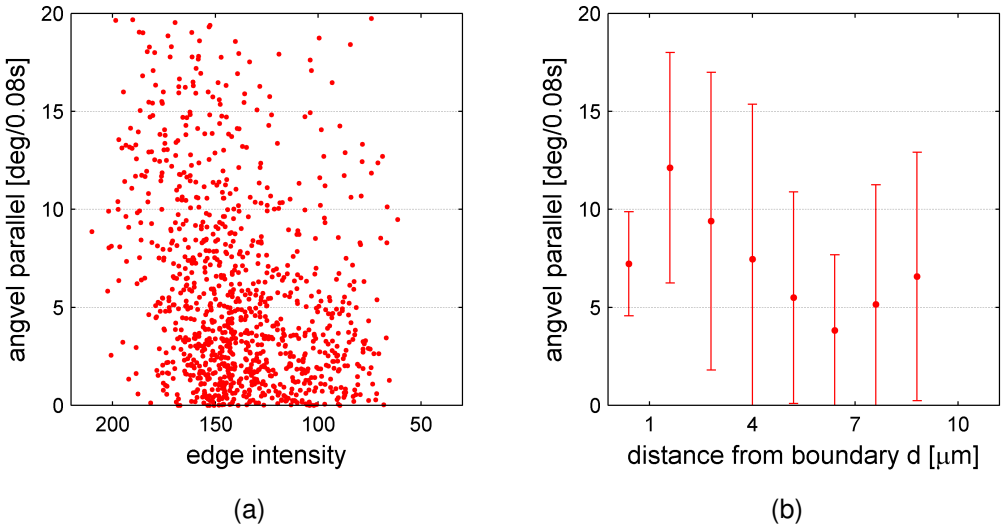

Fig. 5.14: (a) Angular velocity and corresponding sharpness of cell body (measured by edge intensity) for cells swimming parallel to the boundary, recorded with the microscope objective focused at the lower channel boundary (glass-coverslip). (b) Average velocities for data from (a), binned according to edge intensity. The corresponding distance to the wall has been retrieved from the calibration curve in figure 4.12. Angular velocity increases in the proximity of the boundary. Datapoints from 'Series1-20x' are shown (see figure 5.15).

recorded on a single day and with an identical cell population at different times within an interval of half an hour. The other two datasets (Series4-20x and Series5-40x) were recorded in two different experiments on different days.

The results for the average absolute values are shown in figure 5.15. As we can see in the figure 5.15(a), four of the datasets differ slightly in their average speed ($v = 38.2 \pm 4.3$ μm/s) in the bulk fluid at $d = 50$ μm, far away from the boundary, while the fifth dataset drops out with an average speed of $v = 20.8$ μm/s at a distance $d = 25$ μm, only half the value of the speed measured in the other four datasets. Below $d = 10$ μm, in the proximity of the surface, four out of five datasets show a moderate increase in speed with peaks at $d = 2 \pm 1$ μm and maximum speeds around 45 to 50 μm/s. In figure 5.15(b), which shows the angular velocities, differences between the first four datasets are less strong. The angular velocity in the bulk fluid around $\omega = 6.1$ deg/0.08 s increases up to 11.8 deg/0.08 s near the interface with a maximum at $d = 1 \pm 1$ μm for all datasets. The fifth dataset shows a strong peak in the angular velocity at $d = 15$ μm which is not observed any of the other four datasets. The experimental protocol was identical for all five datasets and careful inspection could not explain the deviation which we observed in the fifth dataset which was recorded with 40x magnification.

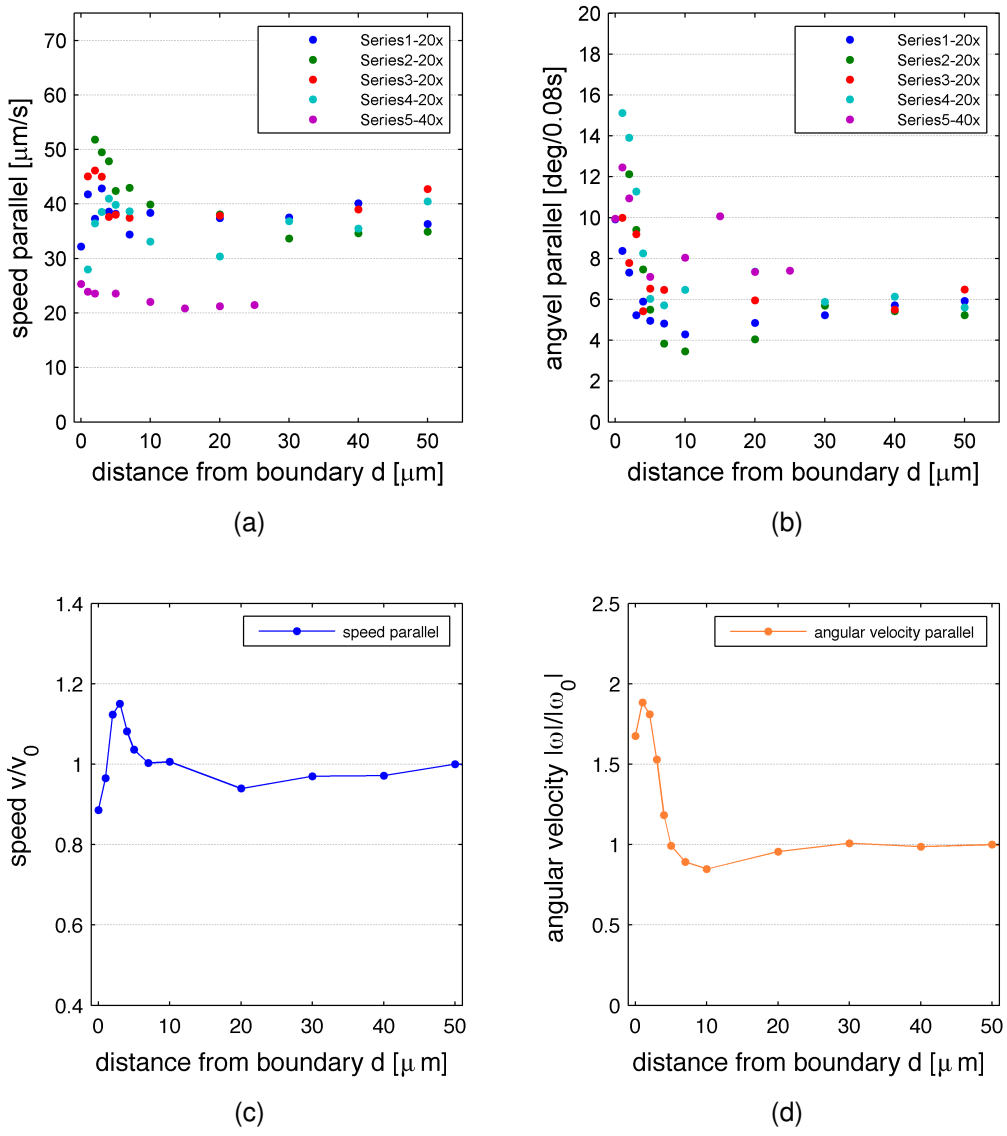

Fig. 5.15: (a) Average cell speed in the microchannel as a function of the distance from the glass coverslip for five different datasets. For distances below 10 μm, the speed increases in four out of five datasets with a peak at $d = 3 \pm 1$ μm. (b) Average angular velocity as a function of the distance from the boundary. For all five datasets, angular velocity increases for $d < 10$ μm, with a peak at $d = 1 \pm 1$ μm. (c) and (d) Average speed and average angular velocity (absolute value) as a function of the distance from a single boundary, calculated as the mean over the first four datasets (Series1-20x till Series4-20x from (a) and (b)) normalized by the bulk fluid value. Around $d = 3$ μm the average speed is 15% higher as compared to cells swimming at $d = 50$ μm. Below 3 μm, the average speed decreases by more than 20%. The average angular velocity increases by more than 70% as we observe cells closer to the surface and peaks at ≈ 1 μm, in direct proximity of the surface.

For a clearer picture, we normalized all measurement points by the bulk fluid values at $d = 50$ μm for the average velocity v_0 and average angular velocity ω_0 in the corresponding datasets. Then the mean over the normalized values from the first four datasets was taken for each distance d. The fifth dataset was excluded from analysis. For the speed, figure 5.15(c), we observed a local decrease at a distance of 20 μm. Below 10 μm, the averaged normalized speed increases and reaches a peak at $d = 3 \pm 1$ μm, where cells on average move 15% faster than in the bulk fluid. The average increase in angular velocity is more pronounced (figure 5.15(d)). In the proximity of the surface, it starts to increase below 8 μm and reaches a peak in the closest possible proximity to the surface $d = 1 \pm 1$ μm, that can be resolved by the axial resolution of our method. Right above the surface, cells describe circular trajectories with a 90 $\%$ higher angular velocity.

Additionally we provide the angular velocity as a signed quantity in figure 5.16. Here, negative values mean that the majority of cells during their runs perform a turn to the right, a CW circular trajectory when viewed from above, while positive values mean that cells are on average turning to the left, describing a CCW circle in the image sequence. In all five datasets the angular velocity for cells swimming close to the boundary becomes increasingly negative (see figure 5.16(a)). Cells are swimming in CW circles. As can be seen in the plot for the averaged quantities (figure 5.16(b)), the right-turn bias is peaked at $d = 1 \pm 1$ μm with a value of $\omega = -7.9$ Deg/0.08 s in the closest proximity of the wall which can be resolved by our method. This observation is consistent with predictions from the hydrodynamic wall effects on the rotating cell body and flagellar bundle (see section 3.3.3). If we assume that *P. putida* bacteria are propelled by a bundle of left-handed flagella rotating CCW [64], the rigid boundary will induce a torque as depicted in figure 3.11 which forces the cell on a right curved trajectory. For a more detailed discussion we refer to section 5.2.4.

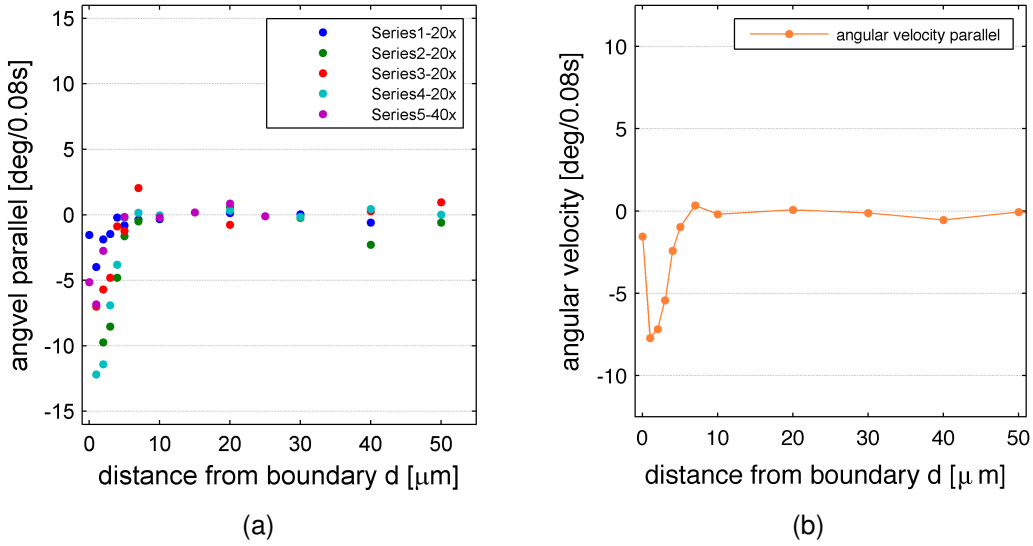

Fig. 5.16: Signed average angular velocity as a function of the distance from the boundary. Negative values correspond to a majority of cells performing a right-turn, positive values to cells performing a left-turn. (a) In all five datasets, for $d < 7\ \mu$m, the average angular velocity becomes increasingly negative with decreasing distance to the boundary. (b) Mean value taken over four datasets (Series1-20x till Series4-20x) from (a) showing a negative peak at $d = 1 \pm 1\ \mu$m. Near the boundary, cells are turning to the right with increasing magnitude.

Distinction between two swimming modes

In section 5.1.1 we have learned that *P. putida* perform reversal events with a dominating peak in the turning angle distribution at $\psi_1 \approx 180°$ and this was confirmed by motility statistics in the presence of two boundaries 5.2.1. We observed that upon a reversal event, the speed of the cell systematically changes by a factor of two. As discussed in section 5.1.3 it is unclear how flagella reorient during such a reversal but the systematic difference in swimming speed suggests that a reversal is accompanied by a temporary change in the cells swimming mode. Different possible changes in the swimming mode have been depicted in figure 5.8, while we were able to rule out the transition in figure 5.8(a) which would require an unrealistically fast cell body rotation. In the following, we want to concentrate on the remaining three possible transitions.

The previous section has confirmed that in close proximity to a single boundary, hydrodynamic forces affect the swimming speed and lead the cell to swim in circular trajectories with increased angular velocity. Additionally, we predict that the sign of the angular velocity i.e. whether the trajectory is curved to the right or to the left depends on whether the flagellar bundle is rotating in CW or CCW-direction (see section 3.3.3).

During the three remaining possible transitions, depicted in figure 5.17, the position of the flagellar bundle with respect to the cell body and/or the direction of flagellar rotation changes each time upon a reversal. We thus expect that a change in swimming mode will manifest itself in a sign change or a magnitude change in the curvature of the two subsequent runs. Here we will first discuss the wall effect on the trajectories depending on the individual transition in swimming mode. Then we will analyze the change in curvature of two subsequent runs before and after a reversal event and try to discriminate between the three transitions.

(1) In figure 5.17(a) we are looking from above at a cell swimming parallel to a single boundary, which one can imagine as being below the cell. On the left, the cell is entering a reversal head forward with its bundle of flagella trailing behind and rotating in CCW direction (red arc with arrow) while the cell body is rotating in CW direction (blue arc with arrow). The motors then synchronously reverse to CW-rotation and thrust is generated in the opposing direction (right cell picture). The cell leaves the reversal with its bundle of flagella ahead (push-reverse-pull). Because of the hydrodynamic effect, explained in section 3.3.3, the forces $\boldsymbol{F}_b$ and $\boldsymbol{F}_l$ both change sign as the direction of flagellar rotation and thus also the opposing rotation of the body changes. The cell enters a reversal as a 'pusher' with a run which is curved to the right ($\kappa_n < 0$) and leaves the reversal with a left curved run trajectory ($\kappa_{n+1} > 0$) as indicated by the dashed lines in green and red.

(2) Alternatively one can also imagine that during a reversal the bundle of rotating flagella anchored at one pole flips over to the other side of the cell body like an opening 'umbrella' as show in figure 5.17(b). The cell enters and leaves a reversal head forward as a 'pusher' with flagella rotating in CCW-direction in both cases (red arc with arrow). Because flagella remain anchored at the side of the cell body pointing towards the direction of propagation after the reversal, the body now also rotates in CCW-direction. Only the wall induced force $\boldsymbol{F}_b$ changes sign. The cell switches from a right-curved to a left curved run (push-reverse/flip-push). Because the lever arm of force (the distance along the cell axis between $\boldsymbol{F}_b$ and $\boldsymbol{F}_l$) is shorter during the alternative 'pusher' mode, we expect a smaller magnitude in the curvature ($|\kappa_{n+1}| < |\kappa_n|$), as compared to the curvature of a run in a conventional 'pusher' mode before the reversal.

(3) A reversal can be also induced by a ‚flip over' of the flagellar bundle where the direction of flagellar rotation changes (see figure 5.17(c)). A cell enters a reversal as a 'pusher'. If one or several motors switch to CW-rotation, hydrodynamic forces acting on the semiflexible filaments change the orientation of the helix from left-handed to right-handed as it has been observed during tumble events in *E.coli* [34]. Flagella flip over like in (2) and a stable, CW-rotating bundle forms at the other side of the

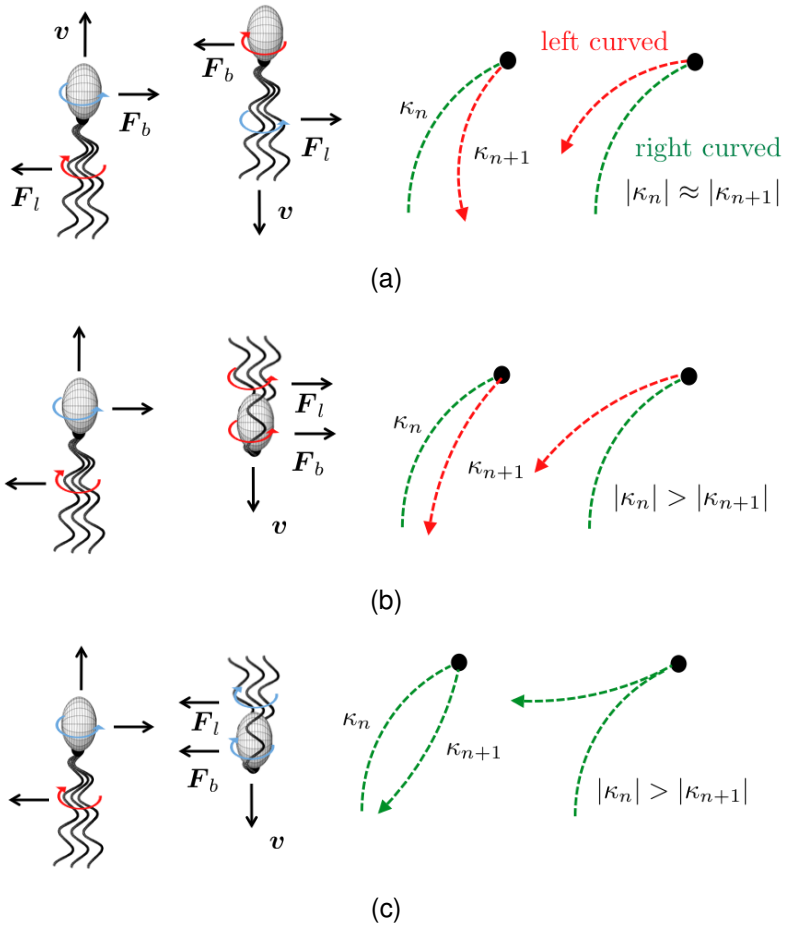

Fig. 5.17: Possible changes in swimming mode upon a reversal and corresponding wall induced effect on the curvature of a cell swimming close to a single boundary: (a) the cell enters a reversal head forward and emerges from it head backward (push-reverse-pull). The trajectory changes from right curved to left curved ($\kappa_n < 0$, $\kappa_{n+1} > 0$). (b) The cell enters a reversal head forward, and the CCW-rotating bundle 'flips' to the other side of the cell body. Upon the reversal, cell body and flagella both rotate in CCW-direction (push-reverse/flip-push). The trajectory changes from right-curved to left-curved with reduced magnitude ($|\kappa_n| > |\kappa_{n+1}|$). (c) During a reversal flagella switch to CW-rotation. Hydrodynamic forces acting on the flexible filaments change the helix from left-handed to right handed. The CW-rotating bundle 'flips' over to the other side of the cell body. Upon reversal, cell body and flagella both rotate in CW-direction (push-reverse/flip-push with polymorphic transition). The trajectory before and after the reversal is curved to the right. See text for closer description.

cell. Because of the conformational change, the filaments now generate thrust as a 'pusher' during CW-rotation. Only the wall induced force $\boldsymbol{F}_l$ changes sign. The cell enters and leaves the reversal with a right-curved trajectory (push-reverse/flip-push with polymorphic transition). Like in (2) because of the shorter lever arm force, we expect a

decrease in curvature magnitude ($|\kappa_{n+1}| < |\kappa_n|$).

Using the experimental data available on trajectories of cells swimming close to a single boundary we plot the average speed of two subsequent runs interrupted by a reversal event against each other (figure 5.18(a)). The points cluster left and right from the bisecting line. The speed difference of the two runs divided by the sum of the two speeds is shown in figure 5.18(b). Like in the bulk fluid case we observe two peaks at $\pm 1/3$. Upon a reversal, the average run speed changes by a factor of two. The more pronounced peak at $1/3$ indicates that in our given dataset, the recorded trajectories more often started with a fast run (on average $v_n > v_{n+1}$). From our dataset we determined that 61% of the cell trajectories started with a fast run.

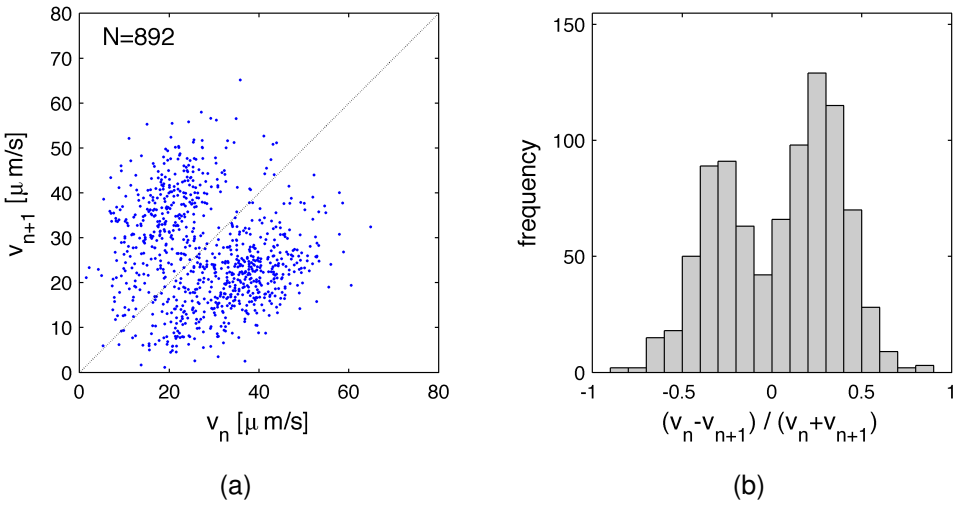

Fig. 5.18: (a) Average run speeds before (v_n) and after (v_{n+1}) a reversal event for a population of cells swimming close to a single boundary. (b) Frequency distribution of speed differences normalized by the sum of the two subsequent average velocities using the same dataset like in (a). Two peaks at $\pm 1/3$ can be observed. Interrupted by reversals, cells alternate between fast and slow runs with speeds differing by a factor of two on average.

To investigate possible systematic changes from a left curved to right curved run trajectory or vice versa upon a reversal we plot the curvatures of two subsequent runs against each other (figure 5.19(a)). Points clustering in the center of the second and fourth quadrant (counting CCW, starting with the upper right quadrant) would correspond to cells systematically changing the sign of their curvature, with $\kappa_{1,2} < 0$ for right-curved runs and $\kappa_{1,2} > 0$ for left-curved runs before or after a reversal. Strong changes in the magnitude of the curvature would lead to points clustering parallel close to the xy-axis. No clear tendencies could be identified in this plot. The number of points in the left half

(second and third quadrant) is higher than in the right half (first and fourth quadrant), meaning that within our dataset, more trajectories started with a run which is curved to the right ($\kappa_1 < 0$).

In figure 5.19(b) we show the magnitude changes in curvature divided by the sum of the two curvature magnitudes. No systematic change in curvature magnitude between two subsequent runs could be observed. The plot in figure 5.19(c) shows the frequency distribution of the curvature product normalized by the sum of the curvature magnitudes. Negative values correspond to events where the curvature of the cell trajectory changes sign upon a reversal (from right curved to left curved or vice versa), positive values correspond to subsequent runs with the same curvature sign (from right curved to right curved or from left curved to left curved)). The distribution is centered at zero. Sign changes in curvature are equally likely to occur as no sign changes. For completeness, in the appendix A.2 we present the analysis on curvature changes for cells swimming in between two solid boundaries based on the motility statistics used in section 5.2.1. Again no indication for a sign change or a systematic change in curvature magnitude upon a reversal was found.

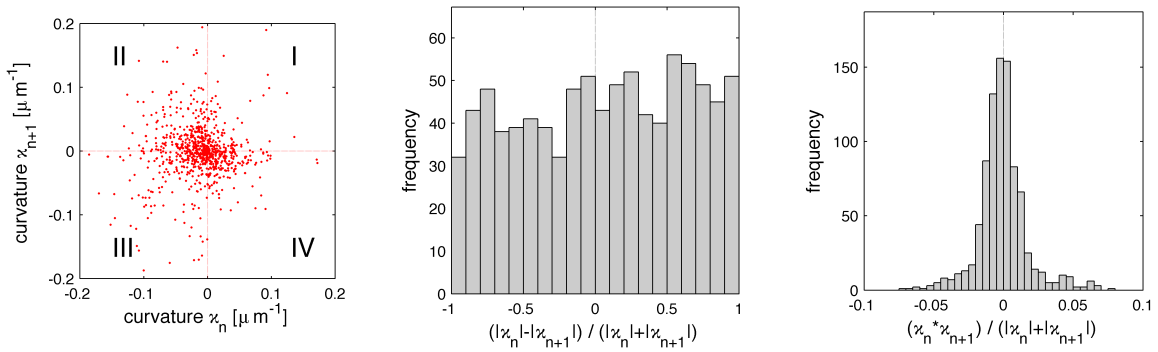

(a) (b) (c)

Fig. 5.19: (a) Average curvature of runs before (κ_n) and after (κ_{n+1}) a reversal event for a cell population swimming close to a single boundary. Numbers denote the corresponding quadrant. (b) Frequency distribution of differences in curvature magnitude normalized by the sum of the two magnitudes. (c) Frequency distribution of the curvature product normalized by the sum of the two magnitudes. See text for description.

Additionally we wanted to correlate possible curvature changes with changes in the average run speed. Each trajectory consisted of a sequence of numbered run segments interrupted by reversals. Two average curvatures and two average speeds were then calculated for each trajectory as the mean over all odd run segments (κ_o and v_o) and all

even run segments (κ_e and v_e). In figure 5.20 the difference in the curvature magnitude between odd and even segments ($|\kappa_o| - |\kappa_e|$) versus the normalized velocity difference between the odd and even segments ($(v_o - v_e)/(v_o + v_e)$) is shown. One datapoint correspond to one trajectory in the dataset. Points clustering in the center of the first and third quadrant would indicate a positive correlation between curvature and speed. Cells would then alternate between fast curved runs and slow straight runs. If points accumulate in the center of the second and fourth quadrant the correlation would be negative. Cells would then alternate between slow curved runs and fast straight runs. However, the scatterplot indicates no such correlation. Systematic changes in cell speed upon a reversal are not accompanied by systematic changes in the curvature magnitude of the run trajectory.

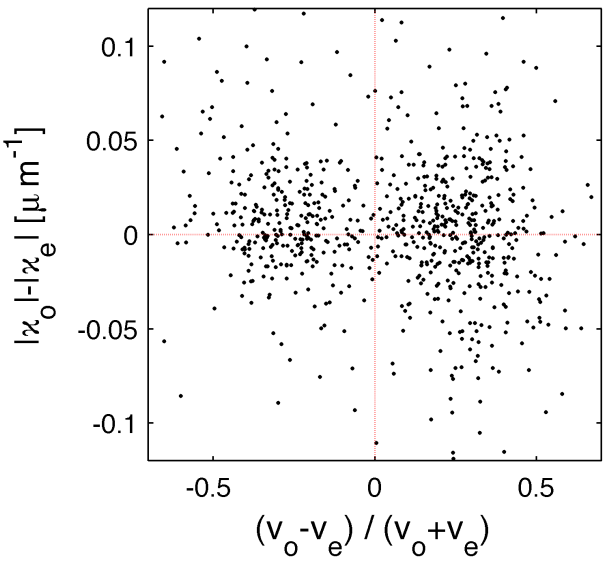

Fig. 5.20: Correlations between curvature and speed: Difference in curvature magnitude between odd ($|\kappa_o|$) and even segments ($|\kappa_e|$) as a function of the normalized speed difference. See text for description.

In conclusion, cells swimming near a single rigid boundary showed the same run-reverse pattern with alternating periods of fast and slow runs as it has been observed in the bulk fluid. Hydrodynamic interactions with the wall induce a torque which alters the direction of propagation (curvature) during a run. Cell trajectories follow a CW or CCW-circle. To discriminate between possible changes in the swimming mode, we analyzed the change in curvature between two subsequent runs. As figure 5.19(c) shows, no systematic sign change in the curvature, which would correspond to a switch from

a right curved 'pusher'- to a left curved 'puller'-mode (transition (a) in figure 5.17) could be observed. Though not in a systematic fashion, upon a reversal, the magnitude in curvature changes (see figure 5.19(b)). This would indicate that, upon a reversal, the cell changes its swimming mode according to transition (b) or (c) displayed figure 5.17. We suggest that to initiate a reversal, a cell is indeed flipping its flagellar bundle to the other side of the cell body. For a more detailed discussion we refer to the end of this section.

5.2.3 Three-dimensional motility statistics in strong confinement

Fast Z-scanning, using a piezo driven objective turret together with long-term high speed recordings, as described in section 4.4.2, gave us the opportunity to extend our analysis to three-dimensional trajectories. While the analysis of the sharpness of cell edges in the gray scale images, presented in section 5.2.2, allowed us to determine the swimming height with a resolution of one micrometer, we are now able to determine the z-position of a cell in the microchannel with submicron accuracy. Furthermore, from the segmented Z-stacks, we have the full information on the cell ellipsoid, the three dimensional morphology of the cell. In the following section, we show first that we recover the main observation from section 5.2.1, that cells in a confined environment perform a run-reverse random walk, with a peak in the turning angle distribution around 180 degrees. In the second part, we investigate how a cell's speed and angular velocity (the curvature of its trajectory) depends not only on the distance to the solid boundary but also on its orientation in the microchannel, its pitch angle θ, the angle of rotation with respect to its lateral axis.

The series of plots in figure 5.21 show a sample trajectory from our dataset, which has been recorded in a microchannel measuring $10\ \mu$m in height and $500\ \mu$m in width. Starting in the middle of the microchannel (blue star) the cell executes straight runs (plotted in green) for one to two seconds, which are interrupted by sharp turns (plotted in red). During the runs, the cell changes its swimming height, either ‚diving' towards the lower boundary or ‚climbing' towards the upper boundary of the microchannel. Following the speed over time (figure 5.23(a)), we see again that upon a sharp turn the speed changes by a constant factor.

The sample trajectory in figure 5.22 shows a cell starting close to the lower boundary of the channel. After a moderate climb it reverses its direction in the middle of the channel. During the following run, which lasts more than five seconds, it first swims back towards the lower boundary and then changes its direction of propagation towards the upper

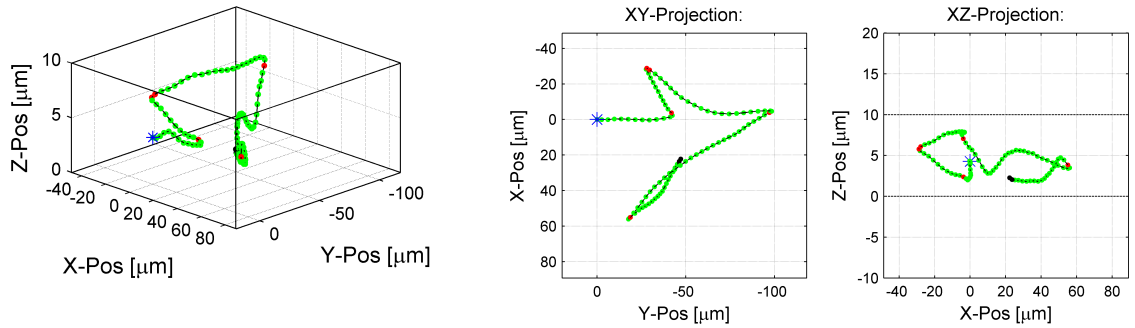

(a) (b)

Fig. 5.21: Sample trajectory from three dimensional cell tracking with runs plotted in green and turn events plotted in red. The blue star marks the first datapoint of the trajectory. (a) xyz-perspective, (b) Projection on the xy-plane (left) and on the xz-plane (right). The channel boundaries are indicated by black dashed lines. The cell performs four sharp turns at different distances from the channel walls: Two around $d = 5$ μm (Z-position) and two close to the upper and lower boundary of the microchannel.

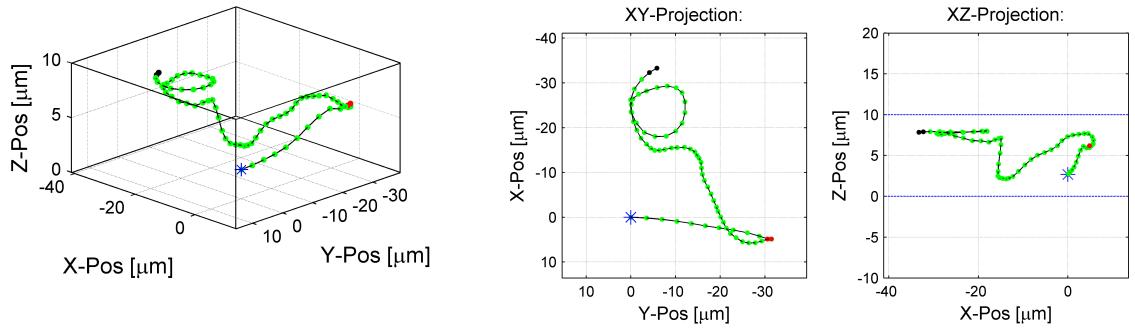

(a) (b)

Fig. 5.22: Sample trajectory from three dimensional cell tracking with runs plotted in green and turn events plotted in red. The blue star marks the first datapoint of the trajectory. (a) xyz-perspective, (b) Projection on the xy-plane (left) and on the xz-plane (right). The channel boundaries are indicated by black dashed lines. After a sharp turn, the cell performs a run, first propagating towards the lower then apruptly changing towards the upper channel wall. Near the upper channel wall, hydrodynamic interactions with the boundary force the cell into a clockwise circular path when viewed from above.

boundary. At the end of the second run, interaction with the upper boundary forces the cell onto a circular path with a radius of approximately four micrometers. While moving in circles, the cell maintains a stable distance $d = 0.95 \pm 0.23$ μm to the upper boundary. Speed and absolute angular velocity of the cell are shown in figure 5.23(b). After the turn at $t = 1.04$ s, indicated by the peak in the angular velocity (green curve), the speed increases at the end of the second run as the cell approaches the upper boundary. Though somewhat noisy, the circular path of the trajectory at the end of the run is reflected by an increased angular velocity for $t > 4$ s.

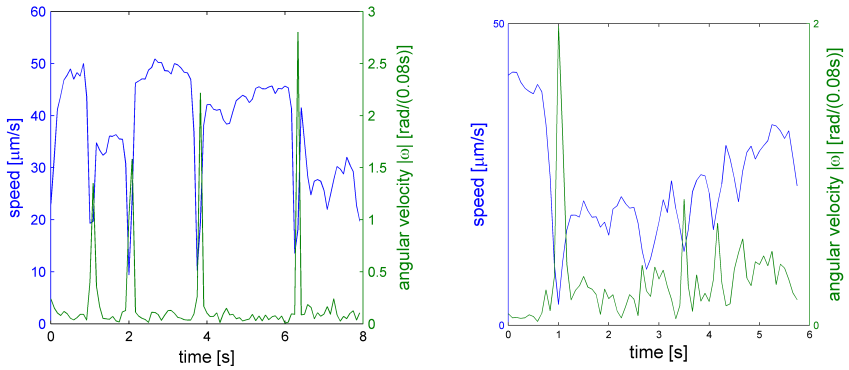

Fig. 5.23: (a) Speed and absolute angular velocity as a function of time for the sample trajectory shown in figure 5.21. Runs at different average speeds are interrupted by four sharp turns with a high instantaneous angular velocity. (b) Speed and angular velocity as a function of time for the sample trajectory shown in figure 5.22. A fast run ends with a sharp turn (high angular velocity). In the following run, the speed changes as the cell approaches the surface, where it starts to follow a circular path with increased angular velocity.

The distribution of turning angles is displayed in figure 5.24. In the left plot, we show the three-dimensional turning angle Φ, calculated as the angle between the smoothed velocity vectors at the end and at the beginning of two subsequent runs, which are interrupted by a turn. The right plot shows the two dimensional turning angle ψ, in other words the angular change between the velocity vectors of the subsequent runs, but now projected onto the xy-plane parallel to the boundaries. The two dimensional angle lies in the xy-plane and is aequivalent to the yaw angle. It is the same quantity that has been measured in the two dimensional datasets.

The distribution for Φ was peaked at 165 degrees. In approximately four out of five turn events, the cell reverses its direction of propagation ($\Phi >$ 150 degrees). Unlike in the turning angle histogram in section 5.2.1, no second peak around zero degree was observed. The projected turning angle distribution for ψ showed a peak around

180 degree. Additionally, more events with small angles ($\psi < 30$ degrees) could be observed. Results are consistent if we consider the fact that we are looking at the projection of a three dimensional trajectory. Turning angles Φ below 90 degrees are thus underestimated in the projection while turning angles Φ above 90 degrees are overestimated if the runs before and after the turn do not lie in the plane parallel to the surface. Consequently, in the ψ-histogram, values from the Φ-histogram below 90 degrees are ‚shifted' to the left and values above 90 degrees are shifted to the right. In the appendix A.4 an estimate on the systematic bias in the two dimensional turning angle distribution is presented.

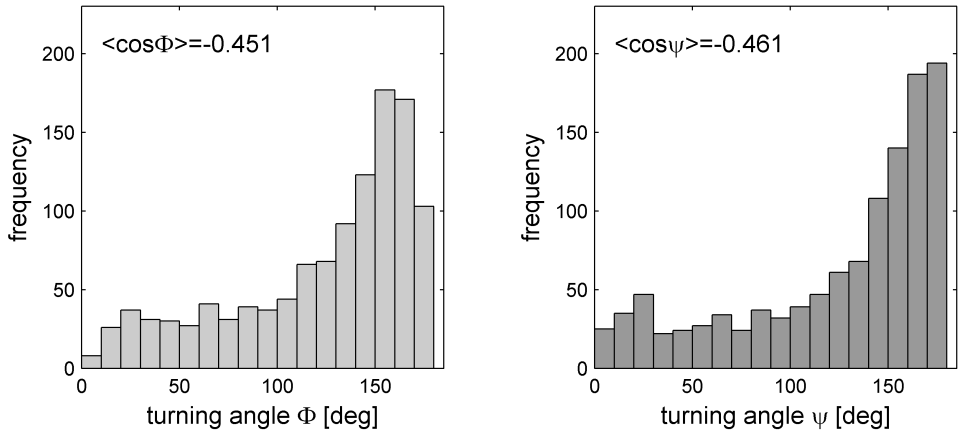

Fig. 5.24: (a) Distribution of three dimensional turning angle: The histogram is peaked at 165 degrees. (b) Distribution of two dimensional turning angle (angle between two subsequent runs, projected into the xy-plane): in the two-dimensional projection, angles from (a) below 90 degrees are underestimated while angles above 90 degrees are overestimated. The original peak at 165 degree is shifted towards 180 degrees. See text for closer description.

In section 5.2.2 we have analyzed how speed and angular velocity of the cell are affected by the presence of a single boundary. Here we look at the speed and absolute angular velocity ω from three dimensional trajectories as a function of the position d in the microchannel (see figure 5.25), measured from the bottom, where the population of cells is now performing confined swimming between two solid boundaries. Like in section 5.2.2 we want to compare only cells swimming parallel between the two boundaries. Therefore cells moving with a pitch angle $|\theta| >= 5$ degrees with respect to the xy-plane are excluded from statistics. The average swimming speed is highest in the middle of the microchannel ($v(4.5\ \mu\text{m}) \approx v(5.5\ \mu\text{m}) \approx 30\ \mu$m/s), where cells are the

farthest away from the boundary. Close to the upper and lower channel wall, the speed decreases down to $v(1\ \mu\text{m})$=$v(9\ \mu\text{m}) \approx 25\ \mu$m/s. The mean angular velocity is lowest in the middle of the microchannel, while it is twice as high near the channel boundaries ($\omega(1\ \mu\text{m}) = \omega(9\ \mu\text{m}) \approx 112$ degrees/s). This means that trajectories of cells constantly swimming in close proximity to the boundary are on average curved with a radius of $r = v/\omega \approx 95\ \mu$m.

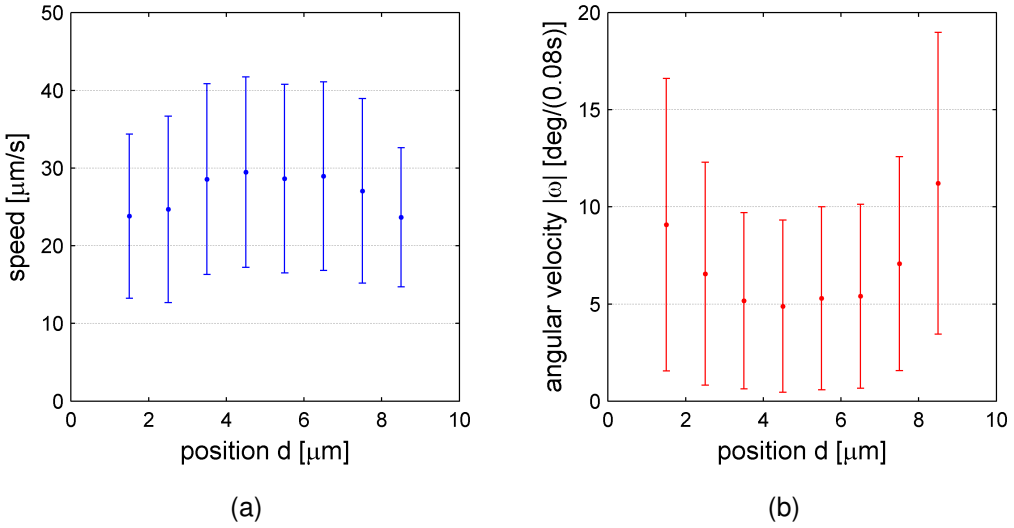

Fig. 5.25: Speed and absolute angular velocity of cells swimming parallel to the solid boundaries (pitch angle $\theta < 5$ degrees) as a function of the position in the microchannel. (a) In the center of the microchannel ($d = 5\ \mu$m) cells swim at $v \approx 30\ \mu$m/s. Near the boundaries ($d = 2\ \mu$m, $d = 8\ \mu$m) the speed decreases down to $25\ \mu$m/s. (b) Average angular velocity near the surface is two times higher than in the centre of the microchannel.

The results for the speed dependence are qualitatively consistent with figure 5.15(c) (blue curve) in section 5.2.2. In the presence of a single boundary, the average speed is highest at a distance $d = 4\ \mu$m. With figure 5.25 (a) showing data in a confinement, we can imagine the graph as a superposition of two single boundary curves like the one in figure 5.15(c), one peaked around $d = 3\ \mu$m and the other one around $d = 7\ \mu$m. Superposition of these two curves then leads to the observed speed maximum in the centre of the microchannel at $d \approx 5\ \mu$m, five micrometers away from each boundary. Analogously, the increase in angular velocity by interaction with a single wall, as shown in figure 5.15(d) (orange curve), is highest at $d = 1\ \mu$m and rapidly decays to less than 5% increase at $d = 5\ \mu$m. Superposition of two such curves with peaks at $d = 1\ \mu$m and $d = 9\ \mu$m qualitatively reproduces the angular velocity in the presence of a two boundary confinement (figure 5.25(b)).

Apart from speed and angular velocity, we also investigated how the pitch angle $\theta \in [-90°, 90°]$, the orientation of the cell with respect to the xy-plane, is affected by the position of the cell between the two boundaries (see figure 5.26(a) for definition). In figure 5.26(b), we display the average pitch angle as a function of the swimming height. Near the lower boundary, the average pitch angle is negative ($\theta < 0$), the direction of propagation for the majority of cells points towards the boundary. Near the upper boundary, the average pitch angle changes sign ($\theta > 0$), on average the cell trajectories are pointing towards the upper channel wall.

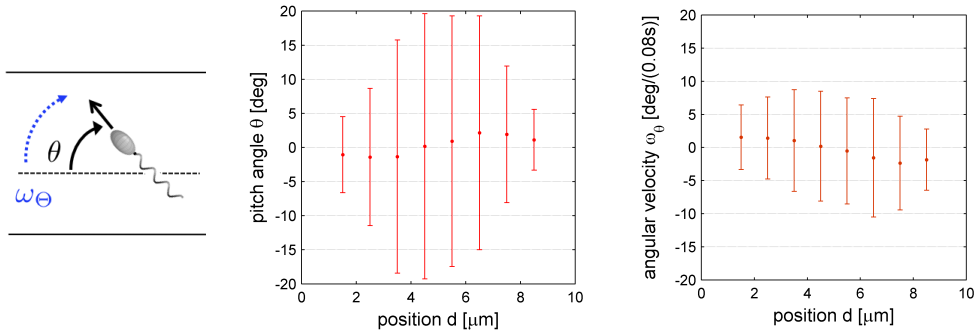

Fig. 5.26: (a) Definition of pitch angle θ and pitch angular velocity $\omega_\theta = d\theta/dt$. (b) Mean pitch angle as function of position in the microchannel. The majority of cells near the lower boundary point towards the lower boundary ($\theta < 0$ degree) while the majority of cells near the upper boundary point towards the upper boundary ($\theta > 0$ degree). In the center, on average cells are oriented parallel to the two boundaries. In both plots, the error is highest for the average value in the center (see text). (c) Mean value for pitch angular velocity (change in pitch angle) as a function of d. Near the lower boundary, the average value is positive, the cell experiences a rotation to point its head upward, while near the upper boundary, this value changes sign, the cell experiences a rotation to point its head down. In both cases, the angular acceleration reorients the cell towards the center of the microchannel to align the movement of the swimming cell parallel to the wall.

In the center of the microchannel, cells are oriented in both directions, swimming towards the upper and the lower boundary as indicated by the high standard deviation at $d = 5$ μm, while the average θ is zero (parallel). The right plot, figure 5.26(c) shows the change in the pitch angle $\omega_\theta = d\theta/dt$, the average rotation of the cell around its lateral axis, which we denote as pitch angular velocity, as a function of the position in the microchannel. Near the lower boundary ω_θ is positive. Inciding at small negative pitch angles, as seen in the neighboring plot, the cell experiences an upward rotation to

align its swimming direction parallel to the surface. Similarly, near the upper boundary ω_θ becomes negative. Cells approaching the boundary at a positive pitch angle rotate downward to align with the wall. These results are in agreement with theoretical prediction presented in section 3.3.3 if we assume that the cell is swimming as a 'pusher' with a bundle of flagella generating thrust from behind the cell body. In this case, the cell can be modeled as a positive force dipole. A cell pointing with its head towards the boundary ($\theta > 0$ near the upper and $\theta < 0$ near the lower boundary) pushes fluid against the wall (see also figure 3.12(a)). The counterforce induces a rotation or pitch moment away from the boundary pointing towards the center of the microchannel. Approaching cells are aligned parallel to the two confining walls.

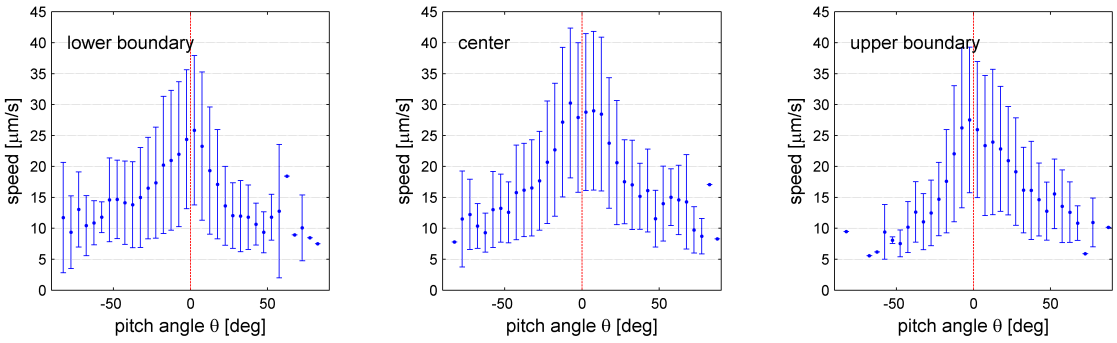

Fig. 5.27: Average speed of cells as a function of their orientation with respect to the two boundaries (pitch angle θ). From (a) to (c) plots show the population of cells close to the lower boundary ($d < 4$ μm), in the center (4 μm $< d < 6$ μ m) and close to the upper boundary ($d > 6$ μm) of the microchannel. In all regions, cells swimming parallel to the surface (θ=0 degree) have the highest speed. Near the lower boundary/upper boundary, cells pointing towards the surface with a small angle ($\theta \approx \mp 20$ degree) move faster than cells pointing away from the surface ($\theta \approx \pm 20$ degree).

We have shown that the cell speed is affected by the distance from the cell wall. In figure 5.27 we investigated whether it also depends on the pitch angle θ, the fact whether the cell is moving towards or away from the wall. For this we binned our dataset and plotted the speed as a function of θ for the population of cells close to the lower boundary, in the center and close to the upper boundary (left to right). In the center, the curve is symmetric ($v(\theta) = v(-\theta)$). Cells moving parallel to the interface are fastest, while cells swimming upward and downward with the same $|\theta|$ do this at comparable speeds. Near the lower and upper boundary, the symmetry is broken. Cells swimming towards the wall at small angles ($\theta \approx \mp 20$ degree) are faster than cells swimming away from the

wall ($\theta \approx \pm 20$ degree).

This result is contradicting the expected orientation dependent wall effect (see section 3.3.3). If the cell is swimming as a 'pusher' with a nonzero pitch angle θ, the distance d_b from the cell body to the wall is different from the distance d_l of the rotating flagellar bundle to the boundary. As explained in section 3.3.3, for $d_b > d_l$ the drag increase on the cell body is stronger, while for $d_b > d_l$ it is weaker than the increase in drag based thrust provided by the flagella. For cells swimming towards the wall d_b is smaller than d_l, and we would therefore expect a decrease in swimming speed. Instead, cells swimming in the vicinity of the surface and propagating towards the channel walls are moving faster.

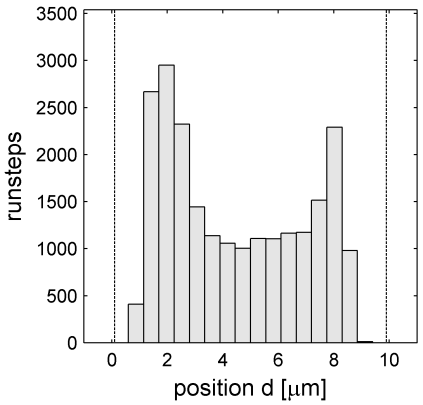

Fig. 5.28: Probability density of cells as a function of the position in the microchannel. Cells in the closed system (microchannel) spend most of their time swimming close to the upper or lower boundary (peak at $d \approx 2$ μm and $d \approx 8$ μm). The second peak at the liquid-PDMS interface ($d = 8$ μm) is less pronounced than the one near the liquid-glass interface ($d = 2$ μm).

Speed and orientation dependent pitch behavior as a function of the distance to the boundary might contribute to the overall density distribution of moving cells within the microchannel. In figure 5.28 we plot the number of individual velocity steps which were tracked over the duration of the experiment versus the position in the microchannel. Two peaks at $d = 2.5$ μm and $d = 7.5$ μm can be observed. Cells spend most of their time swimming close to the upper or lower boundary while probability density is lowest in the middle of the channel. The peak corresponding to the vicinity of the liquid-coverglass interface is larger than the one near the liquid-PDMS interface. To us, the reason for this asymmetry is unclear. In experiments performed by Li et al. [92] the probability density of swimming *C. crescentus* 'sandwiched' between two glass coverslips was strictly symmetric. Cells equally accumulated near the upper and lower glass side.

We therefore conjecture that below distances of $d < 1$ μm, a different electrostatic interaction of the cell with the PDMS-surface and glass-surface leads to the observed asymmetry. Cells are repelled stronger by the PDMS-boundary and prefer to swim parallel and in close proximity to the glass-interface (also see the discussion at the end of this chapter).

5.2.4 Discussion

Comparison with motility in the bulk fluid

The motility statistics of cells swimming in a confined environment between two solid boundaries differ significantly from the measured quantities for cells in the bulk fluid. In table 5.1, the most important parameters calculated from both datasets are listed for comparision. On average, cells in the confinement swim about 50% faster than the cells in the bulk. As one would expect from theoretical predictions (see section 3.4, in particular equation 3.29) this should go hand in hand with a more than 100% increase in the translational effective diffusion coefficient. In fact the increase is only moderate ($D = 292$ μm^2/s for the confinement as compared to $D = 218$ μm^2/s for the bulk fluid). Although the speed increases from which we would expect an increase in the mean square displacement, parts of this are counterbalanced by a drastic increase in rotational diffusion ($D_R = 0.280$ rad^2/s in confinement, $D_R = 0.073$ rad^2/s in the bulk fluid) corresponding to a higher number of curved trajectories in the confinement rather than straight trajectories with a higher net displacement, which dominate the population in the bulk. Additionally the turn behavior is affected by the presence of boundaries. More than 90% of all turning events are now reversals as compared to 60% in the bulk fluid. The average runtime as well as the directional persistence measured by the directional autocorrelation decreases in the confinement as compared to free-swimming cells.

In conclusion, cells in the confinement move faster and more often reverse their direction than cells in the bulk fluid. Their trajectories are curved and have a shorter average runtime than the rather straight trajectories in the bulk.

Speed and curvature near a single open boundary

In section 5.2.2 we measured the average speed and angular velocity of cells as a function of the distance to an open boundary, which was formed by the glass coverslip

description	parameter	bulk fluid	confinement
average velocity	v [μm/s]	26.9	37.8
reversal frequency	n_{ψ_1}/n_ψ	≈ 0.6	≈ 0.9
linear MSD fit	D [μm^2/s]	227	292
linear MSAD fit	D_R [rad^2/s]	0.073	0.280
average runtime	τ [s]	1.12	1.00
exponential DACF fit	z [s]	0.78	0.45

Table 5.1: Comparision of parameters calculated from cell trajectories in the bulk fluid and in the 10 μm microchannel. The value n_{ψ_1}/n_ψ is the ratio between the number of reversals ($\psi_i > 150°$) and the total number of all turning events in the corresponding dataset.

at the bottom of the microchannel. The swimming height of each cell or its distance d to the surface was determined from the sharpness of the cell body. Because swimming speed and angular velocity also depend on the orientation of the cell with respect to the wall, i.e. whether the cell is swimming with its head pointing towards or away from the boundary [86], we restricted our analysis to cells swimming parallel to the surface. We found that below a distance $d = 5$ μm, the average speed increases and reaches a maximum at $d = 3 \pm 1$ μm where cells swim on average 15 % faster as compared to free-swimming cells in the bulk fluid. For shorter distances $d < 3$ μm, the speed decreases down to a minimum for $d \approx 0 - 1$ μm. At this smallest distance, which can be resolved by our method, cells swim 10% slower as compared to the bulk fluid. The average angular velocity starts to increase at distances $d < 5$ μm and reaches a peak at $d = 1 \pm 1$ μm where it is around 90% higher than in the bulk fluid.

The increase in speed near a solid boundary indicates that at the observed distance the increase in thrust generated by the flagellar bundle exceeds the increase in hydrodynamic drag. This can be explained by qualitative predictions from section 3.3.3 if we assume that near a wall the flagellar bundle rotates with the same frequency as in the bulk fluid. Near a wall the translational viscous drag experienced by the cell increases. The forward thrust produced by the flagella, however, is also drag dependent. With a constant rotation rate the propulsion power increases and may overcompensate the increase in hydrodynamic resistance. For very short distances below the average cell body size ($d < 1$ μm) the drag increase on the cell body dominates. The average cell speed decreases.

The increase in angular velocity can be explained by an asymmetry in rotational drag experienced by cell body and flagellar bundle as the cell approaches the boundary ([85], see also section 3.3.3). Because cell body and flagella are rotating in opposing

directions, a torque is induced which leads the cell to describe a constant right- or left-turn. The average angular velocity in these curved trajectories increases as compared to cells swimming in straight runs in the bulk fluid.

Several experimental studies have reported on curved trajectories of bacterial swimmers and of eukaryotic sperm cells in close proximity to a solid boundary [10, 50, 82, 102]. To the knowledge of the author, however, no experimental studies are available that systematically investigated the swimming speed of a microorganism as a function of the distance to a solid boundary. For the monoflagellated bacterium *V. algynolyticus* an increase in swimming speed around 47 % as compared to the bulk fluid was observed for a cell population swimming within a ten micrometer thick layer above the surface [110]. This increase however was restricted to runs attributed to the backward swimming mode of the cell, where it is swimming as a 'puller'. No wall induced effect on the swimming speed was observed in the forward swimming mode of the bacterium.

In a theoretical study by Ramia et al. numerical simulations based on resistive force theory (see section 3.3.2) were used to model the swimming of a bacterium with spherical cell body and a single flagellum near a plane boundary [123]. They found a 10% increase in speed for cells swimming parallel to the surface at a distance on the order of the flagellar radius $d \approx 50$ nm stating that at this distance 'the flagellar propulsive advantage...is offset by an equally significant increase in the cell body drag' [123]. For distances above one micrometer, no increase in speed was reported. The simulations are thus unable to explain the observed speed increase at a distance of three microns. Analytical solutions from resistive force theory were compared with experimental data of *E. coli* with varying cell body size swimming close to the boundary [84]. While the exact swimming height could not be determined in this study, the authors present analytical solutions for the swimming speed as a function of the cell body radius for two distances, 10 nm and 60 nm. No significant difference in swimming speed between the two distances could be observed. However, results from the model show that the swimming speed strongly depends on the cell body size. Cells with a body radius $r = 0.8$ μm in close proximity to the boundary are predicted to swim 35 % faster than cells with $r = 1.2$ μm, again presuming constant rotation rate of the flagellar motor.

Apart from resistive force theory, bacterial swimming near boundaries at distances larger than the cell size was described by a multipole expansion [137]. The flow induced by a bacterium swimming as a 'pusher' is modeled by a linear combination of fundamental solutions to the Stokes equation, starting with a positive force dipol at the highest order. The presence of the boundary is accounted for by mirror singularities inside the wall to satisfy the no-slip boundary condition at the surface. For a cell swim-

ming parallel to the surface, no increase in swimming speed is predicted. An increase in swimming speed can be anticipated only if the cell is swimming with its head pointing away from the boundary. However, at a distance six times the cell body radius, which corresponds to the observed peak in our experiments, in the model a pitch angle on the order of 45 degrees would be necessary to explain the magnitude of the observed speed increase around 15%. We can definitely rule out the possibility that our calculated average speed values include cells swimming at such high angles with respect to the boundary.

Neither resistive force theory based upon the increase in local drag on body and flagellum nor far field approximations using a multipole expansion to describe the hydrodynamic interactions between bacterium and boundary are thus able to explain the increase in swimming speed at the observed distance and we can only speculate about its origin. A possible assumption is that flagella start to rotate faster if they experience higher drag. To verify this, we suggest an experiment where swimming speed and rotational frequency of the flagellar bundle near a boundary are measured simultaneously e.g. by laser illuminated dark field microscopy similar to a study performed by Magariyama et al. [104].

Three-dimensional motility measurements

High speed Z-Scans in combination with an appropriate reconstruction algorithm allowed us to acquire three dimensional trajectories of cells with a high temporal and spatial resolution. We performed experiments with cells swimming in a microchannel measuring 10 μm in height. The distribution of turning angles shows a peak at 165 degrees. This is consistent with our previous results if we consider that in section 5.1 and section 5.2 the angle between two subsequent runs was in fact calculated from the two-dimensional projection of a three-dimensional trajectory. Trajectories acquired from three-dimensional time lapse recordings display a run-reverse swimming pattern with alternating propagation speeds which is consistent with our observations from two-dimensional motility statistics.

The results on average speed and angular velocity as a function of the position in between the two boundaries of the channel are consistent with the motility statistics in the presence of a single boundary (section 5.2.2). Near a single boundary, we measured a maximum in average speed at a distance $d = 4$ μm and a decrease for smaller distances. With a superposition of two single boundary curves, one with a peak at $d = 4$ μm the other one with a peak at $d = 6$ μm, we recover the observed maximum in

average speed in the center of the channel between the two boundaries at a distance $d = 5\ \mu$m. Analogously, a superposition of two curves describing the angular velocity in the presence of a single boundary can reproduce the observed minimum in the center and the observed maximum in closest proximity to the boundaries calculated from the three dimensional trajectories.

With the full three dimensional picture of swimming dynamics available, we were able to analyze how the orientation of the cell is affected by the two boundaries. We found that near the upper and lower boundary, below a distance of three micrometers, cells pointing towards the channel walls experienced a rotation to align themselves parallel to the boundary. If we assume that a majority of cells are swimming as a 'pusher', a possible explanation for this result can be given by the hydrodynamic interaction of the flow field generated by the bacterium with the solid boundary [137]. The flow around a 'pusher' can be approximated in the leading order by a positive force dipole. If a cell is swimming with its heads pointing towards the boundary, it pushes fluid against the wall. The corresponding counterforce then induces a rotation away from the boundary. However, if this hydrodynamic interaction were to dominate the swimming dynamics we would expect that in a steady-state situation, the majority of cells would swim parallel to the upper and lower boundary. This is clearly not the case in our experiment as can be seen from figure 5.26. While hydrodynamic interactions reduce the inciding angle at which a cell is approaching the boundary, they do not prevent collisions with the channel wall. The influence of collisions and rotational diffusion in the vicinity of a boundary have to be taken into account.

We also analyzed how the average swimming speed depended on the orientation of the cell in the microchannel. Results from the multipole expansion in [137] would predict that cells pointing towards the boundary move slower, while cells pointing away from the boundary move faster as compared to parallel swimmers because of far field interactions of the flow field with the boundary (see the previous subsection). Additionally, for a cell swimming in a 'pusher' configuration the flagellar bundle is moving closer to the boundary than the head of the cell. At distances on the order of the cell body size, the increase in drag based thrust produced by the flagella is then higher than the drag increase on the cell body, the cell is expected to move faster than a parallel oriented cell swimming at a comparable distance to the boundary. Unexpectedly we found that cells pointing towards the boundary swim slightly faster than cells which were pointing with their head towards the center of the microchannel. Currently, we cannot explain this observation. A closer analysis of individual trajectories from three-dimensional tracking however revealed that the direction in which a cell is swimming is not always aligned with the principal axis of the cell body. The presented theoretical models do

not account for such a 'drift' swimmer and corresponding deviations in the flow field generated by the cell. The positive force dipole is always aligned with the cells principal axis [86, 123, 137]. Additional experiments are required to systematically investigate differences in cell body orientation and swimming direction which are caused by wall effects.

Our analysis of the probability density of cells revealed that cells spend most of their time swimming close to the upper or lower boundary of the microchannel. At first hand this can be explained by hydrodynamic interactions. Cells swimming in a 'pusher' mode experience a wall induced attraction [13]. If hydrodynamic forces were the dominating factor, however, cells would equally accumulate near the upper and lower boundary. This is not the case in our experiment where we observe a stronger peak at the liquid-glass interface as compared to the liquid-PDMS interface. Collisions with the surface and electrostatic interactions must play an important role. Recently, Drescher et al. directly measured the amplitude of the flow field generated by swimming *E.coli* by tracking fluorescent microspheres [42]. They found that collisions with the surface rather than hydrodynamic forces are the dominating factors governing alignment with the boundary. They claim however, that once oriented parallel to the boundary at distances within a few microns, hydrodynamic interactions stabilize the near boundary swimming state. In a recent study, where a comparable experiment was performed with *Caulobacterium crescentus*, simulations accounting for the interplay between collisions and near surface rotational diffusion only, could reproduce the steady state accumulation of swimming cells near boundaries [93, 94]. Our experimental results suggest that both collisions and hydrodynamic interactions of a 'pusher' cell with the boundary promote an accumulation of swimming *P. putida* near the solid boundaries of confined environment.

Change in swimming mode upon reversal

As discussed in the bulk fluid section 5.1.3, it is unclear how the multiple, polar flagella of *P. putida* reorient during a reversal. Because no rotation in the cell body could be observed, we concluded that a reversal must be accompanied by one out of three possible changes in the swimming mode which we depicted in figure 5.8(b)-(d). This is also supported by the systematic difference in swimming speed by a factor of around two, which was observed in all three different experimental settings, in the bulk fluid, for cells swimming in between two solid boundaries and near a single open boundary.

As explained in section 3.3.3 and confirmed by measurements in section 5.2.2, below

a threshold distance, interaction with a solid boundary induces a torque on a swimming bacterium which leads the cell to describe a curved trajectory. The sign of the curvature, i.e. whether the cell performs a right turn or a left turn depends on the direction (CCW or CW) in which cell body and flagellar bundle are rotating. For a constant distance to the boundary we expect the magnitude of the curvature to depend on how the flagellar bundle is arranged with respect to the cell body. Since all possible transitions in swimming mode upon a reversal are accompanied by a change in the direction of rotation or in the location of the flagellar bundle our hypothesis, essentially summarized in figure 5.17, was that by analyzing the change in curvature upon a reversal for cells swimming close to the surface we could discriminate between the three transitions. This approach was supported by experiments on the swimming behavior of the monoflagellated marine bacterium *V. alginolyticus* [102]. There it was found that near a surface alternating periods of forward and backward swimming are accompanied by alternating straight and curved run segments in the corresponding trajectory.

Our analysis of the average curvature of two subsequent runs near a surface did not reveal a systematic change in the sign of the curvature (from right-curved to left-curved and vice versa) as it would be expected for a cell constantly switching between 'pusher' and 'puller' mode upon reversal. With approximately equal probability the cell continues with a left-curved or right-curved trajectory upon a reversal. Together with our considerations from section 5.1.3 on the low stability of a pulling flagellar bundle which is supported by several studies [100, 101] we therefore conclude that a reversal is not initiated by a transition from a 'pusher' to a 'puller' swimming mode.

Instead we propose that, to enter and leave a reversal as a 'pusher' without rotating the cell body, *P. putida* flips the direction of the flagellar filaments to the other side of the cell body. A cell then emerges from a reversal with the side of the cell body, where the flagellar motors are located, at the front, while its filaments are pointing backwards, away from the new direction of propagation. Because our results showed no systematic changes in the sign of the curvature between subsequent runs, we assume that this reorientation of filaments is initiated by a reversal of the motors from CCW to CW rotation (figure 5.17(c)) instead of an unlikely spontaneous 'flipping' of filaments (figure 5.17(b)). Because of a shorter distance between rotating filaments and body in this alternative pusher mode 5.29(B), we expected a smaller magnitude in the wall induced curvature of the corresponding run. This is consistent with the fact that in our experiments, though not in a systematic fashion, we observed a change in the curvature magnitude upon a reversal.

The probability density of cells as a function of the channel height which was determined

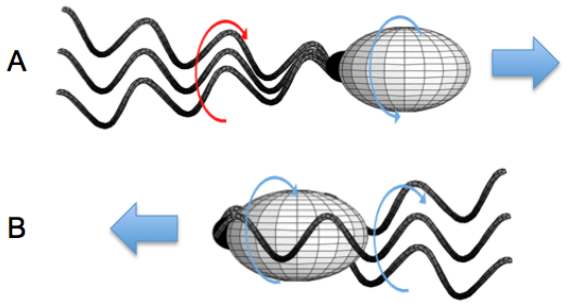

Fig. 5.29: Conjecture for the reorientation of flagellar filaments during a reversal event in *Pseudomonas putida*. Before (A) and after the reversal (B), the cell is swimming as a 'pusher'. While before the reversal, flagella are rotating in CCW- (red arc arrow) and the cell body is rotating in CW-direction (blue arc arrow), after the reversal flagella and cell body are both rotating in CW-direction. In both cases (A) and (B), the trajectory of the cell will perform a right turn when swimming close to a solid boundary.

from three-dimensional trajectories in section 5.2.3 may support our assumption that *P. putida* is predominantly swimming as 'pusher'. We found that cells accumulated near the upper and lower boundary of the channel, while the cell density was lowest in the center between the two walls. Provided that hydrodynamic interactions play an important role, such an attraction of cells to a solid boundary can be attributed to cells swimming in a 'pusher' mode, while cells swimming in a 'puller' mode are expected to be repelled from the boundary [13, 86]. Furthermore, in section 5.2.2 all five datasets of cell trajectories in the vicinity of a single boundary showed a negative average value in the angular velocity corresponding to a majority of cells preferentially turning to the right. This additionally supports our 'push-flip' scenario presented in figure 5.17(c), where a right-curved trajectory is expected before and after the reversal.

5.3 Surface related growth in linear channels

In the previous sections we have analyzed the swimming pattern of *P. putida* in the bulk fluid and in a confined microchannel. The present chapter will focus on a different aspect of the same experiment, again performed according to the protocol described in section 4.4.1, the growth dynamics of swimming cells and immobile cells in colonies at the surface of the channel. While cells after five hours swim with an average speed of $35\ \mu$m/s, colonies at the surface grow by cell division on a much longer timescale, with an increase in colony diameter around $2\ \mu$m/h. We are thus looking at a process, which proceeds in the same experiment only much slower at a longer timescale.

5.3.1 Number growth and colony formation

After the diluted suspension of cells was filled into the microchannel, the initial population of cells immediately attached to the surface and started to grow by division forming colonies of increasing size. At the same time, swimming cells coexisted with the sessile cells, moving in between the colonies and temporarily attaching and detaching from the surface. We counted the number of sessile and swimming cells every 30 min. While the number of swimming cells at a given time was directly accessible from the tracking algorithm, the number of sessile cells was estimated by dividing the surface area coverage by the average size of a single cell determined from the data of individual swimmers. The results are shown in figure 5.30 starting after a development time of 3 hours. During the first 3 hours, the number of swimming and sessile cells remained constant. As can be seen in the left plot, after 3 hours the density of sessile cells during three comparable experiments increased exponentially. From a fit we estimated a doubling time between 1.5 to 2 hours. This is much slower than $t_d = 38$ min for cells growing in a shaking culture. The growth curve for the swimming cells (center panel) remains flat during the first five hours, the number fluctuates around $10 - 40$ cells. Approximately after 5.5 hours, we observe a sudden jump, the number of swimming cells increases by more than one order of magnitude. The right plot shows that, while at the beginning of the experiment only a minority of cells are motile, an equal number of cells in the microchannel are now in the swimming and in the sessile phase. Beyond 6.5 hours, the channel became crowded and we could no longer identify individual cells. The characteristic jump in the number of swimming cells occurred at three comparable experiments, each time with a different initial density of sessile cells on the surface (see figure 5.30(a) at $3:00$ h).

In figure 5.31 we display the evolution of the colony size as a function of time. After three

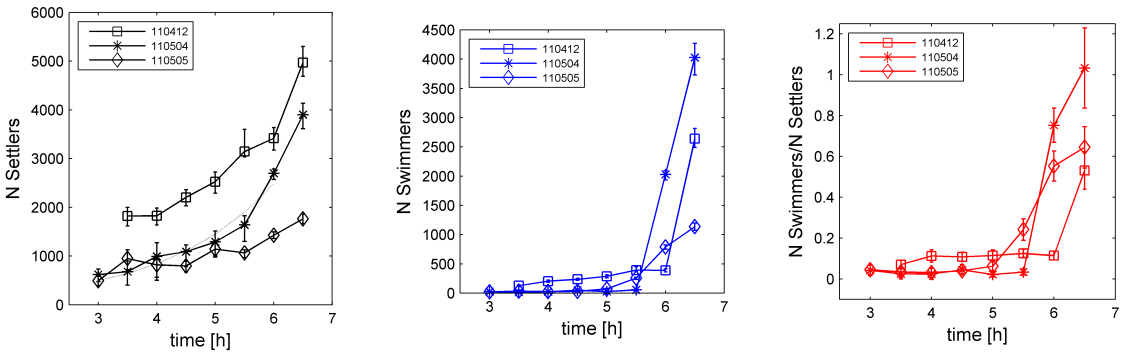

(a) (b) (c)

Fig. 5.30: Number of swimming and sessile cells in microchannel with 20 μm height for three comparable experiments starting after a development time of 3 hours. (a) Sessile cells grow continuously in colonies with a doubling time around 1.5 hours. (b) The number of swimming cells fluctuates between $10 - 50$ cells during the first five hours. At $5:00 - 5:30$ h, the number increases by two orders of magnitude, accompanied by the dissolving of bigger cell colonies on the surface (see figure 5.31)).(c) Ratio between swimming and sessile cells over time. During the first three hours the number of swimming and sessile cells was constant. No growth could be observed.

hours of surface growth the distribution shows a peak around 7 μm^2, single isolated cells with an average area of $\approx$ 3 μm^2 have divided at least once. These colonies grow further, which is reflected by the peak in the distribution being shifted to the right. Approximately 5.5 h after the beginning of the experiment, the average colony size has reached a maximum with $\bar{s} = 28.9$ μm^2. During the following 60 minutes (center and right plot), big colonies first continue to grow and then dissolve with the majority of their cells detaching from the surface at $6:00$ h. At the same time, a huge number of individual cells from the bulk fluid newly attach to the surface and join the remaining residues of the colonies. Note that while the average cluster size has decreased, the overall number of sessile cells, the cell density on the surface has increased continuously.

In the following we investigate the cause of the sudden transition of cells into the swimming phase and the breakup of clusters, constantly occurring after five to six hours of growth within the microchannel. The transition could be triggered by: (1) quorum sensing or mechano-sensing after either the density of cells on the surface or the size of the individual colonies exceeds a threshold, (2) a depletion or change in the properties of the growth medium, or (3) the contact time or ‚age' of a cell, in other words the time it has spend on the surface after its initial attachment.

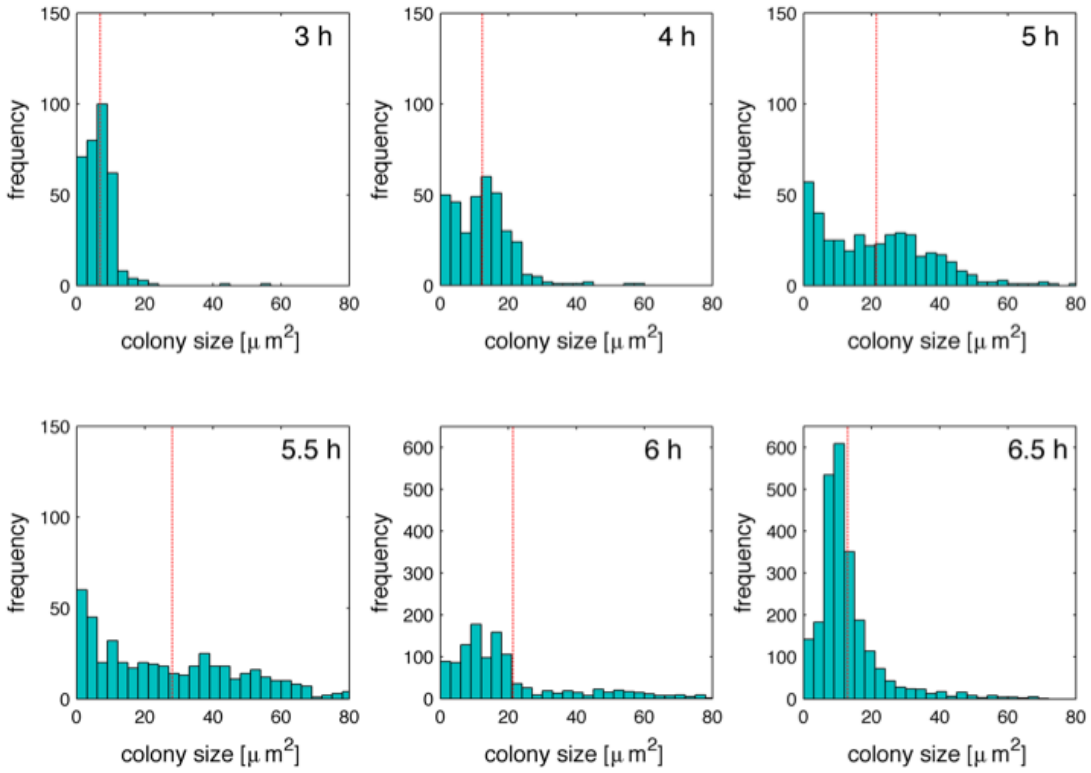

Fig. 5.31: Distribution of colony sizes for different times (from left to right) after the beginning of the experiment. After three hours, isolated, individual clusters consisting of one up to three cells dominate (left plot, peak at $\approx 7\ \mu$m^2). Over time, the average colony size increases (red vertical line). After five hours, the bigger clusters have reached a size around $\approx 25\ \mu$m^2, containing more than eight cells. After 5.5 hours, the average colony size reaches its maximum with $\bar{s} = 28.9\ \mu$m^2. During the following 30 minutes, bigger colonies start to dissolve and the average cluster size decreases. After 6.5 hours, the residues of the bigger colonies together with individual cells attaching from the bulk fluid form the peak at $\approx 7 - 10\ \mu$m^2.

5.3.2 Renewing growth medium

To check the influence of depletion of nutrients in the growth medium we performed a comparative experiment, inoculating the surface of our microchannel with the same density of cells as in the experiment described in the previous section. This time, one inlet of the channel was connected via tubing with an infusion pump, that would run a shringe (Hamilton 1750 TLLX, Hamilton (Bonaduz, Switzerland)), filled with growth medium (N-Medium). Throughout the experiment we then ran a flow with $\bar{u} = 650\ \mu$m/s for a period of three minutes every 30 minutes as indicated by the red vertical lines in figure 5.32. The growth medium of the cells in the channel was thus renewed every 30 minutes and the time and flow speed were adjusted such that in every ‚flush'

(i) all swimming cells were removed from the microchannel and (ii) the colonies were unaffected and not removed by the shear forces induced by the flow .

We repeated the count of swimmers and sessile cells at the end of every 30 minutes period, right before starting the flow, following the same procedures like in section 5.3.1. The results are shown in figure 5.32. While the number of sessile cells grows continuously with a slightly higher average doubling time (1.0 to 1.5 hours), we recover the same jump in the number of swimming cells after 5.5 hours of development. Since swimmers are now removed by the flow every 30 minutes, we know that all cells counted as swimmers must originate from cells that have detached from the surface colonies or from growth within the past 30 minutes.

In summary, we can rule out the possibility (2), see above, that the sudden transition of cells from the sessile to the swimming phase is caused by medium depletion only, because periodic renewal of growth medium using microfluidics reproduces the same jump in the number of swimmers after a comparable development time.

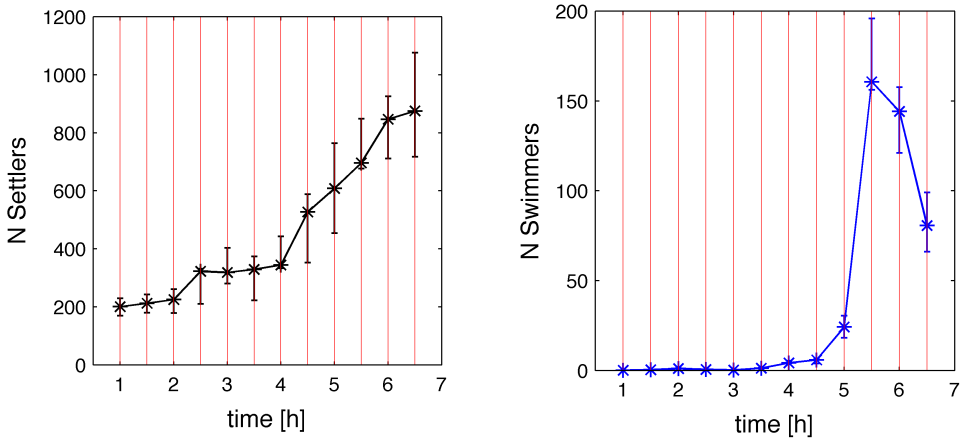

(a) (b)

Fig. 5.32: Number of sessile and swimming cells in microchannel with 20 μm height. The growth medium is renewed by flow every 30 minutes (vertical red lines). (a) Sessile cells grow continuously but slightly faster than under no flow conditions (see figure 5.30(a)). (b) The jump in the number of swimming cells detaching from the colonies occurs after 5.5 hours at a time comparable to the results from the experiment without flow.

5.3.3 Populations with different contact time

The experiment in the previous section pointed towards a transition from the sessile to the motile lifestyle which occurs after a certain contact time with the surface or when the size of the growing colonies exceeds a certain treshold (possibility (1) and (3), see above). To investigate these two aspects further, a second complementary experiment was performed, where we made specific use of the advantages provided by microfluidic techniques in the study of cell growth and motility. We designed a microchannel with a Y-shaped geometry consisting of two inlets which are connected to smaller channels (300 μm width). The channels merge together into a bigger main channel (500 μm width) with an outlet for fluid dispersal at its end. Two syringes were connected via tubings to the channel inlets, one filled with buffer and the other one filled with a cell suspension of a density around 10^7 mL^{-1}, the same density that was applied for the inocculation of the surface in the previous experiments (see section 5.1). During the first three hours of the experiment an equal pressure gradient was applied via infusion pumps on both syringes that created two separated flow streams at the crossection of the Y-junction (see figure 5.33), one consisting of buffer (region II), the other one consisting of cell suspension (region I). The idea was to first colonize only a limited area of the microchannel (region I). The continuous buffer flow would remove swimming cells that could diffuse into region II and provide only the cells in the lower half with growth medium. By switching off the flow at the point where cell density and colony size in region I are approaching the level that precedes the transition into the swimming phase observed in section 5.3, we would then observe initially sessile cells from region I exploring region II during the second half of the experiment. The aim was to compare the growth dynamics of this younger offspring population with our previous results from section 5.3.1 and with the mother population of cells in region I.

During the first half of the experiment under flow conditions, cells continuously attached to the surface area that was covered by the flow of cell suspension and started to grow by division forming tightly packed colonies with increasing number density (see figure 5.34(a) and figure 5.33 at 58 and 133 min for comparision) while the number of cells in region II remained close to zero (see figure 5.34(b)) as intended. After 160 minutes the flow was switched off (indicated by red vertical line in figure 5.34). Colonies in region I consisted of more than eight cells and had grown to sizes near the maximum before the recorded transition in section 5.3. No swimming or otherwise motile cells were observed in the region of interest. In the following, while colony growth in region I proceeded, cells detached from the aggregates and started to swim and diffuse towards region II. Exploration of cells into this area was followed by irreversible attachment and

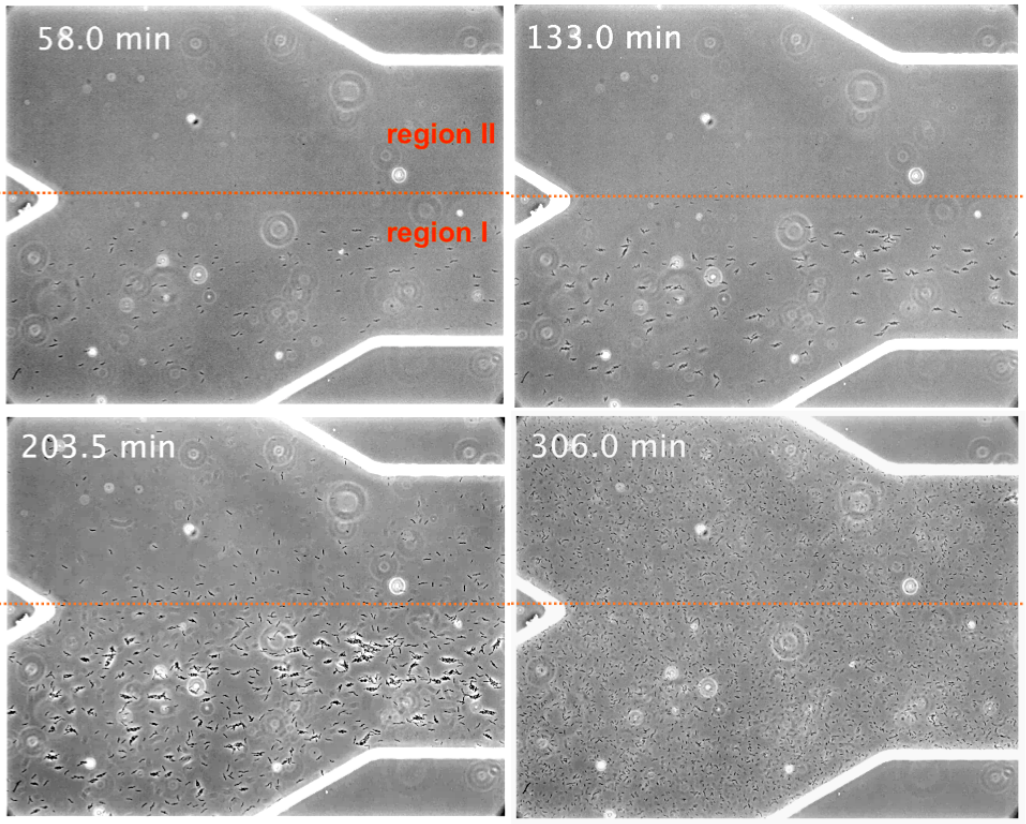

Fig. 5.33: Colony growth and breakup in Y-junction microchannel: During the first half of the experiment (upper left and upper right) a constant flow of buffer (region II) and cell suspension (region I) merges at the intersection. In the lower half, cells attach to the surface and form colonies while the upper half is kept free of microorganisms. After 160 min, the flow is switched off (lower left and lower right). Cells from region I explore into region II. Synchronous breakup of newly grown smaller colonies in region II and bigger older colonies in region I occurs at 230 min. After five hours, the channel is homogenously covered by swimming cells and isolated sessile cells on the surface. The ROI lies at the crossection of the two channel branches (see also figure 4.6 for the channel geometry).

the surface cell density in region II increased. The offspring population started to grow by division in newly formed colonies (see figure 5.33 at 203.5 min).

Approximately four hours after the beginning of the experiment and after 80 minutes under no flow conditions, the new colonies in region II started to break up and the number of swimming cells increased suddenly (blue vertical line in figure 5.34(b)). At the time of the breakup, initially isolated cells in region II had divided no more than three times and had grown to only half the average cluster size that was monitored in the previous experiments before cell dispersal. Synchronously, the older and bigger

clusters in region I started to dissolve and release swimming cells to the surrounding fluid at the exact same time. After more than 230 minutes, cluster size as well as number density of cells on the surface continued to decrease in both regions while the number of swimming cells quickly equilibrated to a homogenous density across the channel. Reattachment and recolonization, now with a new population of individual cells joining the remains of the colonies at the surface again started to occur synchronously in both regions five hours after the beginning of the experiment.

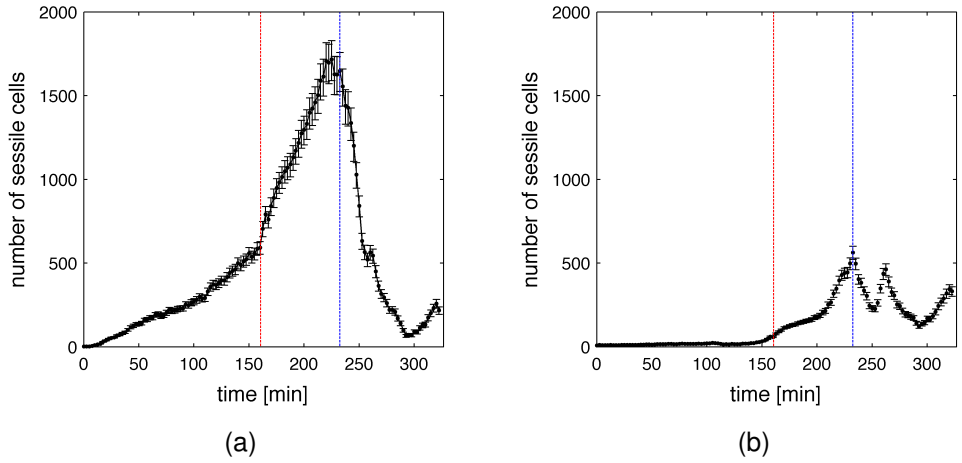

Fig. 5.34: Number of sessile cells in region I (a) and region II (b) during the Y-junction experiment as a function of time. While the number of cells in region II, which is covered by a constant flow of buffer, is close to zero, cells in region I subjected to a constant medium flow grow continuously in colonies. At 160 min (red vertical line) the flow is switched off, allowing colonization of region II by cells from region I. Cell density continues to increase in both areas. At 230 min, surface density decreases accompanied by a synchronous colony break up in both regions. Above five hours, individual cells reattach to the surface in both regions.

5.3.4 Discussion

We used time-lapse microscopy to monitor the number of swimming and sessile cells during the early development towards biofilm formation in the medium-rich environment of a microchannel. Because of the hydrophobic nature of the cell membrane [150], at the beginning of the experiment the majority of cells immediately attached to the solid-liquid interface of the glass coverslip sealing the microchannel from below. Few swimming cells were populating the channel. The first generation of cells, referred to as 'primary' biofilm cells, experienced a surface associated delay time or lag time of $3:30$

hours before they started to grow by binary fission. This is usually attributed to genetic changes which occur during the transition from the planktonic to the sessile phenotype of the bacterium [126]. Genes encoding flagellar synthesis are downregulated while the synthesis of adhesive proteins and the production for the secretion of other extracellular substances is upregulated [35, 36]. In general, growth of cells in surface associated colonies was significantly reduced with an average doubling time $t_d \approx 1.7$ hours as compared to growth in the bulk liquid of a shaking culture with a doubling time around 0.8 hours (see section 4.2) . Note that experimental findings have reported both increasing or decreasing growth rates of bacteria attached to a surface, varying from species to species, sometimes even with opposite effects on the same microorganism depending on the nature of the growth substrate [135]. Here one has to distinguish between the changes in the physical and chemical environment around a cell on the surface and the physiological changes due to adaption to the sessile lifestyle. While diffusive uptake of oxygen, carbon or other substrates by the cell (which is modeled as a half sphere) is reduced as compared to the bulk case, a change in the phenotype can increase metabolic activity of the cell, accelerate substrate utilization kinetics [135] and promote cell growth on the surface. Within the observation period of our experiment, the negative effects on the growth kinetics dominated.

In three comparable experiments we observed a sudden jump in the number of swimming cells accompanied by a breakup of all bigger surface attached colonies, containing 8 to 16 cells (three to four generations), approximately 5.5 hours after the beginning of the experiment.

Subsequently the crowded microchannel was dominated by a population of swimming cells which after 60 minutes reattached to the surface as individual cells. The observed transition can be interpreted as an emigration and recolonization event, where biofilm capable cells first grow to defined sizes after which flagella synthesis is renewed and daughter cells are emitted to swim and explore towards new growth environments. A similar process has been reported for *Pseudomonas fluorescence* by Lawrence et al. for surface related growth under flow conditions [88].

To evaluate whether this transition is triggered by changes in the growth medium, either by a local or global depletion of the carbon source or an accumulation of signaling substances secreted by the cells (quorum sensing), we renewed the growth medium and removed all swimming cells and secreted substances from the system by periodically flushing the channel. We observed colony dispersal and cell release to the swimming phase at comparable times indicating that the transition is not induced by a global depletion of the substrate and is independent from the overall density of cells on the surface.

The latter was already suggested by the fact that the breakup occurred at the same time in three experiments with a varying initial density of cells on the surface (see figure 5.30(a)). We cannot rule out, however, the possibilty that a local depletion of substrate triggers the observed transition as proposed in [80]. In particular when colonies grow above eight cells, the local flux of oxygen and nutrients towards bacteria in the center might be impaired significantly. To keep medium growth conditions exactly constant even at a local level, we plan further experiments and developed a double-layer microfluidic device where a constant supply of medium is provided via diffusion through narrow perfusion channels which are connected to the cell chamber (see section 6).

Careful manipulation of medium and buffer flow in the Y-junction experiment allowed us to first colonize a predefined subregion of a microchannel by 'primary' biofilm cells and then monitor the growth dynamics of its 'secondary' offspring population of cells colonizing the initially uncovered areas of the channel. Suprisingly, the dissolution of colonies occured synchronously in both neighboring areas. While 'primary' biofilm cells had grown to the size observed in the previous experiments, colonies from 'secondary' cells had grown for a much shorter time and were thus much smaller. At the time of the colony break up, 'primary cell' had been in contact with the surface for 230 min as compared to a contact time of less than 80 min for the offspring population. In their experiment under continuous flow conditions, Lawrence et al. reported surface associated growth in tightly packed colonies which was followed by a global detachement of cells from the colonies after four division cycles (microcolony of 16 cells) [88]. We suggest that in *P. putida*, a bacterial species from the same family, we are looking at a similar process. While not directly depending on the contact time, the dissolution of colonies formed by the 'primary' and 'secondary' population of cells is triggered after a fixed number of generations spent in contact with the surface. Individual cells that emigrate from the primary colonies, before the global brake up of clusters is initiated, have already completed a number of generations as sessile cells and settle in the unoccupied space but detach again after two or three division cycles.

Chapter 6

Summary and Outlook

In the present work, we performed experiments with *Pseudomonas putida*, a lophotrichously flagellated soil bacterium capable of biofilm formation at solid-liquid interfaces. We used microfluidic tools together with high speed cell tracking to acquire trajectories of cells swimming in the bulk fluid, in the vicinity of a single open boundary, or confined between two solid boundaries. Additionally, we investigated the surface related growth dynamics of motile and non-motile cells.

In the bulk fluid (section 5.1), cells displayed a typical bacterial swimming pattern with periods of persistent runs interrupted by turn events. When compared to the swimming trajectories of the peritrichously flagellated bacterium *E. coli*, the most commonly studied bacterial model organism, the reorientation events of *P. putida* resemble sharp turns and are on average faster ($< 0.08\ s$) than tumbling events in *E. coli* ($\sim 0.1\ s$) [8, 34]. An analysis of the turning angle distribution revealed a strong peak at an angle around 180 degrees and a minor peak around zero degree. During a majority of the turn events, the cell virtually instantaneously reverses its swimming direction, while to a lesser extent the cell pauses and then continues to swim towards the previous direction of propagation. Additionally, we found that upon a reversal the swimming speed of the cell on average changes by a factor of two. Cells alternate between fast and slow runs. While earlier studies on *P. putida* have reported on the bimodality of the turning angle distribution [38, 44], to the knowledge of the author, this is the first time that such a systematic change in swimming speed between subsequent runs has been reported for a free-swimming bacterium.

In a joint effort with Johannes Taktikos, Vasily Zaburdaev and Holger Stark, we developed a model for a run-reverse random walker with two alternating speeds based on the experimentally determined parameters for the average runtime and rotational diffusion of cells. In its simple analytic form, where we used an exponential runtime dis-

tribution, the model yielded good agreement with the experimentally measured mean square displacement (MSD). In comparison with cells swimming at a constant intermediate speed, the MSD for a population of cells alternating between fast and slow run speeds is strongly increased. In an extend version of the model, where runtimes were approximated by a gamma distribution, we successfully reproduced the observed negative dip in the directional autocorrelation function.

A run-reverse swimming pattern has been reported for monoflagellated bacteria like *Pseudomonas citronellolis* [140] and has been typically attributed to marine bacteria like *Shewanella putrefaciens* and *Vibrio alginolyticus* [4,72]. In the case of a monotrichously flagellated bacterium a reversal is induced by a change in the rotational direction of the flagellar motor unit. The cell switches from a 'pusher' to a 'puller' swimming mode. For a lophotrichously flagellated bacterium it remains unclear how a reversal in swimming direction can be achieved without rotating the body of the cell. It has been suggested that in *P. putida* a reversal in swimming direction is caused by a synchronous reversal of the flagellar motors from CCW- to CW-direction [64]. Recent experiments have shown that the rotational directions of nearby flagellar motors can indeed synchronize [141]. It is generally assumed however, that a pulling bundle is unstable and prone to jamming [100]. Instead, we propose that in *P. putida*, to enter and leave a reversal as a 'pusher' without rotating the cell body, the cell flips the direction of the flagellar filaments to the other side of the cell body. A cell then emerges from a reversal with flagellar motors located at the front and with the filaments pointing backwards. In section 5.2.2 we analyzed the change in curvature upon a reversal for cells swimming close to a solid boundary to discriminate between the two possible transitions in swimming mode upon a reversal. Our analysis revealed no systematic change in the sign of the curvature as it would be expected for a cell switching from a 'push' to a 'puller' mode close to a surface. Additionally we find a preference for right-curved trajectories and an increased density of cells near the boundary which is both usually attributed to cells swimming in the 'pusher' configuration [13, 86]. This additionally supports our 'push-flip' scenario.

In section 5.2 we investigated possible changes in the swimming pattern in a confined environment. For this purpose, we used the local intensity gradient of the cell contour to determine the position of cells with respect to the boundary from two dimensional trajectories. In the presence of a single boundary, we observed an increase in average swimming speed of around 15 % at a distance of three micrometers to the surface when compared with free-swimming cells. Below a distance of one micrometer, the average swimming speed was approximately 10 % smaller than in the bulk fluid. The average angular velocity of the cell started to decrease for distances below five micrometers and was maximum in the closest proximity to the boundary. These observations are

consistent with our results on swimming speed and angular velocity in the presence of two solid boundaries for which we analyzed three-dimensional trajectories (section 5.2.3). The average swimming speed and angular velocity in a microchannel measuring 10 μm in height could be explained qualitatively by a superposition of two corresponding curves for speed and angular velocity in the presence of a single boundary.

Observations on the average angular velocity are in agreement with experiments on *E. coli* [84]. Near an open solid boundary, the axial symmetry of the rotational drag experienced by the cell body and by the flagellar bundle is broken. Because of the opposing rotational direction of cell body and flagella, this asymmetry induces a torque which leads a cell swimming in a 'pusher' fashion to perform a constant right turn. When imaged from above, trajectories follow a clockwise circular path. The increase in swimming speed at a distance around three micrometers to the boundary cannot be explained by existing theories. Numerical studies based on resistive force theory, where the bacterium was modeled with a spherical cell body and an single flagellum near a plane boundary, predicted a 10% increase in swimming speed but at a much smaller distances to the boundary on the order of the radius of a single flagellum ($d \approx 10$ nm) [123]. To account for hydrodynamic interactions with the boundary at distances larger than the cell size, a microswimmer has been described by a linear combination of fundamental solutions of the Stokes equation, in leading order by a positive force dipole [137]. No increase in swimming speed was predicted for a cell swimming parallel to the boundary. Neither resistive force theory nor long range hydrodynamics explain the speed increase which has been measured in our experiments using statistics from two- and three-dimensional trajectories.

Apart from speed and angular velocity our analysis of the cell density profile revealed that the majority of bacteria accumulated near the upper and lower boundary of the microchannel. For cells swimming in a 'pusher' mode this has been explained by a wall induced attraction and alignment parallel to the surface [13]. However we observed that the peak in cell density is relatively stronger near the liquid-glass interface as compared to the liquid-PDMS interface. This indicated that apart from hydrodynamic interactions, other forces like collisions with the surface and electrostatic interactions with the boundary must be considered. Recent studies have addressed the relative importance of long range hydrodynamic interactions, resistive force theory, as well as the influence of rotational diffusion and collisions on a parallel alignment of the swimming direction with the boundary and consequently on an accumulation near the boundary [42, 93, 94]. Measuring the amplitude of the flow field generated by a swimming *E. coli* they found that collisions with the surface rather than hydrodynamic forces are the dominating factors governing alignment with the boundary [42]. Notwithstanding, once oriented paral-

lel to the boundary, hydrodynamic interactions stabilize the near boundary swimming state. Recently, simulations accounting for the interplay between collisions and near surface rotational diffusion alone, were able to reproduce the steady state accumulation of swimming *Caulobacterium crescentus* bacteria near boundaries [93, 94].

In section 5.3 we monitored the number growth of swimming and sessile cells in the medium-rich environment of a microchannel during the early stage of biofilm formation. We observed that the first generation of sessile cells experienced a surface associated lag time of $3:30$ hours before they started to grow by binary fission forming colonies of increasing size. The number of cells on the surface increased continuously with an average doubling time of $t_d \approx 1.7$ hours. At the same time we observed that the number of swimming cells, which coexisted with the surface attached clusters, remained constant. Approximately $5:30$ hours after the beginning of the experiment we measured a sudden jump in the number of swimming cells which was accompanied by a breakup of bigger surface attached colonies, that contained 8 to 16 cells, corresponding to three to four cycles of cell divisions. Subsequently the microchannel was dominated by a population of cells in the swimming state while approximately $6:30-7:00$ hours after the beginning of the experiment we observed that individual cells reattached to the surface.

With a similar process being reported for *Pseudomonas fluorescence* by Lawrence et al. [88], we interpreted this transition as an emigration and recolonization event, where biofilm forming cells first grow to defined sizes at the surface. After that, flagella synthesis in a number of sessile cells is renewed and daughter cells are emitted to swim and explore towards new growth environments. We performed additional experiments to investigate whether the observed transition is triggered by (1) a depletion of the growth medium, (2) quorum sensing or mechanosensing after the density of cells on the surface or the size of the colonies exceeds a certain threshold, or (3) the time a cell has spent on the surface after initial attachment.

In experiments where the growth medium was constantly renewed by a periodic flow and in experiments where the initial seeding density of cells was varied, colony dispersal and release of cells to the swimming phase proceeded at comparable times. This is a strong indication that the observed transition is not triggered by a growth medium depletion and independent of the global density of cells on the surface. In an additional experiment we used a microfluidic device with a Y-shaped geometry. Manipulation of medium and buffer flow allowed us to first colonize a predefined subregion of the microchannel and then monitor the growth of a 'secondary' offspring population of cells which would colonize initially uncovered areas of the channel. We found a synchronous dissolution of cells to the swimming phase in both neighboring areas. While cells from

the 'primary' population had grown to sizes comparable to the previous experiment (8-16 cells) and had been in contact with the surface for 230 min, colonies from the 'secondary' population had grown to a much smaller size (4-8 cells on average) and had only spent around 80 min on the surface. These results indicate that the release of cells into the planktonic phase does not depend on the colony size nor the contact time with the surface. Instead we propose that, while not directly dependent on the contact time, the transition is triggered by a purely local adaption process after cells have undergone a fixed number of division cycles on the surface. After three to five generations in a sessile lifestyle, proteins encoding flagellar synthesis are upregulated and motile cells detach from the surface. This is supported by similar observations on the surface related growth of *Pseudomonas fluororescens*, where under continuous flow conditions a global detachment of cells from the colonies was observed after four division cycles [88]. Because cells from the 'secondary' population 'remember' the number of division cycles spent during growth as part of the 'primary' population, the release to the swimming phase occurs simultaneously in both populations.

In conclusion, using microfluidic devices together with cell tracking at different timescales proved us a productive approach to study the motility of swimming microorganism and surface related growth under hydrodynamically stable conditions. However, several points of this work motivate complementary future experiments:

Regarding the reversal events in the swimming pattern of *P. putida*, a visualization of the flagellar reorientation during a reversal is necessary to confirm or reject the proposed scenario. From our side, several attempts to stain the filaments with various fluorescent dyes were unsuccessful, partly because of the phototoxic effect of the excitation light on the flagellar motor, partly because the necessities of the staining protocol were incompatible with essential steps required in the preparation of experiments on swimming cells. Our experience suggests that an indirect approach, e.g. to image the flow field around the cell using fluorescent tracer particles like in [42], might more likely yield sufficient results to clarify the reorientation behavior of flagella during a reversal. Alternatively, one could also track the motion of fluorescent nanobeads which bind to the flagellar filaments [111].

A significant part of this work was devoted to establish a method to acquire three dimensional trajectories of swimming cells from fast Z-scans using a piezo driven objective mount coupled to a high speed camera. From the reconstruction algorithm we did not only acquire the three-dimensional position of a cell's center of mass but also retrieved the full information on the three dimensional morphology of the cell body, usually with the shape of a prolate ellipsoid. Preliminary results indicate that, in particular while

swimming near a solid boundary, at certain distances the swimming direction is not always aligned with the principal axis of the cell body. In theoretical models presented so far this is not taken into account, the swimming direction is always concentrated on the principal axis of the cell body. Systematic experiments to investigate such cases of 'drift swimming' near boundaries eventually with a constant 'equilibrium pitch angle' of the cell body with respect to the surface may give interesting insights.

During experiments which investigated the sudden release of cells into the planktonic phase after a longer period of surface associated growth, we did not follow the behavior of individual cells. To supplement our conjecture that detachment occurs after a constant number of division cycles on the surface and is independent of collective effects, we suggest an experiment where the 'fate' of an individual cell can be tracked for more than six hours through periods of planktonic life and sessile growth. This could be most easily achieved by staining a subpopulation of individual cells and complemented by experiments with mutant cell lines expressing a fluorescent marker after a fixed number of division cycles.

Chapter 7

Acknowledgements

First of all, i want to thank my supervisor, Prof. Carsten Beta, for the opportunity to work in his group and for accepting me as a student of the research training group 1558 on collective dynamics. I am deeply grateful of his open ear for questions and the informal and personal working atmosphere i enjoyed with him. Among many things i want to acknowledge most his strategic far-sightedness and his structured approach to all scientific questions. No matter which problems occurred during my PhD, his calm and deeply professional way of guiding me through the world of science always kept me on track. Personally, i am grateful for his emphasis on presenting scientific results with a clear and structured language. This is not self-evident in all parts of the scientific community.

Within the biological physics group i am grateful to Eva Barbosa Pfannes, whose biological background helped me to establish successful protocols for studying bacterial motility. Similar credit goes to Robert Niedl. Together with Eva, his expertise as well as his cheerful and communicative spirit pushed me through the ups and downs experienced throughout my work on this thesis. The current state of the three-dimensional cell-tracking project would not be possible without the contribution from Achim Quaas, a studentische Hilfskraft which was assigned to me within the research training group. I particularly benefited from his programming skills and his practical technical knowledge. I strongly appreciated plenty of scientic and non-scientific discussions with Marius Hintsche, my successor on the biofilm project, and with 'my' fellow bachelor students Oliver Nagel, Michael Raatz and Marco Bahrs. The experimental part of this work would not be possible without the steady and professional work of our technician Kirsten Krüger. I also want to thank her for organizing the group outings and in general for her care about all things related to the social life within the Biological Physics group.

From the research training group i want to thank Prof. Holger Stark for the successful

collaboration and for his commitment as RTG chairman. In the end it was the generous funding within this framework that enabled my project. Equal thanks goes to Dr. Vasily Zabuerdaev for his close supervision and theoretical expertise. In particular i am grateful to Johannes Taktikos, who contributed the theoretical modeling part to this work. I enjoyed the scientific discussions with him and the mutual support during presentations at the regular conference meetings. Our communication was informal and carried by mutual respect and friendliness, a strong basis for all fruitful scientific collaboration. The collaboration within the research training group strongly dependent on the successful coordination by Julia Eckert from the Technical University of Berlin. I want to thank her for her responsive and competent way of solving all organizational issues and sometimes worries, that occurred during this work and especially for her cheerful and encouraging attitude while doing so.

Though not directly related to the work presented in this thesis but because my evolution as a researcher did not start from nowhere, i want to express once more my gratitude to the old 'Goettingen-Team' with Albert Bae, Christian Westendorf and Gabriel Amselem in the Biological Physics group of Prof. Bodenschatz where it all started.

I want to thank all people that i at this very moment forgot to mention and all the others that were giving me company and support during my past years here in Berlin. Most of all, i am deeply grateful to my parents Isolde and Bernd Theves and also to my grandmother Maria Heischel. I simply owe them EVERYTHING.

'Ich dachte, das wird ein Abenteuer, aber es war das ganze Leben.' (Joseph Conrad)

Appendix A

Appendix

A.1 Force estimate: Fast turn of a low Reynolds number bacterium

Since we are in the low Reynolds number regime, inertial forces can be neglected. With only viscous drag opposing the rotation of a bacterium, approximated by a sphere, the equation of motion reads

$$N = \gamma_R \Omega_D \tag{A.1}$$

with $N = \left(\frac{dL}{dt}\right)$ for the required torque, $\Omega_D = \left(\frac{d\Theta}{dt}\right)$ for the angular drift velocity and $\gamma_R = 8\pi\eta R^3$ for the drag coefficient of a bacterium modeled as a spheroid. For a full 180 degree turn during a time ϵ, with a radius $R = 1$ μm and the viscosity of water $\eta = 1$ Ns/m^2 we obtain

$$\begin{aligned} N &= \frac{8\pi^2}{\epsilon}\frac{[N][s]}{m^2}[\mu m]^3 && \text{(A.2)} \\ &= \frac{8\pi^2}{\epsilon}[pN][\mu m][s], && \text{(A.3)} \end{aligned}$$

which yields the values listed in table A.1.

N [pN μm]	ϵ [s]	Ω_D [rad/s]
159	0.50	2π
790	0.10	31
1974	0.04	78
3948	0.02	157
7896	0.01	314

Table A.1: Estimate on the required torque for a 180 degree turn of a spheroid as a function of the turning time ϵ or the corresponding rotational frequency Ω_D.

From the Stokes law we can estimate a total propulsion force on the order of ≈ 565 pN for a cell propagating at a speed of 30 μm/s. We recorded time series at 50 fps. According to table A.1 an unnoticed 180 degree turn ($\epsilon < 0.02$ s) would require a force on one polar end of the bacterium around 4000 pN. This is around eight times higher than the total propulsion force. It is thus unlikely that a reversal in the cell trajectory is accompanied by a full turn of the cell body, unnoticed at our given frame rate.

A.2 Curvature of two subsequent runs in the presence of two solid boundaries

The sample trajectory in figure A.1 displays a cell swimming in the confined environment between the two channel boundaries. The cell alternates between curved and straight runs.

Analogously to the analysis of cell trajectories near a single boundary, we plotted the average curvatures of two subsequent runs against each other (figure A.2(a)). Some points cluster near the x- or y-axis, which corresponds to changes from highly curved to relatively straight runs with low curvature. The distribution for changes in curvature magnitude normalized by the sum of the two magnitudes is shown in figure A.2(b). Except for a small peak at -0.9 it is uniform. There is no indication that upon a reversal the magnitude of the curvature in the following run changes in a systematic fashion. In figure A.2(c) we plot the curvature product divided by the sum of the curvature magnitude. Though slightly biased towards negative values the distribution is centered at zero. There is no indication that upon a reversal the cell changes from a right curved ($\kappa < 0$) to a left curved ($\kappa > 0$) run trajectory or vice versa.

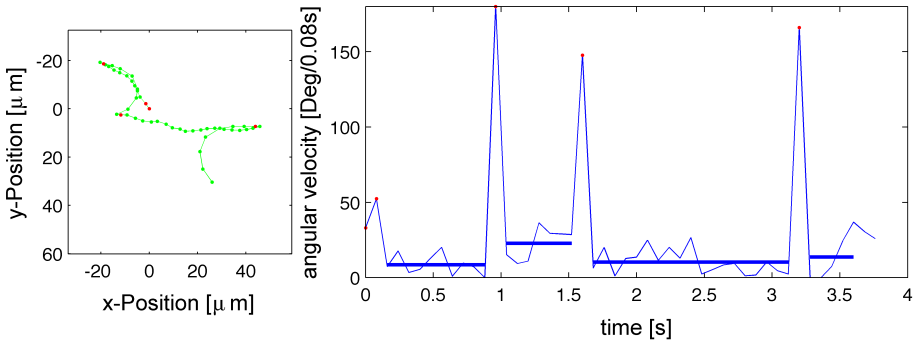

Fig. A.1: Sample trajectory of a cell swimming inside a microchannel with a height of $10\ \mu$m. (left) Runs in green are interrupted by 180 degree turns (reversals) in red. (right) Angular velocity of the same cell as a function of time: between its reversal events in red, the cell alternates between runs with higher and lower curvature (average angular velocity of the corresponding run is designated by thick blue line).

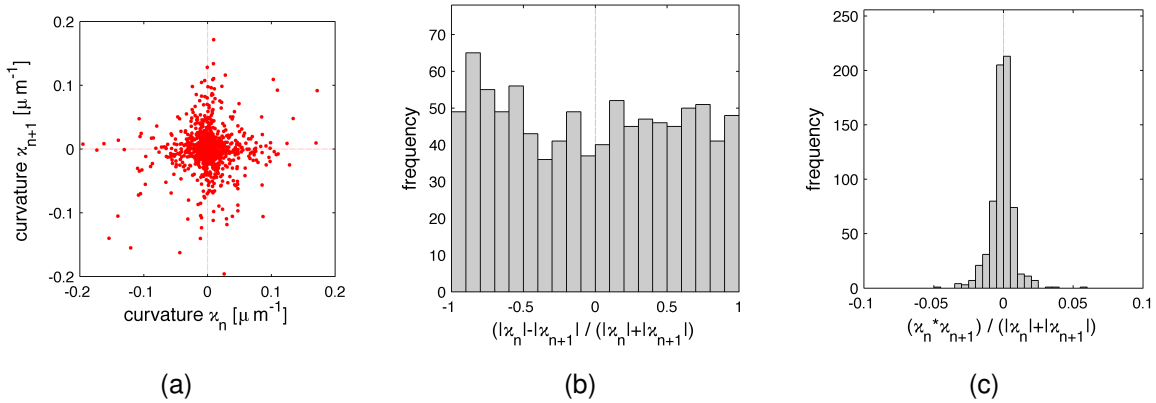

Fig. A.2: (a) Average curvature of two subsequent runs. Some points cluster along the xy-axis indicating that occasionally curved runs and straight lines alternate. (b) Frequency distribution of differences in curvature magnitude normalized by the sum of the two magnitudes. (c) Frequency distribution of the curvature product normalized by the sum of the average curvature magnitudes. See text for description.

A.3 Mean square displacement and velocity autocorrelation function of a run-reverse random walker with alternating speeds [1]

In the following we derive the velocity autocorrelation (VACF) and mean square displacement (MSD) for the random walk model presented in section 5.1.2. In the simple random walk model, the cell is alternating between two constant speeds v_1 and v_2, and the run times are exponentially distributed with a mean run time τ.

Consequently the runtimes follow Poisson statistics, and the probability for n turn events to occur within a time t is given by

$$p_n(t) = \frac{(\lambda t)^n}{n!} e^{-\lambda t} \tag{A.4}$$

with $\lambda = \tau^{-1}$ for the turning rate. For a cell starting with a speed v_1 at time $t = 0$ the VACF can be written as

$$\langle \boldsymbol{v}(0) \cdot \boldsymbol{v}(t) \rangle = p_0 v_1^2 + p_1 v_1 v_2 \alpha + p_2 v_1^2 \alpha^2 + p_3 v_1 v_2 \alpha^3 + ... \tag{A.5}$$

or alternatively, if the cell starts with v_2, as

$$\langle \boldsymbol{v}(0) \cdot \boldsymbol{v}(t) \rangle = p_0 v_2^2 + p_1 v_1 v_2 \alpha + p_2 v_2^2 \alpha^2 + p_3 v_1 v_2 \alpha^3 + ... \quad . \tag{A.6}$$

Like in Lovely et al. [98], the parameter $\alpha = \langle \cos \psi \rangle$ reflects the persistence of the random walk and can be calculated from the experimental distribution of turning angles ψ and the series of exponents α^n are due to the occurrence of n turn events up to the time t.

By taking the average over equation A.5 and equation A.6 and using equation A.4 we get

$$\begin{aligned} \langle \boldsymbol{v}(0) \cdot \boldsymbol{v}(t) \rangle &= p_0 \frac{v_1^2 + v_2^2}{2} + p_1 v_1 v_2 \alpha + p_2 \frac{v_1^2 + v_2^2}{2} \alpha^2 + ... & \text{(A.7)} \\ &= e^{-\lambda t} \left(\frac{v_1^2 + v_2^2}{2} \cosh(\lambda \alpha t) + v_1 v_2 \sinh(\lambda \alpha t) \right). & \text{(A.8)} \end{aligned}$$

[1] The mathematical derivation of this model was done by Johannes Taktikos, Vasily Zaburdaev and Holger Stark, in close collaboration with the author.

Analogously to [98], we can include rotational diffusion as another Poison process by adding an additional factor $e^{-2D_R t}$ to the right-hand side of equation A.7 which then reads

$$\langle \boldsymbol{v}(0) \cdot \boldsymbol{v}(t) \rangle = e^{-(\lambda+2D_R)t} \left(\frac{v_1^2 + v_2^2}{2} \cosh(\lambda\alpha t) + v_1 v_2 \sinh(\lambda\alpha t) \right), \tag{A.9}$$

given as equation 5.1 in section 5.1.2.

From the analytic expression for the VACF we can calculate the MSD by integrating twice over time

$$\langle \boldsymbol{d}(t)^2 \rangle = \int_0^t dt' \int_0^t dt'' \langle \boldsymbol{v}(t') \boldsymbol{v}(t'') \rangle. \tag{A.10}$$

This gives a lengthy expression which after simplification for large times reads

$$D = \lim_{t\to\infty} \frac{\langle \boldsymbol{d}(t)^2 \rangle}{(4t)} = \frac{2D_R(v_1^2 + v_2^2) + \lambda(v_1^2 + v_2^2 + 2\alpha v_1 v_2)}{6[2D_R + \lambda(1-\alpha)][2D_R + \lambda(1+\alpha)]}, \tag{A.11}$$

reconstituting equation 5.2 from section 5.1.2.

A.4 Measurement bias on turning angle distribution in two dimensions

Because we are looking at the two-dimensional projection of a swimming cell, the distribution of turning angles ψ determined from the analysis of two-dimensional trajectories (section 5.1.1 and section 5.2.1) differs from the turning angle distribution Φ, which was calculated from three-dimensional trajectories (section 5.2.3). Here we want to estimate the bias of the two-dimensional projection and give a quantitative relationship between ψ and Φ.

In figure A.3 we display two velocity vectors $\boldsymbol{v}_n$ and $\boldsymbol{v}_{n+1}$, which correspond to the directions of two subsequent runs. The turning angle calculated from the three-dimensional trajectories, Φ, lies in the plane spanned by the two vectors. In the two-dimensional projection we measure the angle ψ lying in the xy-plane. In the following α denotes the angle by which the plane of the two three-dimensional vectors is tilted with respect to the xy-plane.

From figure A.3 we get

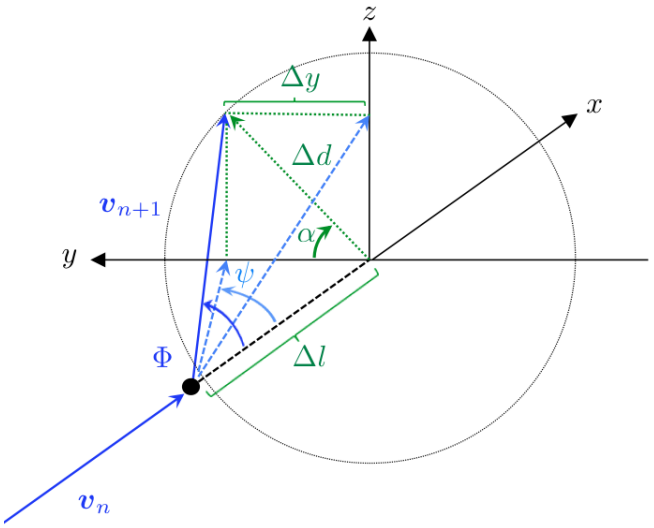

Fig. A.3: Schematic presentation of the two different turning angles calculated from two- and three-dimensional trajectories. The angle Φ represents the turning angle in three-dimensions and lies in the plane spanned by the two velocity vectors $\boldsymbol{v}_n$ and $\boldsymbol{v}_{n+1}$, while ψ lies in the xy-plane and represents the angle between the two-dimensional projections of the two vectors. See text for closer description.

$$\Delta y = \cos\alpha \Delta d \quad , \quad \Delta d = \sin\Phi |\boldsymbol{v}_{n+1}| \quad \text{and} \quad \Delta l = \cos\Phi |\boldsymbol{v}_{n+1}|, \tag{A.12}$$

and for the turning angle in two dimensions

$$\tan\psi = \frac{\Delta y}{\Delta l}. \tag{A.13}$$

Using both equation A.12 and A.12 yields

$$\tan\psi = \frac{\cos\alpha \sin\Phi}{\cos\Phi}$$

and thus a relationship between ψ and Φ

$$\psi = \arctan(\cos\alpha \tan\Phi). \tag{A.14}$$

For a three-dimensional turning angle Φ and we can now calculate the two-dimensional turning angle as a function of the tilt angle α which we display in figure A.4(a). For $\alpha = 0°$, we determine the same turning angles in two and three dimensions ($\Phi = \psi$) while for $\alpha = 90°$ the bias from the two dimensional projection is strongest. In this case we have $\psi = 0°$ for $\Phi < 90°$ and $\psi = 180°$ for $\Phi > 90°$.

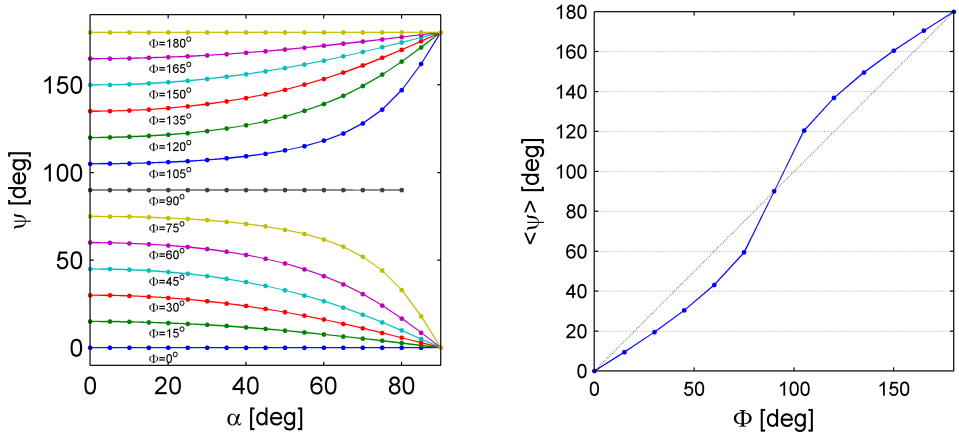

(a) (b)

Fig. A.4: (a) Turning angle ψ as a function of the tilt angle α determined from the two-dimensional projection of various turns in three dimensions with angle Φ function (see equation A.14). While the angles $\Phi = 0°, 90°,$ and $180°$ are not affected, the projection ψ deviates stronger from Φ with increasing α. (b) Expectation value $\langle\psi\rangle$ as a function of Φ assuming that all values α are equally probable. See text for closer description.

If we assume that in our two-dimensional tracking experiments all angles α by which the plane spanned by the two vectors $\boldsymbol{v}_n$ and $\boldsymbol{v}_{n+1}$ is tilted with respect to the xy-plane are equally probable, we can calculate the expectation value

$$\langle\psi\rangle = \int_0^{\pi/2} d\alpha \arctan(\cos\alpha \tan\Phi) \tag{A.15}$$

as a function of Φ. This integration can only be solved numerically and the result is shown in figure A.4(b). We see that for $\Phi < 90°$ the two-dimensional projection ψ underestimates the magnitude of the turn while for $\Phi > 90°$ the turning angle is overestimated.

References

[1] S.-I. Aizawa. Flagellar assembly in salmonella typhimurium. *Molecular Microbiology*, 19(1):1–5, 1996.

[2] I. Albers et al. *Molecular Biology of the Cell*. Garland Science, New York, 5th edition, 2008.

[3] J. P. Armitage and R. M. Macnab. Unidirectional, intermittent rotation of the flagellum of rhodobacter sphaeroides. *Journal of Bacteriology*, 169(2):514–518, 1987.

[4] G. M. Barbara and J. G. Mitchell. Bacterial tracking of motile algae. *FEMS Microbiology Ecology*, 44(1):79–87, 2003.

[5] S. M. Barns, R. E. Fundyga, M. W. Jeffries, and N. R. Pace. Remarkable archaeal diversity detected in a yellowstone-national-park hot-spring environment. *Proceedings of the National Academy of Sciences*, 91(5):1609–1613, 1994.

[6] H. C. Berg. *Random Walks in Biology*. Princeton University Press, Princeton, New Jersey, expanded edition, 1993.

[7] H. C. Berg. Torque generation by the flagellar rotary motor. *Biophysical Journal*, 68(4):163–167, 1995.

[8] H. C. Berg and D. A. Brown. Chemotaxis in *Escherichia coli* analyzed by Three-dimensional Tracking . *Nature*, 239:500–504, 1972.

[9] H. C. Berg and L. Turner. Movement of microorganisms in viscous environments. *Nature*, 278(5702):349–351, 1979.

[10] H. C. Berg and L. Turner. Chemotaxis of bacteria in glass capillary array. *Biophysical Journal*, 58(4):919–930, 1990.

[11] H.C. Berg. *E. coli in motion*. Springer Inc., New York, Berlin, Heidelberg, 2004.

[12] Howard C. Berg. The rotary motor of bacterial flagella. *Annual Review of Biochemistry*, 72(1):19–54, 2003.

[13] A. Berke, L. Turner, H. Berg, and E. Lauga. Hydrodynamic attraction of swimming microorganisms by surfaces. *Physical Review Letters*, 101(3):038102, 2008.

[14] S. Bhattacharya, A. Datta, J.M. Berg, and S. Gangopadhyay. Studies on surface wettability of poly(dimethyl) siloxane (pdms) and glass under oxygen-plasma treatment and correlation with bond strength. *Journal of Microelectromechanical Systems*, 14(3):590–597, 2005.

[15] N. Biais, B. Ladoux, D. Higashi, M. So, and M. Sheetz. Cooperative retraction of bundled type iv pili enables nanonewton force generation. *PLoS Biology*, 6(4):e87, 2008.

[16] S. M. Block and H. C. Berg. Successive incorporation of force-generating units in the bacterial rotary motor. *Nature*, 309(5967):470–472, 1984.

[17] R. Brinkmeyer, K. Knittel, J. Jurgens, H. Weyland, R. Amann, and E. Helmke. Diversity and structure of bacterial communities in arctic versus antarctic pack ice. *Applied and Environmental Microbiology*, 69(11):6610–6619, 2003.

[18] S. M. Butler and A. Camilli. Going against the grain: Chemotaxis and infection in vibrio cholerae. *Nature Reviews Microbiology*, 3(8):611–620, 2005.

[19] C. R. Calldine. Change of waveform in bacterial flagella: The role of mechanics at the molecular level. *Journal of Molecular Biology*, 118(4):457–479, 1978.

[20] S. Chattopadhyay. *Study of Bacterial Motility using Optical Tweezers*. PhD thesis, University of Pittsburgh, 2008.

[21] S. Chattopadhyay, R. Moldovan, C. Yeung, and X. L. Wu. Swimming efficiency of bacterium escherichia coli. *Proceedings of the National Academy of Science of the United States of America*, 103(37):13712–13717, 2006.

[22] S. Chattopadhyay and X.-L. Wu. The effect of long-range hydrodynamic interaction on the swimming of a single bacterium. *Biophysical Journal*, 96(5):2023–2028, 2009.

[23] M. K. Chaudhury and G. M. Whitesides. Correlation between surface free energy and surface constitution. *Science*, 255(5049):1230–1232, 1992.

[24] C. Q. Chiam, Chui C. W., Sanjay S., and Keng-Hwee. Bacterial tethering analysis reveals ”run-reverse-turn” mechanism for pseudomonas spp. motility. *Environmental Microbiology*, 79(15):4734–4743, 2013.

[25] H. J. Cho, H. Jonsson, K. Campbell, P. Melke, J. W. Williams, B. Jedynak, A. M. Stevens, A. Groisman, and A. Levchenko. Self-organization in high-density bacterial colonies: Efficient crowd control. *Plos Biology*, 5(11):2614–2623, 2007.

[26] L. Cisneros, C. Dombrowski, R. Goldstein, and J. Kessler. Reversal of bacterial locomotion at an obstacle. *Physical Review E*, 73(3), 2006.

[27] P. Cluzel, M. Surette, and S. Leibler. An ultrasensitive bacterial motor revealed by monitoring signaling proteins in single cells. *Science*, 287(5458):1652–1655, 2000.

[28] E. A. Codling, M. J. Plank, and S. Benhamou. Random walk models in biology. *Journal of The Royal Society Interface*, 5(25):813–834, 2008.

[29] J. C. Conrad. Physics of bacterial near-surface motility using flagella and type iv pili: implications for biofilm formation. *Research in Microbiology*, 163(9-10):619–29, 2012.

[30] E. K. Costello, S. R. P. Halloy, S. C. Reed, P. Sowell, and S. K. Schmidt. Fumarole-supported islands of biodiversity within a hyperarid, high-elevation landscape on socompa volcano, puna de atacama, andes. *Applied and Environmental Microbiology*, 75(3):735–747, 2009.

[31] J. W. Costerton, Philip S. Stewart, and E. P. Greenberg. Bacterial biofilms: A common cause of persistent infections. *Science*, 284(5418):1318–1322, 1999.

[32] J. C. Crocker and D. G. Grier. Methods of digital video microscopy for colloidal studies. *Journal of Colloid and Interface Science*, 179(1):298–310, 1996.

[33] A. F. Daniel and J. A. Theriot. An introduction to cell motility for the physical scientist. *Physical Biology*, 1:T1–T10, 2004.

[34] N. C. Darnton, L. Turner, S. Rojevsky, and H. C. Berg. On Torque and Tumbling in Swimming Escherichia coli . *J. Bacteriology*, 189(5):1756–1764, 2007.

[35] M. E. Davey and G. A. O'Toole. Microbial biofilms: from ecology to molecular genetics. *Microbiology and Molecular Biology Reviews*, 64(4):847–867, 2000.

[36] D. G. Davies, A. M. Chakrabarty, and G. G. Geesey. Exopolysaccharide production in biofilms: substratum activation of alginate gene expression by pseudomonas aeruginosa. *Applied and Environmental Microbiology*, 59(4):1181–1186, 1993.

[37] D. G. Davies, M. R. Parsek, J. P. Pearson, B. H. Iglewski, J. W. Costerton, and E. P. Greenberg. The involvement of cell-to-cell signals in the development of a bacterial biofilm. *Science*, 280(5361):295–298, 1998.

[38] M. L. Davis, L. C. Mounteer, L. K. Stevens, C. D. Miller, and A. Zhou. 2d motility tracking of pseudomonas putida kt2440 in growth phases using video microscopy. *Journal of Bioscience and Bioengineering*, 111(5):605–611, 2011.

[39] L.E Den Doorden de Jong. *Bijdrage Tot de Kennis van het Mineralisatieproces*. PhD thesis, Rotterdam, 1926.

[40] R. Di Leonardo, D. Dell'Arciprete, L. Angelani, and V. Lebba. Swimming with an image. *Physical Review Letters*, 106(3):038101, 2011.

[41] R. M. Donlan and J. W. Costerton. Biofilms: Survival mechanisms of clinically relevant microorganisms. *Clinical Microbiology Review*, 15(2):167–193, 2002.

[42] K. Drescher, J. Dunkel, L. H. Cisneros, S. Ganguly, and R. E. Goldstein. Fluid dynamics and noise in bacterial cell-cell and cell-surface scattering. *Proceedings of the National Academy of Sciences*, 108(27):10940–10945, 2011.

[43] D. C. Duffy, J. C. McDonald, O. J. A. Schueller, and G. M. Whitesides. Rapid prototyping of microfluidic systems in poly(dimethylsiloxane). *Analytical Chemistry*, 70(23):4974–4984, 1998.

[44] K. J. Duffy and R. M. Ford. Turn angle and run time distributions characterize swimming behavior for pseudomonas putida. *Journal of Bacteriology*, 179(4):1428–1430, 1997.

[45] Michael Eisenbach. *Bacterial Chemotaxis*. John Wiley and Sons Ltd, Hoboken, New Jersey, 2001.

[46] M. Espinosa-Urgel and J. L. Ramos. Cell density-dependent gene contributes to efficient seed colonization by pseudomonas putida kt2440. *Applied and Environmental Microbiology*, 70(9):5190–5198, 2004.

[47] Manuel Espinosa-Urgel, R. Kolter, and J.-L Ramos. Root colonization by pseudomonas putida: love at first sight. *Microbiology*, 148(2):341–343, 2002.

[48] H.-C. Flemming and J. Wingender. The biofilm matrix. *Nature Review Microbiology*, 8(9):623–633, 2010.

[49] M. Ford. Chilean extremophile bacteria thrive in mars-like conditions. *Ars Technica*, 2009.

[50] B. M. Friedrich, I. H. Riedel-Kruse, J. Howard, and F. Juelicher. High-precision tracking of sperm swimming fine structure provides strong test of resistive force theory. *The Journal of Experimental Biology*, 213(8):1226–1234, 2010.

[51] E. Frimmersdorf, S. Horatzek, A. Pelnikevich, L. Wiehlmann, and D. Schomburg. How pseudomonas aeruginosa adapts to various environments: a metabolomic approach. *Environmental Microbiology*, 12(6):1734–1747, 2010.

[52] B. Galan, E. Diaz, and J. L. Garcia. Enhancing desulphurization by engineering a flavin reductase-encoding gene cassette in recombinant biocatalysts. *Environmental Microbiology*, 2(6):687–694, 2000.

[53] F. Garcia-Pichel, J. Belnap, S. Neuer, and F. Schanz. Estimates of global cyanobacterial biomass and its distribution. *Archiv fuer Hydrobiologie Supplement*, 148:213–227, 2003.

[54] M. Gjermansen, P. Ragas, C. Sternberg, S. Molin, and T. Tolker-Nielsen. Characterization of starvation-induced dispersion in pseudomonas putida biofilms. *Environmental Microbiology*, 7(6):894–904, 2005.

[55] R. Gonzales and R. Woods. *Digital Image Processing*. Addison Wesley, Prentice Hall, third edition, 2008.

[56] J. Gray. The movement of sea-urchin spermatozoa. *Journal of Experimental Biology*, 32(4):775–801, 1955.

[57] J. Gray and G. J. Hancock. The propulsion of sea-urchin spermatozoa. *Journal of Experimental Biology*, 32(4):802–814, 1955.

[58] G. Gregoire and H. Chate. Onset of collective and cohesive motion. *Physical Review Letters*, 92(2):025702, 2004.

[59] L. Hall-Stoodley, J. W. Costerton, and P. Stoodley. Bacterial biofilms: From the natural environment to infectious diseases. *Nature Reviews Microbiology*, 2(2):95–108, 2004.

[60] Brian K. Hammer and Bonnie L. Bassler. Quorum sensing controls biofilm formation in vibrio cholerae. *Molecular Microbiology*, 50(1):101–104, 2003.

[61] S. K. Hansen, P. B. Rainey, J. A. J. Haagensen, and S. Molin. Evolution of species interactions in a biofilm community. *Nature*, 445(7127):533–536, 2007.

[62] A. Hansler, Q. Y. Chen, B. Crane, and S. Gross. Endogenous nitric oxide production in the radioresistant bacterium deinococcus radiodurans determines lipid composition and is essential for rapid growth recovery after gamma-irradiation. *Nitric Oxide-Biology and Chemistry*, 27:S16, 2012.

[63] J. Happel and H. Brenner. *Low Reynolds number hydrodynamics*. Martinus Nijhoff Publishers, Dordrecht, Boston, Lancaster, 2nd revised edition, 1983.

[64] C. S. Harwood, K. Fosnaugh, and M. Dispensa. Flagellation of pseudomonas putida and analysis of its motile behavior. *Journal of Bacteriology*, 171(7):4063–4066, 1989.

[65] C. S. Harwood, R. E. Parales, and M. Dispensa. Chemotaxis of pseudomonas putida toward chlorinated benzoates. *Applied and Environmental Microbiology*, 56(5):1501–1503, 1990.

[66] N. I. Hendey. Some observations on cladosporium resinae as a fuel contaminant and its possible role in the corrosion of aluminium alloy fuel tanks. *Transactions of the British Mycological Society*, 47(4):467–475, 1964.

[67] J. Henrichsen. Bacterial surface translocation - survey and a classification. *Bacteriological Reviews*, 36(4):478–503, 1972.

[68] M. E. Hibbing, C. Fuqua, M. R. Parsek, and S. B. Peterson. Bacterial competition: surviving and thriving in the microbial jungle. *Nature Review Microbiology*, 8(1):15–25, 2010.

[69] D. L. Higashi, S. W. Lee, A. Snyder, N. J. Weyand, A. Bakke, and M. So. Dynamics of neisseria gonorrhoeae attachment: Microcolony development, cortical plaque formation, and cytoprotection. *Infection and Immunity*, 75(10):4743–4753, 2007.

[70] H. Hillborg, J. F. Ankner, U. W. Gedde, G. D. Smith, H. K. Yasuda, and K. Wikström. Crosslinked polydimethylsiloxane exposed to oxygen plasma studied by neutron reflectometry and other surface specific techniques. *Polymer*, 41(18):6851–6863, 2000.

[71] F. Jin, J. C. Conrad, M. L. Gibiansky, and G. C. L. Wong. Bacteria use type-iv pili to slingshot on surfaces. *Proceedings of the National Academy of Sciences*, 108(31):12617–12622, 2011.

[72] J. E. Johansen, J. Pinhassi, N. Blackburn, U. L. Zweifel, and A. Hagstroem. Variability in motility characteristics among marine bacteria. *Aquatic Microbial Ecology*, 28(3):229–237, 2002.

[73] J. N. Kapur, P. K. Sahoo, and A. K. C. Wong. A new method for gray-level picture thresholding using the entropy of the histogram. *Computer Vision, Graphics, and Image Processing*, 29(3):273–285, 1985.

[74] M. G. Katsikogianni and Y. F. Missirlis. Bacterial adhesion onto materials with specific surface chemistries under flow conditions. *Journal of Materials Science: Materials in Medicine*, 21(3):963–968, 2010.

[75] D. F. Katz, J. R. Blake, and S. L. Paverifontana. Movement of slender bodies near plane boundaries at low reynolds number. *Journal of Fluid Mechanics*, 72(DEC9):529–540, 1975.

[76] M. Kim. A macroscopic scale model of bacterial flagellar bundling. *Proceedings of the National Academy of Sciences*, 100(26):15481–15485, 2003.

[77] M. J. Kim and T. R. Powers. Hydrodynamic interactions between rotating helices. *Physical Review E*, 69(6):061910, 2004.

[78] S. Kim and S. J. Karilla. *Microhydrodynamics: Principles and Selected Applications*. Dover Publications Inc., New York, 2005.

[79] I. Klapper and J. Dockery. Mathematical description of microbial biofilms. *Siam Review*, 52(2):221–265, 2010.

[80] M. Klausen, M. Gjermansen, J.-U. Kreft, and T. Tolker-Nielsen. Dynamics of development and dispersal in sessile microbial communities: examples from pseudomonas aeruginosa and pseudomonas putida model biofilms. *Fems Microbiology Letters*, 261(1):1–11, 2006.

[81] M. Klausen, A. Heydorn, P. Ragas, L. Lambertsen, A. Aaes-Jorgensen, S. Molin, and T. Tolker-Nielsen. Biofilm formation by pseudomonas aeruginosa wild type, flagella and type iv pili mutants. *Molecular Microbiology*, 48(6), 2003.

[82] S.i Kudo, N. Imai, M. Nishitoba, S. Sugiyama, and Y. Magariyama. Asymmetric swimming pattern of vibrio alginolyticus cells with single polar flagella. *Fems Microbiology Letters*, 242(2):221–225, 2005.

[83] J. Lacal, F. Munoz-Martinez, J. A. Reyes-Darias, E. Duque, M. Matilla, A. Segura, J. J. Calvo, C. Jimenez-Sanchez, T. Krell, and J. L. Ramos. Bacterial chemotaxis towards aromatic hydrocarbons in pseudomonas. *Environmental Microbiology*, 13(7):1733–44, 2011.

[84] E. Lauga, W. R. DiLuzio, G. M. Whitesides, and H. A. Stone. Swimming in circles: motion of bacteria near solid boundaries. *Biophysical Journal*, 90(2):400–412, 2006.

[85] E. Lauga, W. R. DiLuzio, G. M. Whitesides, and H. A. Stone. Swimming in circles: motion of bacteria near solid boundaries. *Biophysical Journal*, 90(2):400–12, 2006.

[86] E. Lauga and T. R. Powers. The hydrodynamics of swimming microorganisms. *Reports on Progress in Physics*, 72(9), 2009.

[87] P. Lauger. Torque and rotation rate of the bacterial flagellar motor. *Biophysical Journal*, 53(1):53–65, 1988.

[88] J. R. Lawrence, P. J. Delaquis, D. R. Korber, and D. E. Caldwell. Behavior of pseudomonas-fluorescens within the hydrodynamic boundary-layers of surface microenvironments. *Microbial Ecology*, 14(1):1–14, 1987.

[89] S. Lecuyer, R. Rusconi, Y. Shen, A. Forsyth, H. Vlamakis, R. Kolter, and H. A. Stone. Shear stress increases the residence time of adhesion of pseudomonas aeruginosa. *Biophysical Journal*, 100(2):341–350, 2011.

[90] P. Lewus and R. M. Ford. Quantification of random motility and chemotaxis bacterial transport coefficients using individual-cell and population-scale assays. *Biotechnology and Bioengineering*, 75(3):292–304, 2001.

[91] G. Li, J. Bensson, L. Nisimova, D. Munger, P. Mahautmr, J. Tang, M. Maxey, and Y. Brun. Accumulation of swimming bacteria near a solid surface. *Physical Review E*, 84(4), 2011.

[92] G. Li, J. Bensson, L. Nisimova, D. Munger, P. Mahautmr, J. Tang, M. Maxey, and Y. Brun. Accumulation of swimming bacteria near a solid surface. *Physical Review E*, 84(4), 2011.

[93] G. Li, J. Bensson, L. Nisimova, D. Munger, P. Mahautmr, J. Tang, M. Maxey, and Y. Brun. Accumulation of swimming bacteria near a solid surface. *Physical Review E*, 84(4), 2011.

[94] G. Li and J. X. Tang. Accumulation of microswimmers near a surface mediated by collision and rotational brownian motion. *Physical Review Letters*, 103(7):078101, 2009.

[95] Martin Li. *Experimental study of swimming flagellated bacteria and their collective behaviour in concentrated suspensions*. PhD thesis, University of Edinburgh, 2010.

[96] James M.J. Lighthill. *Mathematical Biofluiddynamics*. SIAM, Philadelphia, 1975.

[97] C. B. Lindemann and K. A. Lesich. Flagellar and ciliary beating: the proven and the possible. *Journal of Cell Science*, 123(4):519–528, 2010.

[98] P. S. Lovely and F. W. Dahlquist. Statistical measures of bacterial motility and chemotaxis. *Journal of Theoretical Biology*, 50(2):477–496, 1975.

[99] G. Lowe, M. Meister, and H. C. Berg. Rapid rotation of flagellar bundles in swimming bacteria. *Nature*, 325:637–640, 1987.

[100] R. M. Macnab. Bacterial flagella rotating in bundles - study in helical geometry. *Proceedings of the National Academy of Sciences*, 74(1):221–225, 1977.

[101] R. M. Macnab and M. K. Ornston. Normal-to-curly flagellar transitions and their role in bacterial tumbling. stabilization of an alternative quaternary structure by mechanical force. *Journal of Molecular Biology*, 112(1):1–30, 1977.

[102] Y. Magariyama, M. Ichiba, K. Nakata, K. Baba, T. Ohtani, S. Kudo, and T. Goto. Difference in bacterial motion between forward and backward swimming caused by the wall effect. *Biophysical Journal*, 88(5):3648–3658, 2005.

[103] Y. Magariyama, S. Sugiyama, and S. Kudo. Bacterial swimming speed and rotation rate of bundled flagella. *Fems Microbiology Letters*, 199(1):125–129, 2001.

[104] Y. Magariyama, S. Sugiyama, K. Muramoto, I. Kawagishi, Y. Imae, and S. Kudo. Simultaneous measurement of bacterial flagellar rotation rate and swimming speed. *Biophysical Journal*, 69(5):2154–2162, 1995.

[105] R. M. Miller, A. P. Tomaras, A. P. Barker, D. R. Voelker, E. D. Chan, A. I. Vasil, and M. L. Vasil. Pseudomonas aeruginosa twitching motility-mediated chemotaxis towards phospholipids and fatty acids: Specificity and metabolic requirements. *Journal of Bacteriology*, 190(11):4038–4049, 2008.

[106] J. Monod. The growth of bacterial cultures. *Annual Review of Microbiology*, 3:371–394, 1949.

[107] M. Morra, E. Occhiello, R. Marola, F. Garbassi, P. Humphrey, and D. Johnson. On the aging of oxygen plasma-treated polydimethylsiloxane surfaces. *Journal of Colloid and Interface Science*, 137(1):11–24, 1990.

[108] C. D. Nadell, J. B. Xavier, and K. R. Foster. The sociobiology of biofilms. *FEMS Microbiology Reviews*, 33(1):206–224, 2009.

[109] C. D. Nadell, J. B. Xavier, S. A. Levin, and K. R. Foster. The evolution of quorum sensing in bacterial biofilms. *PLoS Biology*, 6(1), 2008.

[110] T. Nakai, M. Kikuda, Y. Kuroda, and T. Goto. Speed, trajectory and increment in the number of cells of singly flagellated bacteria swimming close to boundaries. *Journal of Biomechanical Science and Engineering*, 4(1):2–10, 2009.

[111] S. Nakamura, N. Kami-ike, J. P. Yokota, T. Minamino, and K. Namba. Evidence for symmetry in the elementary process of bidirectional torque generation by the bacterial flagellar motor. *Proceedings of the National Academy of Sciences*, 107(41):17616–17620, 2010.

[112] R. Navarro-Gonzalez, F. A. Rainey, P. Molina, D. R. Bagaley, Becky J. Hollen, J. de la Rosa, A. M. Small, Richard C. Quinn, F. J. Grunthaner, L. Caceres, B. Gomez-Silva, and C. P. McKay. Mars-like soils in the atacama desert, chile, and the dry limit of microbial life. *Science*, 302(5647):1018–1021, 2003.

[113] K. E. Nelson, C. Weinel, I. T. Paulsen, R. J. Dodson, H. Hilbert, V. A. P. Martins dos Santos, D. E. Fouts, S. R. Gill, M. Pop, M. Holmes, L. Brinkac, M. Beanan, R. T. DeBoy, S. Daugherty, J. Kolonay, R. Madupu, W. Nelson, O. White, J. Peterson, H. Khouri, I. Hance, P. Chris Lee, E. Holtzapple, D. Scanlan, K. Tran, A. Moazzez, T. Utterback, M. Rizzo, K. Lee, D. Kosack, D. Moestl, H. Wedler, J. Lauber, D. Stjepandic, J. Hoheisel, M. Straetz, S. Heim, C. Kiewitz, J. Eisen, K. N. Timmis, A. Duesterhoeft, B. Tuemmler, and C. M. Fraser. Complete genome sequence and comparative analysis of the metabolically versatile pseudomonas putida kt2440. *Environmental Microbiology*, 4(12):799–808, 2002.

[114] D. H. Nies. Microbial heavy-metal resistance. *Applied Microbiology and Biotechnology*, 51(6):730–750, 1999.

[115] C. K. Omoto and C. J. Brokaw. Structure and behaviour of the sperm terminal filament. *Journal of Cell Science*, 58(1):385–409, 1982.

[116] G. O'Toole, H. B. Kaplan, and R. Kolter. Biofilm formation as microbial development. *Annual Review of Microbiology*, 54(1):49–79, 2000.

[117] H. L. Packer, H. Lawther, and J. P. Armitage. The rhodobacter sphaeroides flagellar motor is a variable-speed rotor. *FEBS Letters*, 409(1):37–40, 1997.

[118] T. Paris, S. Skali-Lami, and J.-C. Block. Effect of wall shear rate on biofilm deposition and grazing in drinking water flow chambers. *Biotechnology and Bioengineering*, 97(6):1550–1561, 2007.

[119] F. Peruani, J. Starruss, V. Jakovljevic, L. Soegaard-Andersen, A. Deutsch, and M. Baer. Collective motion and nonequilibrium cluster formation in colonies of gliding bacteria. *Physical Review Letters*, 108(9):098102, 2012.

[120] T. R. Powers. Role of body rotation in bacterial flagellar bundling. *Physical Review E*, 65(4), 2002.

[121] E. M. Purcell. The efficiency of propulsion by a rotating flagellum. *Proceedings of the National Academy of Sciences*, 94(21):11307–11311, 1997.

[122] E.M. Purcell. Life at low reynolds number. *American Journal of Physics*, 45(1):3–11, 1977.

[123] M. Ramia, D. L. Tullock, and N. Phan-Thien. The role of hydrodynamic interaction in the locomotion of microorganisms. *Biophysical Journal*, 65(2):755–778, 1993.

[124] Daniela Regenhardt. *Funktionale Genomanalyse von Pseudomonas putida KT2440*. PhD thesis, Technische Universität Braunschweig, 2003.

[125] M. Reichert and H. Stark. Synchronization of rotating helices by hydrodynamic interactions. *European Physical Journal E*, 17(4):493–500, 2005.

[126] A. R. Rice, M. A. Hamilton, and A. K. Camper. Apparent surface associated lag time in growth of primary biofilm cells. *Microbial Ecology*, 40(1):8–15, 2000.

[127] T.W. Ridler and S. Calvard. Thresholding using an iterative selection method. *IEEE Trans. System, Man and Cybernetics*, SMC-8:630–632, 1978.

[128] M. D. Rolfe, C. J. Rice, S. Lucchini, C. Pin, A. Thompson, A. D. S. Cameron, M. Alston, M. F. Stringer, R. P. Betts, J. Baranyi, M. W. Peck, and J. C. D. Hinton. Lag phase is a distinct growth phase that prepares bacteria for exponential growth and involves transient metal accumulation. *Journal of Bacteriology*, 194(3):686–701, 2012.

[129] P. Romanczuk, M. Baer, W. Ebeling, B. Lindner, and L. Schimansky-Geier. Active brownian particles. *The European Physical Journal Special Topics*, 202(1):1–162, 2012.

[130] F. A. Samatey, H. Matsunami, K. Imada, S. Nagashima, T. R. Shaikh, D. R. Thomas, J. Z. Chen, D. J. DeRosier, A. Kitao, and K. Namba. Structure of the bacterial flagellar hook and implication for the molecular universal joint mechanism. *Nature*, 431(7012):1062–1068, 2004.

[131] K. Sauer and A. K. Camper. Characterization of phenotypic changes in pseudomonas putida in response to surface-associated growth. *Journal of Bacteriology*, 183(22):6579–6589, 2001.

[132] W. R. Schneider and R. N. Doetsch. Effect of viscosity on bacterial motility. *Journal of bacteriology*, 117(2):696–701, 1974.

[133] J. E. Segall, S. M. Block, and H. C. Berg. Temporal comparisions in bacterial chemotaxis. *Proceedings of the National Academy of Sciences*, 83(23):8987–8991, 1986.

[134] T. S. Shimizu, S. V. Aksenov, and D. Bray. A spatially extended stochastic model of the bacterial chemotaxis signalling pathway. *Journal of Molecular Biololgy*, 329(2):291–309, 2003.

[135] G. S. Shreve and T. M. Vogel. Comparison of substrate utilization and growth kinetics between immobilized and suspended pseudomonas cells. *Biotechnology and Bioengineering*, 41(3):370–379, 1993.

[136] M. Simoes, L. C. Simoes, and M. J. Vieira. A review of current and emergent biofilm control strategies. *Lwt-Food Science and Technology*, 43(4):573–583, 2010.

[137] S. E. Spagnolie and E. Lauga. Hydrodynamics of self-propulsion near a boundary: predictions and accuracy of far-field approximations. *Journal of Fluid Mechanics*, 700:105–147, 2012.

[138] P. Stoodley, K. Sauer, D. G. Davies, and J. W. Costerton. Biofilms as complex differentiated communities. *Annual Review of Microbiology*, 56:187–209, 2002.

[139] J. Taktikos. *Modeling the random walk and chemotaxis of bacteria: Aspects of biofilm formation*. PhD thesis, Technische Universität Berlin, 2012.

[140] Barry L. Taylor and D. E. Koshland. Reversal of flagellar rotation in monotrichous and peritrichous bacteria: Generation of changes in direction. *Journal of Bacteriology*, 119(2):640–642, 1974.

[141] S. Terasawa, H. Fukuoka, Y. Inoue, T. Sagawa, H. Takahashi, and A. Ishijima. Coordinated reversal of flagellar motors on a single escherichia coli cell. *Biophysical Journal*, 100(9):2193–2200, 2011.

[142] K. N. Timmis. Pseudomonas putida: a cosmopolitan opportunist par excellence. *Environmental Microbiology*, 4(12):779–781, 2002.

[143] R. L. Townsin. The ship hull fouling penalty. *Biofouling*, 19:9–15, 2003.

[144] D.J. Tritton. *Physical Fluid Dynamics*. Oxford University Press Inc., New York, second edition, 2011.

[145] Y. Tu, T. S. Shimizu, and Howard C. Berg. Modeling the chemotactic response of escherichia coli to time-varying stimuli. *Proceedings of the National Academy of Sciences*, 105(39):14855–14860, 2008.

[146] L. Turner, W. S. Ryu, and H. C. Berg. Real-time imaging of fluorescent flagellar filaments. *Journal of Bacteriology*, 182(10):2793–2801, 2000.

[147] J. Valencia, J. Abalde, A. Bode, A. Cid, E. Fernandez, N. Gonzalez, J. Lorenzo, E. Teira, and M. Varela. Variations in planktonic bacterial biomass and production, and phytoplankton blooms off a coruna (nw spain). *Scientia Marina*, 67(2):143–157, 2003.

[148] S. B. van Albada, S. Tanase-Nicola, and P. R. ten Wolde. The switching dynamics of the bacterial flagellar motor. *Mol Syst Biol*, 5, 2009.

[149] C. van der Drift, D. B. Janssen, and P. van Wezenbeek. Hydrolysis and synthesis of atp by membrane bound atpase from a motile streptococcus. *Archives of Microbiology*, 119(1):31–36, 1978.

[150] M. C. van Loosdrecht, J. Lyklema, W. Norde, G. Schraa, and A. J. Zehnder. The role of bacterial cell wall hydrophobicity in adhesion. *Applied and Environmental Microbiology*, 53(8):1893–1897, 1987.

[151] T. Vicsek, A. Czirok, E.I Ben-Jacob, I. Cohen, and O. Shochet. Novel type of phase transition in a system of self-driven particles. *Physical Review Letters*, 75(6):1226–1229, 1995. PRL.

[152] R. Vogel. *The bacterial flagellum: Modeling the dynamics of the elastic dynamics of the elastic filament and its transition between polymorphic helical forms*. PhD thesis, Technische Universität Berlin, 2012.

[153] R. R. Vuppula, M. S. Tirumkudulu, and K. V. Venkatesh. Chemotaxis of escherichia coli to l -serine. *Physical Biology*, 7(2):026007, 2010.

[154] L. P. Wackett. Pseudomonas putida- a versatile biocatalyst. *Nature Biotechnology*, 21(2):136–138, 2003.

[155] G. H. Wadhams and J. P. Armitage. Making sense of it all: bacterial chemotaxis. *Nature Reviews Molecular Cell Biology*, 5(12):1024–1037, 2004.

[156] S. Weisse, N. Heddergott, M. Heydt, D. Pflaesterer, T. Maier, T. Haraszti, M. Grunze, M. Engstler, and A. Rosenhahn. A quantitative 3d motility analysis of *Trypanosoma brucei* by use of digital in-line holographic microscopy. *PLoS ONE*, 7(5):e37296, 2012.

[157] W. B. Whitman, D. C. Coleman, and W. J. Wiebe. Prokaryotes: The unseen majority. *Proceedings of the National Academy of Sciences*, 95(12):6578–6583, 1998.

[158] F. Widdel. Theory and measurement of bacterial growth, 08-20-13 2010.

[159] M. Wu, J. W. Roberts, S. Kim, D. L. Koch, and M. P. DeLisa. Collective bacterial dynamics revealed using a three-dimensional population-scale defocused particle tracking technique. *Appl. Environ. Microbiol.*, 72(7):4987–4994, 2006.

[160] Y. Xia and G. M. Whitesides. Soft lithography. *Annual Review of Materials Science*, 28(1):153, 1998.

[161] L. Xie, T. Altindal, S. Chattopadhyay, and X.-L. Wu. Bacterial flagellum as a propeller and as a rudder for efficient chemotaxis. *Proceedings of the National Academy of Sciences*, 108(6):2246–2251, 2011.

[162] J. Xing, F. Bai, R. Berry, and G. Oster. Torque-speed relationship of the bacterial flagellar motor. *Proceedings of the National Academy of Sciences*, 103(5):1260–5, 2006.

[163] F. Yousef-Coronado, M. L. Travieso, and M. Espinosa-Urgel. Different, overlapping mechanisms for colonization of abiotic and plant surfaces by pseudomonas putida. *Fems Microbiology Letters*, 288(1):118–124, 2008.

[164] H. P. Zhang, A. Beer, E.-L. Florin, and H. L. Swinney. Collective motion and density fluctuations in bacterial colonies. *Proceedings of the National Academy of Sciences*, 107(31):13626–13630, 2010.